# Quantum magnetism in two dimensions: From semi-classical Néel order to magnetic disorder

J. Richter[1], J. Schulenburg[2], and A. Honecker[3]

[1] Institut für Theoretische Physik, Otto-von-Guericke-Universität Magdeburg, P.O.Box 4120, D-39016 Magdeburg, Germany
johannes.richter@physik.uni.magdeburg.de
[2] Universitätsrechenzentrum, Otto-von-Guericke-Universität Magdeburg, P.O.Box 4120, D-39016 Magdeburg, Germany joerg.schulenburg@ovgu.de
[3] Institut für Theoretische Physik, TU Braunschweig, Mendelsohnstr. 3, D-38106 Braunschweig, Germany & Universität Hannover, Institut für Theoretische Physik, Appelstrasse 2, D-30167 Hannover, Germany
andreas.honecker@u-cergy.fr

Published version: Chapter 2 in *Quantum Magnetism*, ed by U. Schollwöck, J. Richter, D.J.J. Farnell, R.F. Bishop, Lecture Notes in Physics **645**, 85-153 (Springer-Verlag, Berlin Heidelberg 2004)

**Abstract:**

In this article we focus on the ground state and the low-lying excitations of the $s = 1/2$ Heisenberg antiferromagnet (HAFM) on the 11 two-dimensional (2D) uniform Archimedean lattices.

Although we know from the Mermin-Wagner theorem that thermal fluctuations are strong enough to destroy magnetic long-range order (LRO) for Heisenberg spin systems at any finite temperature in one and two dimensions, the role of quantum fluctuations is less understood. While the ground state of the one-dimensional (1D) quantum HAFM is not long-range ordered, the quantum HAFM e.g. on the 2D square and triangular lattices exhibits semi-classical Néel like LRO. However, in two dimensions there are many other lattices with different coordination numbers and topologies, and there is no general statement concerning zero-temperature Néel-like LRO. Recent experimental results on $CaV_4O_9$ and $SrCu_2(BO_3)_2$ demonstrate the possibility of non-Néel ordered ground states and signal that the $s = 1/2$ HAFM on 2D lattices with appropriate topology may have a ground state without semi-classical LRO.

Based on extensive large-scale exact diagonalization studies of the ground state and the low-lying excitations for the spin-1/2 HAFM on the Archimedean lattices we compare and discuss the ground-state features of all 11 lattices.

In this manner we obtain some insight in the influence of lattice topology on magnetic ordering of quantum antiferromagnets in two dimensions. From our results we conclude that the ground state of the spin-1/2 HAFM on most of the Archimedean lattices (in particular the four bipartite ones) turns out to be semi-classically Néel-like ordered. However, we find that the interplay of competition of bonds (geometric frustration and non-equivalent nearest neighbor bonds) and quantum fluctuations gives rise to a quantum paramagnetic ground state without semi-classical LRO for two lattices. The first one is the famous kagomé lattice, for which this statement is well-known by numerous studies during the last decade. Remarkably, we find one additional lattice among the 11 uniform Archimedean lattices, the so-called star lattice, with a quantum paramagnetic ground state. For both these Archimedean lattices the ground state is highly degenerate in the classical limit $s \to \infty$, although notably their quantum ground states are fundamentally different.

Furthermore, we present numerical results for the magnetization curve of the HAFM on all 11 Archimedean lattices. The magnetization process is discussed in some detail for the square, triangular and kagomé lattices. One focus are plateaus appearing in the magnetization curve due to quantum fluctuations and geometric frustration. In particular, the kagomé lattice exhibits a rich spectrum of magnetization plateaus. Another focus are magnetization jumps arising on the kagomé and the star lattice just below the saturation field. These magnetization jumps may be understood analytically by using independent local magnon excitations.

Some related $s = 1/2$ models are also discussed briefly. Particular attention is given to the 2D Shastry-Sutherland model. For this model, we discuss quantum phase transitions and discuss the magnetization curve in comparison with experiments on $SrCu_2(BO_3)_2$.

This preprint version differs in the following respects from the book chapter:

- Value of the spin-wave result [81] of the sublattice magnetization on the triangular lattice on page 27 corrected: *linear* SWT: $m^{sl} = 0.2387 = 0.4774\ m^{sl}_{\rm class}$. For information: the *second-order* SWT theory result of Ref. [81] reads $m^{sl} = s - 0.2613 + 0.0055/s = 0.2497 = 0.4994\ m^{sl}_{\rm class}$ for $s = 1/2$.
- Value of the ground-state energy per bond for the maple-leaf lattice on page 29 corrected: $E_0/\text{bond} = -0.2137$.
- Value of the square of the order parameter for the $N = 36$ kagomé lattice on page 36 corrected: $(m^+)^2 = 0.059128$.
- Some references updated.

## Contents

## 1 Introduction

The subject of quantum spin-half antiferromagnetism in two-dimensional (2D) systems has attracted a great deal of interest in recent times in connection with the magnetic properties of layered cuprate high-temperature superconductors [1–3] and with the recent progress in synthesizing novel quasi-2D magnetic materials exhibiting a spin-gap behavior like $CaV_4O_9$ [4] or $SrCu_2(BO_3)_2$ [5]. Another striking feature is the plateau structure in the magnetization process of frustrated quasi-two-dimensional magnetic materials like $SrCu_2(BO_3)_2$ [5] or $Cs_2CuBr_4$ [6] (for more details concerning the experiments see chapter by P. Lemmens and P. Millet in this book). However, low-dimensional quantum spin systems are of interest in their own right as examples of strongly interacting quantum many-body systems. Although we know from the Mermin-Wagner theorem [7] that thermal fluctuations are strong enough to destroy magnetic long-range order (LRO) for Heisenberg spin systems in one and two dimensions at any finite temperature, the role of quantum fluctuations is less understood. For the magnetic ordering in the ground state (GS) the transition from one to two dimensions seems to be crucial. It is well known that the GS of the one-dimensional Heisenberg quantum antiferromagnet does not possess Néel LRO (see chapter by H.-J. Mikeska and A.K. Kolezhuk in this book). On the other hand as a result of intensive work in the late eighties it is now well-established that the GS of the Heisenberg antiferromagnet on the square lattice exhibits semi-classical Néel LRO (see for example the reviews [1, 2]). However, Anderson's and Fazekas' investigations [8, 9] of the triangular lattice led to the conjecture that quantum fluctuations plus frustration may be sufficient to destroy the Néel-like LRO in two dimensions.

Besides frustration, there is another mechanism favoring the "melting" of Néel ordering in the ground states of unfrustrated Heisenberg antiferromagnets, namely the competition of non-equivalent nearest-neighbor (NN) bonds leading to the formation of local singlets of two (or even four) coupled spins. By contrast to frustration, which yields competition in quantum as well as in classical systems, this type of competition is present only in quantum systems.

Several notations for the quantum phases without semi-classical Néel order are used in the literature, where one often finds the terms 'quantum disorder' or 'quantum spin liquid'. However, these quantum phases may exhibit quite different complex properties. We shall prefer the notation 'quantum paramagnet' (see, e.g. [10]) to stress their common feature, namely the absence of magnetic order at $T = 0$.

A more specific classification of GS phases of 2D quantum magnets has been proposed recently by Lhuillier, Sindzingre, Fouet and Misguich [11–15]. Besides the semi-classical Néel like LRO, these authors also characterize three quantum GS phases, namely the so-called valence bond crystal, the type I spin liquid and the type II spin liquid (for more details see [11–15] and also section 4.4).

We note that quantum paramagnetic phases may be observed also in three-dimensional strongly frustrated quantum magnets like the Heisenberg antiferromagnet on the pyrochlore lattice [16] although the tendency to order is more pronounced in three than in two dimensions.

In this review we focus on the GS of the 2D isotropic Heisenberg antiferromagnet (HAFM)

$$H = \sum_{<i,j>} J_{ij} \mathbf{S}_i \mathbf{S}_j = \sum_{<i,j>} J_{ij} \left( S_i^x S_j^x + S_i^y S_j^y + S_i^z S_j^z \right) \tag{1}$$

and consider the extreme quantum case of spin quantum number 1/2. Of course, there is a long history of investigations of this model. Nevertheless, much interesting new physics has been discovered in recent years. The 2D systems are of particular interest because the competition between quantum fluctuations and interactions seems to be well balanced, and fine tuning of this competition may lead to zero-temperature transitions between semi-classical and quantum phases (see chapter by S. Sachdev in this book and also section 5).

The calculation of the GS of the spin half HAFM is challenging. Besides the conventional methods like spin-wave theory and general quantum-many body techniques like the coupled cluster method also new numerical methods like quantum Monte Carlo and exact diagonalization are powerful instruments. However, only a few of them (e.g. exact diagonalization or the coupled cluster method) are universally applicable, whereas some methods suffer from the sign problem in frustrated systems. More details regarding analytical and numerical methods can be found in chapters by N.B. Ivanov and D. Sen; D.C. Cabra and P. Pujol; N. Laflorencie and D. Poilblanc; D.J.J. Farnell and R.F. Bishop. The majority of the results presented in this chapter were obtained by exact diagonalization using the program package `spinpack` [17].

Quantum magnetism in 2D systems is a very broad field. To be specific and different from other existing reviews we focus our discussion on the ground state properties of the spin half HAFM on the 11 uniform Archimedean lattices (tilings). These lattices are the prototypes of 2D arrangements of spins and vary in their geometrical and topological properties. Hence they present an ideal possibility for a systematic study of the interplay of lattice geometry and magnetic interactions in 2D quantum spin systems. Many of the lattices considered find their realization in nature either in a pure or in a modified form. Furthermore, almost all lattices can be transformed into each other by bond or site depletion/addition. One now has the opportunity to study GS transitions caused by modifying the strength of some bonds [18].

With regard to other aspects of 2D quantum magnetism like e.g. finite temperature properties we recommend among others the Refs. [1,2,12,13,19–22].

The plan of this review is as follows. In section 2 we describe the main geometrical features of the 11 uniform Archimedean lattices and discuss their

mutual relationships. In section 3 we discuss several criteria for semi-classical Néel like order in quantum antiferromagnets with a particular focus on the information that can be extracted from exact diagonalization of finite lattices. The subsequent section 4 is devoted to the analysis of the magnetic ground-state ordering of the spin-half HAFM on the Archimedean lattices, where we consider separately bipartite (section 4.1) and frustrated (sections 4.2 and 4.3) lattices. The findings for all these lattices are compared and summarized in section 4.4. Readers uninterested in the detailed discussion of the particular lattices are referred to this section 4.4. In section 5 we consider briefly quantum phase transitions occurring in the 2D HAFM due to the interplay of competition in the interactions and strong quantum fluctuations. In the final section 6 we discuss the magnetization process of the spin-half HAFM on the Archimedean lattices using the square (section 6.1), triangular (section 6.2) and kagomé lattice (section 6.3) as main examples. We further discuss exact eigenstates that appear for the kagomé and star lattices in section 6.4 and the relation between the Shastry-Sutherland model and $SrCu_2(BO_3)_2$ in section 6.5.

## 2 Archimedean Lattices

### 2.1 Characteristics and geometry

In 2D magnetism we are faced with a large number of different lattices with differing coordination numbers and topologies and therefore we cannot expect a general statement concerning zero-temperature semi-classical Néel-like LRO in 2D quantum spin systems. Nevertheless, we can try to find some systematics concerning the main geometric features relevant for the magnetic ordering in antiferromagnets.

The 11 uniform Archimedean tilings (lattices) shown in Fig. 1 represent the prototypes of 2D arrangements of regular polygons. The first investigations of 2D regular tilings go back to Johannes Kepler (*Harmonice Mundi*, 1619). 2D (spin) lattices are obtained from the tilings by putting sites (spins) on each vertex connecting neighboring polygons. The HAFM for these lattices is obtained by assuming antiferromagnetic exchange bonds $J = 1$ on each edge of the polygons.

The Archimedean lattices vary in coordination number $z$ (from 3 to 6) and in topology (frustrated and nonfrustrated; equivalent nearest-neighbor (NN) bonds and non-equivalent NN bonds). Therefore a systematic study of the influence of lattice geometry on magnetic ordering may be made.

Among them we have three 2D lattices built by a periodic arrangement of **identical** regular polygons, namely the square lattice (T2), the triangular lattice (T1) and the honeycomb lattice (T3). Other uniform tilings are obtained by combining different regular polygons such as hexagons and triangles or hexagons, squares and triangles with the restriction that all lattice sites are

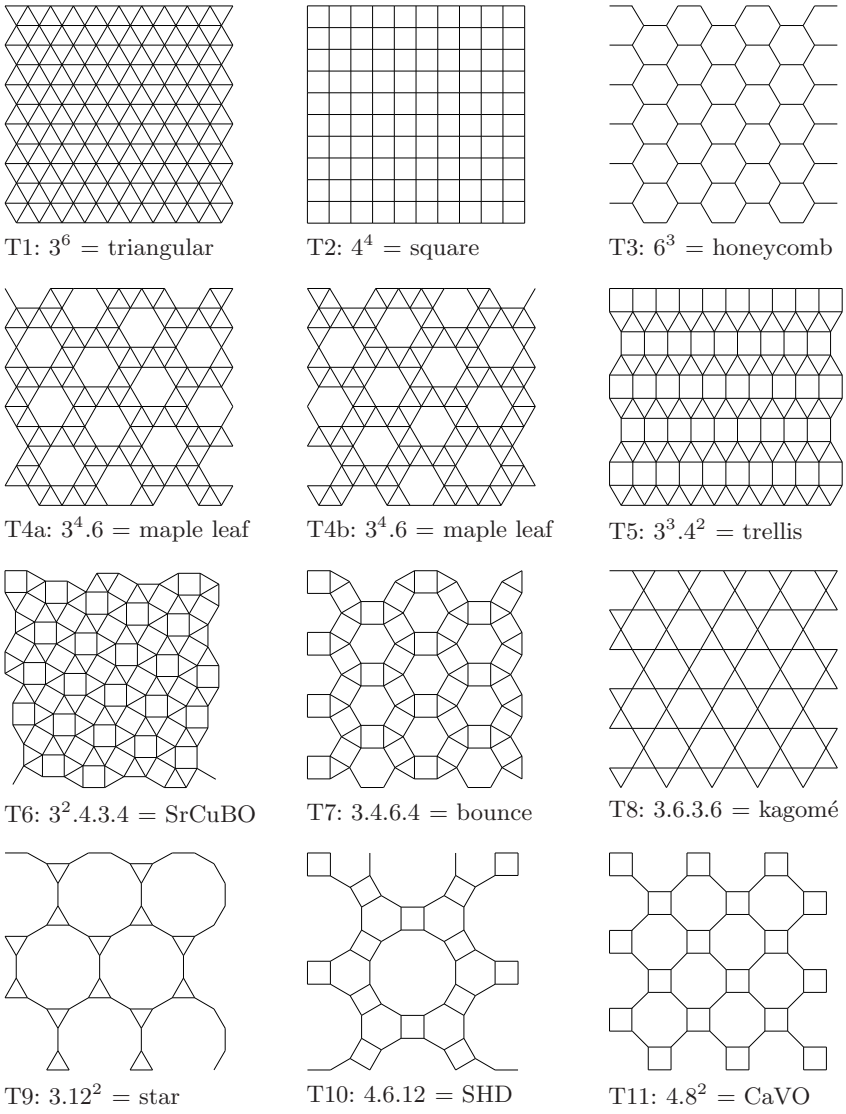


**Fig. 1.** The 11 Archimedean tilings T1...T11. The mathematical description $n_1.n_2.n_3 \ldots n_r$ by numbers $n_i$ separated by dots corresponds to the number of vertices of the polygons arranged around a vertex. The tilings T1, T2, T3, T8 are well-known as triangular (T1), square (T2), honeycomb (T3) and kagomé (T8) lattices. For the other lattices no standardized names are available. For T4, T5, T6, T10 and T11 we employ the names maple-leaf (T4), trellis (T5), SrCuBO or Shastry-Sutherland (T6), SHD (i.e. square-hexagonal-dodecagonal, T10) and CaVO (T11) lattice previously used in papers dealing with magnetic properties of these lattices (see also section 4). We shall denote the tilings T7 and T9 by the names bounce (T7) and star (T9) lattice, proposed in [24].

equivalent and all polygons have identical edge length. Under these geometric restrictions precisely 11 uniform Archimedean tilings are possible, where one tiling exists in two enantiomorphic forms (left and right handed). Only two of them, namely the square lattice (T2), and the triangular lattice (T1) are primitive lattices having only one site per geometric unit cell; all other ones have at least two sites per unit cell. More information can be found, for example, in Ref. [23].

In this section we will illustrate the Archimedean tilings and discuss their main geometric properties. As mentioned above, they represent the prototypes of 2D tilings, from which a large variety of 2D lattices can be derived. As a result we obtain bipartite, i.e. non-frustrated (only even polygons, tilings T2, T3, T10, T11) as well as non-bipartite, i.e. frustrated spin lattices (tilings with odd polygons (triangles), i.e. T1, T4, T5, T6, T7, T8, T9). Furthermore, we can differentiate between lattices with only equivalent NN bonds (T1, T2, T3, T8) and lattices with non-equivalent NN bonds (T4, T5, T6, T7, T9, T10, T11).

The degree of geometric frustration and the coordination number are important quantities that strongly influence the magnetic properties. In order to give a more precise characteristics of the frustration, we use an idea proposed by Kobe and coworkers [25] and consider the GS energy of the classical HAFM (i.e. the spins $\mathbf{S}$ are ordinary classical vectors of length $s = 1/2$). Non-frustrated lattices (T2, T3, T10, T11) have minimal energy per bond $E_0^{\rm class}/{\rm bond} = -1s^2$. Geometric frustration leads to unsatisfied bonds yielding an increase of classical GS energy. This increase of energy can be used as a measure of frustration. The tilings with maximal frustration are the triangular lattice (T1) and the kagomé lattice (T8) having $E_0^{\rm class}/{\rm bond} = -s^2/2$. The combination of strong frustration and low coordination number $z$ favors strong quantum fluctuations. In Fig. 2 we show the location of the lattices in a parameter space spanned by the coordination number $z$ and the frustration. The suppression of classical Néel-like LRO is most likely in the upper left corner in Fig. 2, whereas in the opposite region Néel ordered systems are expected.

### 2.2 Relationships between the lattices

As mentioned above, we interpret the edges of the polygons as exchange bonds which connect the spins sitting on the vertices. In real magnetic systems often we are faced with the situation that bonds may vary in strength for instance due to lattice distortions. Hence it is interesting to consider also bonds varying in strength. In particular, a given lattice may interpolate into another different lattice as selected bonds are forced to reach the limit $J' = 0$. The relationships between the Archimedean lattices based on removing bonds are summarized in Fig. 3.[4] A continuous change of those bonds from $J' = 1$ to $J' = 0$ is therefore

[4] It is also possible to find transformations between lattices by removing sites (site depletion). That is not considered here.

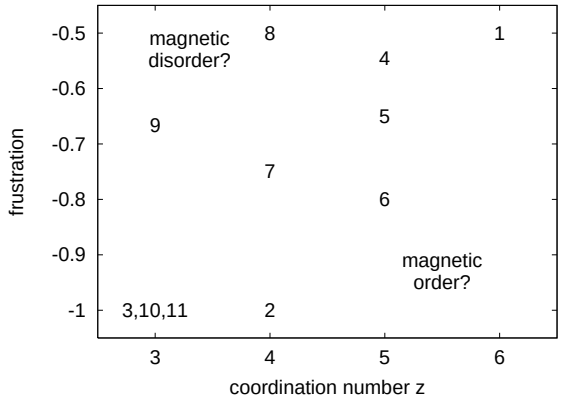


**Fig. 2.** Location of the Archimedean tilings in parameter space spanned by frustration (classical GS energy per bond divided by $s^2$, see text) and coordination number $z$.

accompanied by a transition or a crossover between the ground states of the related lattices. We illustrate some of these relationships between lattices in Figs. 4 and 5.

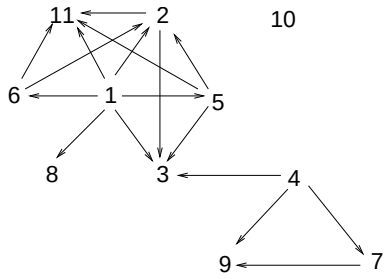


**Fig. 3.** Relationships (arrows) between the tilings (represented by numbers). A related tiling is obtained from an initial tiling by removing certain edges (bonds) and a subsequent appropriate distortion.

Fig. 4 shows the relationships between triangular, square and honeycomb lattices. The square lattice is obtained from the triangular lattice by omitting the dotted bond $J''$. The geometric distortion of the square lattice obtained in this manner is irrelevant for the HAFM because the interaction matrix $J_{ij}$ of the distorted lattice is identical to the regular lattice.[5] The honeycomb lattice

[5] Of course, the distorted lattices obtained by removing bonds may also be transformed to the regular (non-distorted) lattice by an appropriate shift of the sites.

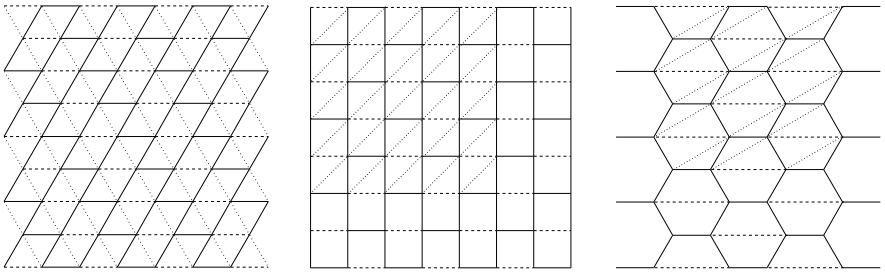


**Fig. 4.** Relationships between triangular (T1, left), square (T2, middle) and honeycomb lattice (T3, right), see text for details.

is then obtained from the square lattice by omitting the dashed bonds $J'$ (the model with variable $J'$ is known as the $J - J'$ model on the square lattice and shows interesting quantum phase transitions [21,26,27]).

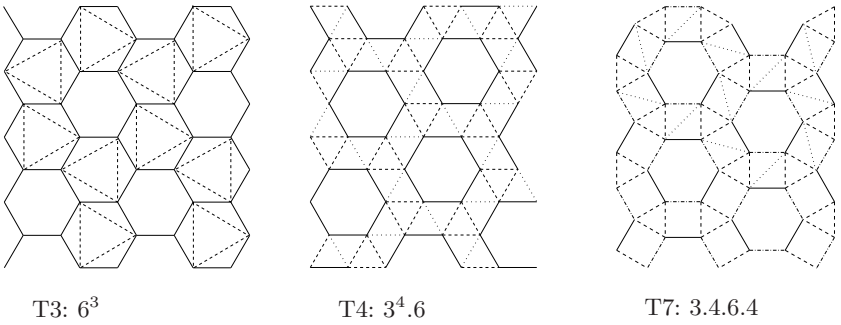


**Fig. 5.** Relationships between the honeycomb (left), maple-leaf (middle) and bounce lattice (right), see text for details.

In Fig. 5 the relationships between the honeycomb, the maple-leaf and the bounce lattice are shown. Starting from the maple-leaf lattice one obtains the bounce lattice by omitting the dotted bonds $J_D$. Further removing the dashed-dotted bond in the bounce lattice one obtains the star lattice (T9, not shown in Fig. 5). On the other hand the honeycomb lattice is obtained from

the maple-leaf lattice by removing the dashed bonds $J_T$. Again the distortion of the lattices is irrelevant for the HAFM.

## 3 Criteria for Néel like order

### 3.1 Order parameter

The definition of the magnetic order parameter is usually related to the classical ground state (GS). Thus supposing that in the classical GS a spin at site $i$ is directed along the unit vector $\mathbf{e}_i$, we choose the spin orientation $\mathbf{e}_i$ as local $z$-direction $\mathbf{e}_i^{z'} = \mathbf{e}_i$, which may in general vary from site to site. In order to break the rotational symmetry we add a field to the Hamiltonian (1)

$$H' = H - h \sum_i \mathbf{e}_i^{z'} \mathbf{S}_i. \tag{2}$$

We define the order-parameter operator as

$$\hat{m}^z = \frac{1}{N} \sum_i S_i^{z'} = \frac{1}{N} \sum_i \mathbf{e}_i^{z'} \mathbf{S}_i. \tag{3}$$

Then the order parameter for a GS spontaneously breaking the rotational symmetry of $H$ is defined as

$$m^z = \lim_{h \to 0} \lim_{N \to \infty} \langle \hat{m}^z \rangle, \tag{4}$$

where $\langle \hat{O} \rangle$ means the expectation value of the operator $\hat{O}$ in the GS. This definition of the order parameter corresponds, e.g., to the order parameter used in spin-wave theory (SWT). However, symmetry breaking is introduced in this case by the Holstein-Primakoff transformation, which starts from a symmetry broken classical GS.

In order to be more specific let us consider a classical spin system having a **planar** magnetic GS ordering. We choose the $z$-$x$ plane of a fixed global coordinate system to describe the order. Then the relation between the spin $\mathbf{S}_i'$ in the local coordinate system and the spin $\mathbf{S}_i$ in the global coordinate system is given by

$$\mathbf{S}_i' = \hat{U}(\phi_i)\mathbf{S}_i = (\cos(\phi_i)S_i^x - \sin(\phi_i)S_i^z \ , \ S_i^y \ , \ \sin(\phi_i)S_i^x + \cos(\phi_i)S_i^z), \tag{5}$$

where $\phi_i$ is the angle between the local $\mathbf{e}_i^{z'}$ and the global $z$ axis $\mathbf{e}^z$. The last component in (5) enters the order-parameter operator $\hat{m}^z$ in (3).

The definition of the order-parameter operator (3) yields the well-known order parameter of the ferromagnet ($\phi_i = 0$) $m^z = \lim_{h \to 0;\, N \to \infty} \frac{1}{N} \langle \sum_i S_i^{z'} \rangle = \lim_{h \to 0;\, N \to \infty} \frac{1}{N} \langle \sum_i S_i^z \rangle$ (magnetization) as well as the order parameter for the conventional two-sublattice Néel antiferromagnet ($\phi_{i \in A} = 0$, $\phi_{i \in B} = \pi$)

$m_s^z = \lim_{h\to 0;\, N\to\infty} \frac{1}{N}\langle \sum S_i^{z'} \rangle = \lim_{h\to 0;\, N\to\infty} \frac{1}{N}\langle \sum \epsilon_i S_i^z \rangle$ (staggered magnetization), where the staggered factor $\epsilon_i$ is $\epsilon_i = +1$ ($\epsilon_i = -1$) for sites belonging to sublattice $A(B)$. The staggered magnetization can be expressed by the sublattice magnetizations $S_A^z = \sum_{i\in A} S_i^z$ and $S_B^z = \sum_{i\in B} S_i^z$, we have $m_s^z = \frac{1}{N}\langle S_A^z - S_B^z \rangle_{h\to 0, N\to\infty}$. The general definition (4) is also applicable for non-collinear (canted) spin structures appearing on frustrated lattices. For example, the classical GS of the HAFM on the triangular lattice consists of three sublattices $A$, $B$, $C$ with an angle of 120° between the sublattice spins, i.e. we have $\phi_{i\in A} = 0$, $\phi_{i\in B} = 2\pi/3$ and $\phi_{i\in C} = 4\pi/3$. Consequently we find $m^z = \frac{1}{N}\langle S_A^z + \sqrt{3}S_B^x/2 - S_B^z/2 - \sqrt{3}S_C^x/2 - S_C^z/2 \rangle_{h\to 0, N\to\infty}$. The extension to arbitrary non-collinear spin structures is straightforward.

The situation is changed for the HAFM on finite lattices considered in numerical studies because the GS of a finite system cannot possess the spontaneous symmetry breaking used for the infinite lattice (eqs. (2) - (4)). Therefore the square of the order-parameter operator $(\hat{m}^z)^2$ has to be used. Furthermore, we have to take into account the fact that the GS of finite antiferromagnetic systems with even number of sites $N$ is a rotationally invariant singlet state.[6] Then the magnetic correlations are equally distributed over all three components $\langle S_i^x S_j^x \rangle = \langle S_i^y S_j^y \rangle = \langle S_i^z S_j^z \rangle$. Thus, taking into account this symmetry, one defines the relevant order parameter for finite systems as

$$\bar{m} = \sqrt{\langle \big(\frac{1}{N}\sum_i \mathbf{S}_i'\big)^2 \rangle} = \sqrt{3\langle (\hat{m}^z)^2 \rangle}\,. \tag{6}$$

One may write this order parameter as

$$\begin{aligned} \bar{m} &= \sqrt{\langle \big(\frac{1}{N}\sum_i \epsilon_i \mathbf{S}_i\big)^2 \rangle} = \sqrt{\frac{1}{N^2}\sum_{i,j} \epsilon_i\epsilon_j \langle \mathbf{S}_i \mathbf{S}_j \rangle} \\ &= \sqrt{\frac{3}{N^2}\langle (S_A^z)^2 + (S_B^z)^2 - 2S_A^z S_B^z \rangle} \end{aligned} \tag{7}$$

for bipartite antiferromagnets and

$$\bar{m} = \sqrt{\frac{3}{N^2}\langle (S_A^z)^2 + (S_B^z)^2 + (S_C^z)^2 - S_A^z S_B^z - S_A^z S_C^z - S_B^z S_C^z \rangle} \tag{8}$$

for the triangular lattice. Note that $\langle S_i^x S_j^z \rangle = 0$ was used in the last equation. Obviously the analysis of magnetic order is then based on the spin pair correlation function $\langle \mathbf{S}_i \mathbf{S}_j \rangle$. We notice that an alternative definition to (4) of the order parameter for infinite systems uses the asymptotic large-distance behavior of the spin pair correlation function.

[6] Note that although there is a rigorous proof for the singlet character of the GS of finite systems only for the HAFM on bipartite lattices [28,29], much numerical evidence suggests that the same statement is true for nonbipartite frustrated antiferromagnetic Heisenberg systems (see e.g. [30]).

The order parameter $\bar{m}$ is widely used for finite lattices such as square or triangular lattices. Finite-size extrapolations of $\bar{m}$ yield good agreement with $m^z$ defined in (4) calculated e.g. by spin-wave theory or the coupled cluster method (see e.g. [31–33]).

However, the definition of the order parameter given above is to some extent problematic for the following reasons: (i) The definition is biased because it supposes the same type of ordering in the quantum system as in the classical system. Investigations of spin systems with spiral order demonstrate, that the characteristic angles $\phi_i$ entering eq. (5) may be different in the classical and quantum case [27]. (ii) There are systems with a huge non-trivial degeneracy of the classical GS (e.g. the HAFM on T8 (kagomé) and on T9 (star), see section 4.3). The question now arises: which of the large number of degenerate classical ground states should be used? (iii) A significant problem is also posed if the classical GS is not known.

We therefore use a universal definition of the order parameter, given by

$$m^+ = \sqrt{\frac{(M^+)^2}{N^2}} = \left( \frac{1}{N^2} \sum_{i,j}^{N} |\langle \mathbf{S}_i \mathbf{S}_j \rangle| \right)^{1/2} , \tag{9}$$

which avoids the problems listed above. For bipartite systems this definition is identical to the staggered magnetization $\bar{m}$ defined in (7). For spin systems with noncollinear GSs both definitions $\bar{m}$ and $m^+$ are not identical, although there is a relation between them. For instance, we have in the classical limit $(m^+_{\mathrm{class}})^2 = \frac{4}{3}(\bar{m}_{\mathrm{class}})^2$ for the HAFM on the triangular lattice. Note that this relation remains valid also for the singlet GS of the quantum spin-1/2 HAFM on the triangular lattice.

Finally, we mention that the universality of the definition (9) of the order parameter may lead to a certain loss of distinction between different types of ordering and for the detection of the type of order an additional inspection of the spin-spin correlation function is necessary.

### 3.2 Mechanism of symmetry breaking - the Pisa tower of quasi-degenerate joint states (QDJS)

As pointed out already by P.W. Anderson [34] the spontaneous symmetry breaking in semi-classically Néel ordered antiferromagnets at the thermodynamic limit is revealed in the spectrum of a finite system. This idea has been picked-up in several papers [31,35–45] dealing with two-dimensional quantum antiferromagnetism.

In the limit $N \to \infty$ a whole set of non-rotationally invariant excited states collapses onto the true GS (e.g. the semi-classical two-sublattice Néel state for the HAFM on a bipartite lattice). Therefore a large amount of information on possible Néel like LRO is contained in the spectrum of HAFM on finite lattices. There are extensive systematic studies for HAFM on the

square, triangular and kagomé lattice [31,36–39,42] and some recent reviews by Lhuillier, Sindzingre, Fouet and Misguich [11–15]. We follow the lines of their studies and illustrate some main features using the HAFM on the square lattice as an example.

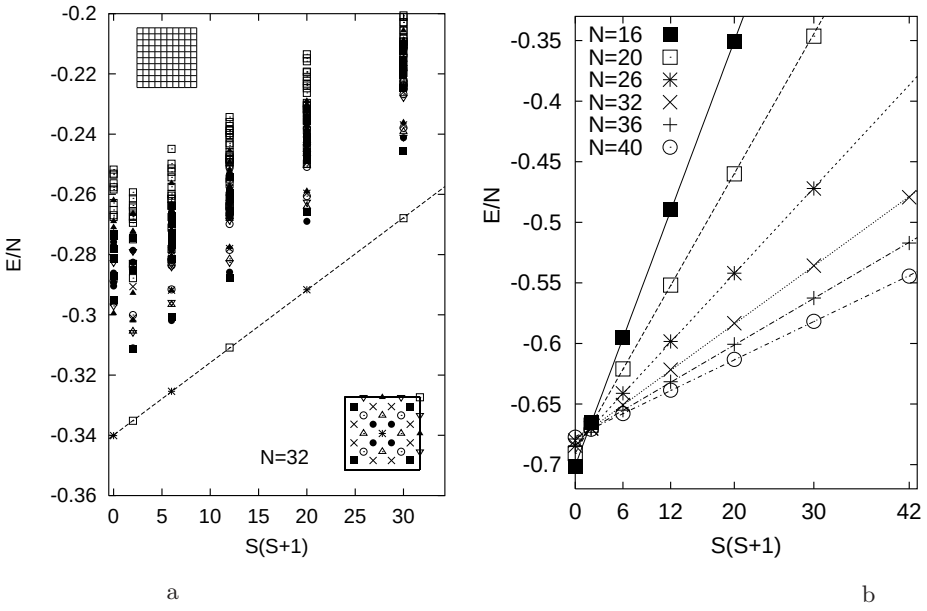


**Fig. 6.** HAFM on the square lattice
a: Low-energy spectrum for $N = 32$ (the inset shows the $\mathbf{k}$ points in the Brillouin zone). b: Energy of the QDJS versus $S(S+1)$ for various system sizes $N$.

For a system with two-sublattice Néel LRO in the GS the low-energy part of the spectrum up to $S \approx \sqrt{N}$ is roughly described by the dynamics of a quantum top, i.e. the effective low-energy Hamiltonian reads

$$H_{\rm eff} \simeq E_0 + \frac{\mathbf{S}^2}{2N\chi_0} + H_{\rm magnons} \;\rightarrow\; E_{\rm min}(S) \simeq E_0 + \frac{S(S+1)}{2N\chi_0} + E_{\rm magnons} \quad (10)$$

with $E_0$ as the GS energy, $\chi_0$ as uniform susceptibility and $\mathbf{S}^2$ as the square of total spin, cf. Fig. 6. The inverse 'moment of inertia' $\frac{1}{N\chi_0}$ vanishes in the thermodynamic limit (see Fig. 7b) and therefore the so-called quasi-degenerate joint states (QDJS) described by (10) collapse to the symmetry broken Néel state in the thermodynamic limit. In case of more complex Néel order e.g. with three sublattices as for the HAFM on the triangular lattice the basic features of the low-energy Hamiltonian as given in eq. (10) are maintained but the moment of inertia then contains both in-plane and out-of-plane susceptibilities. Also the number of the QDJS for a given total spin $S$ depends on the

number of sublattices in the Néel state. There is only one QDJS in each sector of $S$ for the two-sublattice HAFM, but e.g. $N_S = \min(2S+1, N/2-S+1)$ QDJS for a three-sublattice Néel state such as in the triangular lattice [37]. Furthermore, the translational symmetry of the QDJS depends on the relation between the translational symmetry of the Néel state and of the lattice. For instance, the size of the magnetic unit cell for the Néel ordered square-lattice (triangular-lattice) HAFM is twice (three times) as large as the geometric unit cell. Consequently, the QDJS belong to $\mathbf{k}$-vectors $\mathbf{Q}_1 = (0,0)$ and $\mathbf{Q}_2 = (\pi,\pi)$ ($\mathbf{Q}_1 = (0,0)$ and $\mathbf{Q}_2^+ = (+4\pi/3, 0)$, $\mathbf{Q}_2^- = (-4\pi/3, 0)$) of lattice translational symmetry with $\mathbf{Q}_2$ ($\mathbf{Q}_2^+$ and $\mathbf{Q}_2^-$) mapping on the center of the magnetic Brillouin zone. However, only $\mathbf{Q} = (0,0)$ appears for the QDJS for the honeycomb lattice which has two atoms in the geometric unit cell as well as in the magnetic unit cell.

Indeed, a linear relation between the lowest eigenvalues $E_{\min}(S)$ and $S(S+1)$ and a similar relation for the family of magnon excitations has been observed for the HAFM on the 2D square lattice [35], the honeycomb lattice [42] as well as for the triangular-lattice HAFM [37]. We show in Fig. 6a the low-energy spectrum for the HAFM on the square lattice with $N = 32$ sites in more detail.

According to (10) the collapsing QDJS follow in the energy-$S(S+1)$ diagram for small $S \lesssim \sqrt{N}$ in good approximation a straight line with increasing inclination (with decreasing slope), see Fig. 6b, and are sometimes called the Pisa tower of states. The strong deviation from this linear relation has been used as one argument for the absence of semi-classical LRO for the HAFM on the kagomé lattice [38]. A similar argumentation has been used in [40] for the $J_1 - J_2$ square-lattice HAFM and in [41] for the HAFM on the fractal Sierpiński gasket.

Well separated above the family of QDJS a second family of levels exists describing the magnon excitations typical for a HAFM with Néel ordering. This family represents the 'softest magnons', i.e. magnons of energy $E_{\min}^M = c|\mathbf{k}_{\min}|$ with $c$ as lowest spin-wave velocity and $|\mathbf{k}_{\min}| \sim \frac{1}{L}$ ($L = \sqrt{N}$) as smallest finite wave vector (related to the wave vector $\mathbf{Q}$ of the corresponding QDJS) allowed by the periodic boundary conditions of the finite lattice. The energy of these magnons also collapses, however, with

$$E_{\min}^M \simeq \frac{c}{\sqrt{N}} \tag{11}$$

much slower than $E_{\min}(S) \propto \frac{1}{N}$ from eq. (10). This scaling behavior of the QDJS and of the softest magnons is shown in Fig. 7a, where the logarithmic scale in this figure makes it obvious that the slope of the $E_0(S=1) - E_0$-curve belonging to the QDJS is about twice as large as the slope of the $E_1(S=1) - E_0$-curve belonging to the softest magnons.

Finally we want to emphasize two special aspects of the spectrum of semi-classically Néel ordered HAFMs. The first one is the so-called spin gap, i.e. the gap $\Delta = E_0(S=1) - E_0(S=0)$ between the first triplet excitation

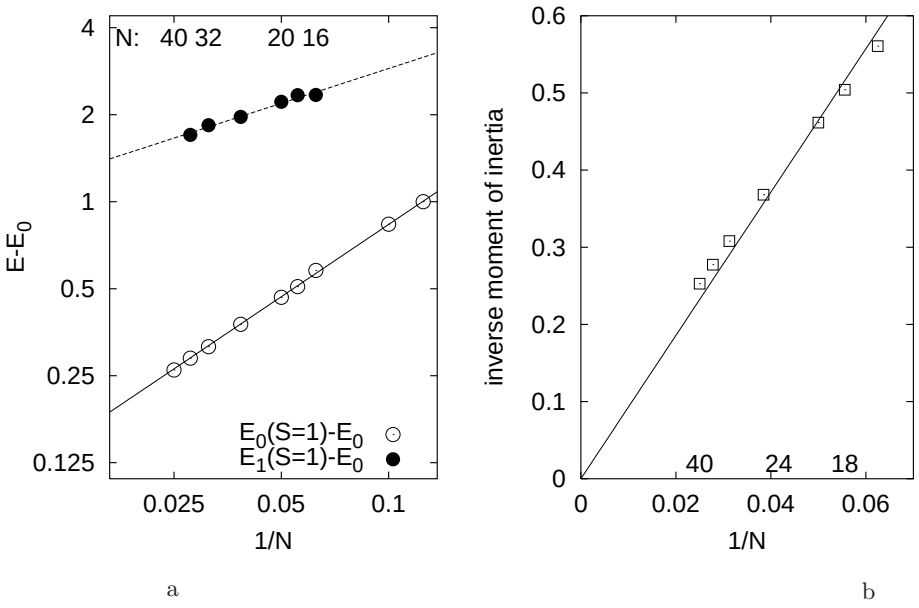


**Fig. 7.** HAFM on the square lattice
a: Finite-size scaling of lowest excitations (double logarithmic scale). b: Finite-size scaling of inverse moment of inertia.

and the singlet GS. According to eqs. (10) and (11) this gap vanishes in the thermodynamic limit for a Néel ordered GS. Note that eq. (11) is related to the existence of gapless Goldstone modes. However, a non-vanishing spin gap for $N \to \infty$ is an indication for a quantum paramagnetic GS. The second aspect is that the singlet GS is unique and the lowest singlet excitation above the GS is well separated from it in a finite system (see Fig. 6a). The first triplet excitation above the rotationally invariant singlet GS generally is the lowest excitation at all. Therefore the existence of low-lying singlets deep within the spin gap also can be understood as an indication for a non-Néel ordered GS.

### 3.3 Finite-size scaling

Effective continuum field-theory studies as well as spin-wave theory and quantum Monte Carlo (QMC) calculations have led to detailed predictions for the low-energy physics and the finite-size scaling of Néel ordered quantum antiferromagnets in two dimensions [35,44–47], which we will use below in eqs. (12), (13) and (14). As already discussed in the last section the inverse 'moment of inertia' is obtained from the QDJS and so the spin gap scales in leading order with $1/N$, see eq. (10). However, for finite-lattice sizes accessible in exact diagonalization the asymptotic behavior is often not reached and boundary

effects are important. Hence, the extrapolation to $N \to \infty$ possesses some uncertainty. According to Refs. [35,44–47] the GS energy per site $e_0 = \frac{E_0}{N}$ for a semi-classical Néel state scales as

$$e_0(L) = A_0 + \frac{A_3}{L^3} + \mathcal{O}(L^{-4}) \tag{12}$$

where $L = N^{1/2}$ is the linear size of the lattice, $A_0 = e_0(\infty)$ and $A_3$ is proportional to the spin-wave velocity $c$. For the order parameter $m^+$ we use

$$m^+(L) = B_0 + \frac{B_1}{L} + \mathcal{O}(L^{-2}) \tag{13}$$

where $B_0 = m^+(\infty)$. For the spin gap $\Delta$ we apply

$$\Delta(L) = G_0 + \frac{G_2}{L^2} + \mathcal{O}(L^{-3}) \tag{14}$$

where $G_0 = \Delta(\infty)$. In case that there are many appropriate finite lattices with $N \leq 36$ the large number of data points leads to reliable extrapolation to the thermodynamic limit [32,33]. On the other hand, for systems with only a few appropriate finite lattices the extrapolation is much stronger influenced by the boundary effects and the extrapolated results exhibit a larger uncertainty. Furthermore, only the leading terms in (12), (13), (14) can be used in case of a small number of data points. Particular problems may arise for the spin gap: (i) Boundary effects are present in both $E_0$ and $E_1$ leading to a larger error in $E_1 - E_0$. (ii) As discussed in the last section the first triplet excitation belongs to the QDJS with a definite symmetry. However, it may appear that this symmetry is not present in a certain finite lattice, i.e. the calculated first excitation belongs to another symmetry and consequently it has higher energy leading to an overestimation of the gap. Therefore the extrapolation of the gap will not be a main focus of our discussion of the ordering of the HAFM on the Archimedean tilings in section 4.

We use only the leading terms even in case that the number of data points would allow a scaling including next-to-leading term in order to have the same systematics for all the 11 Archimedean tilings in the comparative discussion given below. By way of illustration we compare the results obtained by both variants of extrapolation for the square lattice (for a comparison with data available in literature, see section 4.1):

- GS energy per site: $E_0/N = -0.6701$ (leading term only); $E_0/N = -0.6685$ (next-to-leading term included);
- singlet-triplet gap: $\Delta = 0.0605$ (leading term only); $\Delta = 0.0247$ (next-to-leading term included);
- order parameter: $m^+ = 0.3173$ (leading term only); $m^+ = 0.3235$ (next-to-leading term included).

For the extrapolation altogether 12 finite square lattices from $N = 18$ to $N = 40$ are used. The consideration of the next-to-leading terms changes the

energy by less than 0.2% and the order parameter by less than 2%. The values for the extrapolated gap can be understood as a measure of the accuracy of the extrapolation, since we know that the excitations about a Néel ordered GS become gapless for $N \to \infty$.

Finally, we mention that the finite-size scaling for systems with a critical GS or with a GS having only short-range spin pair correlations $\langle \mathbf{S}_i \mathbf{S}_j \rangle$ can be different from the above given relations. The concrete relations may depend on details of GS correlations. Nevertheless one aspect shall be noted: due to the absence of long-range correlations in $\langle \mathbf{S}_i \mathbf{S}_j \rangle$ the finite-size effects should be weaker for the GS energy. As a simple example we can consider a HAFM with a valence-bond GS as realized for the Shastry-Sutherland model for stronger frustration (see section 5). The GS energy per site is completely independent of $N$ in this case.

## 4 Magnetic ground-state ordering for the spin half HAFM on the Archimedean lattices

In this section we present and discuss results obtained by exact diagonalization for the 11 Archimedean lattices. For some of these lattices such studies have not been performed so far or the presented results go beyond the system sizes published until now. If available we also discuss results obtained by other methods to get a reliable picture on the magnetic ordering. From our results we conclude that three categories of ground state ordering appear: Collinear two-sublattice Néel long-range order (LRO), non-collinear (multi-sublattice Néel or spiral) LRO and quantum paramagnetic ground states without LRO in the spin pair correlation $\langle \mathbf{S}_i \mathbf{S}_j \rangle$.

At first we consider in sections 4.1, 4.2 and 4.3 each lattice separately and present results for the GS energy, the spin gap and the order parameter as well as the spectrum. In a second step we summarize and compare in section 4.4 the magnetic ordering on the various Archimedean lattices. We refer the reader who is not interested in the detailed discussion of the individual lattices to section 4.4.

### 4.1 Semi-classical Néel ordering on bipartite lattices

The classical GS for bipartite lattices is the perfect Néel state having a GS energy per bond $E_0^{\text{class}}/\text{bond} = -s^2 = -0.25$ and an order parameter $m^+_{\text{class}} = s = 0.5$. However, this classical order is very sensitive to fluctuations. Indeed the 1D HAFM does not exhibit Néel LRO. For the 2D HAFM we know from the Mermin-Wagner theorem [7] that at arbitrarily small finite temperatures $T$ the thermal fluctuations are strong enough to destroy the Néel LRO. However, it was for a long time an open question whether also quantum fluctuations are able to destroy Néel LRO in 2D at absolute zero. Each 2D lattice needs its individual consideration because the strength of quantum fluctuations can

vary from lattice to lattice. Stronger quantum fluctuations appear in lattices with low coordination number $z$ and in lattices with non-equivalent NN bonds. Although this non-equivalency of NN bonds is irrelevant for classical bipartite HAFM it leads to a competition between the bonds in quantum models. This quantum competition favors local singlet formation weakening that way Néel ordering (see, e.g. [27,48] and section 5).

### The square lattice (T2)

Starting from P.W. Anderson's pioneering work [34], the spin half HAFM on the square lattice has been studied over many decades. There are some excellent reviews [1–3] which can be used to get more detailed information on this work. Although till now there is no rigorous proof for the existence of Néel LRO[7] after intensive studies over many decades it became clear in the late eighties that there is no doubt of semi-classical Néel LRO at absolute zero. The quantum fluctuations lead to a substantial renormalization of the order parameter (sublattice magnetization), which amounts to about 60% of the classical value. Experimentally there are some layered antiferromagnetic inorganic materials like the parent compound $La_2CuO_4$ for high-$T_c$ superconductors or $Sr_2CuO_2Cl_2$ [2,19,53] but also organic compounds [54] which are well described by the (quasi-)2D HAFM on the square lattice.

The spin half HAFM on the square lattice can serve as the canonical example for a quantum HAFM on a 2D bipartite lattice. Already about ten years ago Schulz and coworkers [55] published large-scale exact diagonalization studies for the GS of systems up to $N = 36$. Recently Betts and coworkers [33] have presented a systematic study of a complete set of all finite square lattices up to $N = 32$. In particular, one finds in [33] a guideline how to find systematically the so-called defining edge vector in finite lattices for arbitrary dimension and type of lattice. We use this scheme to generate the finite lattices discussed below. We have recalculated and extended Schulz' and Betts' results for systems up to $N = 40$ sites including the results for the low-lying excitations. We have presented some of our results already in sections 3.2 and 3.3.

The classical GS breaks the translational symmetry of the lattice. The magnetic unit cell is twice as large as the geometric one. On a finite bipartite lattice the quantum GS is a rotationally invariant singlet state (Lieb-Mattis theorem [29]). As can be seen from Fig. 6a there is one QDJS in each sector $S$ (cf. section 3.2) and the translational symmetry of the QDJS alternates between $\mathbf{Q}_0 = (0,0)$ and $\mathbf{Q}_1 = (\pi,\pi)$. Note that $\mathbf{Q}_0$ and $\mathbf{Q}_1$ are different in the geometric but they coincide in the magnetic Brillouin zone. The energies of the QDJS are well described by $E_0 + S(S+1)/2N\chi_0$, see eq. (10). The

[7] We mention that the existence of Néel LRO was proven for the HAFM with $S \geq 1$ [49,50] and for the spin half anisotropic $XXZ$ antiferromagnet [51,52] on the square lattice.

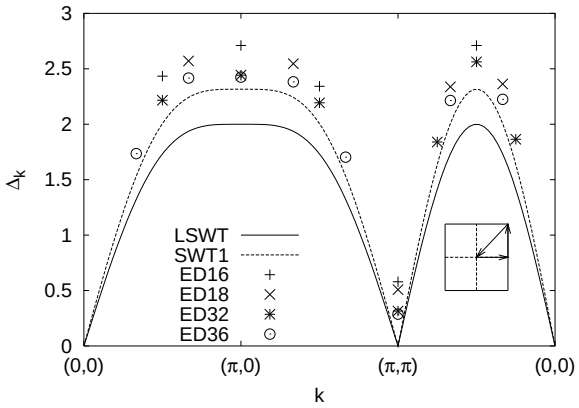


**Fig. 8.** Energy of the one-magnon excitations $\Delta_k = E_0(\mathbf{k}, S = 1) - E_0(S = 0)$ versus $\mathbf{k}$ (dispersion relation). The solid and dashed lines show results of the linear (LSWT) and higher-order spin-wave theory (SWT1) [56], the points are exact data for finite lattices of size $N = 16$, 18, 32 und 36. The inset in the right part of the figure shows the path through the Brillouin zone.

family of one-magnon states is well separated from the QDJS. Their energies follow the dispersion relation obtained by spin-wave theory, see Fig. 8. The lowest singlet excitation is significantly above the first triplet excitation.

The GS energy, the first excitation and the square of the order parameter for the largest lattices with $N = 38$ and $N = 40$ and for comparison for $N = 36$ are given in table 1. Furthermore, we present for the first time all spin-spin correlations for $N = 40$ in table 2. It is obvious that the decay of the spin-spin correlations is weak.

**Table 1.** Ground-state energy $E_0$ (singlet), singlet-triplet gap (spin gap) $\Delta = E_0(S = 1) - E_0$ and square of the order parameter $m^2 \equiv (m^+)^2$ of the HAFM on finite square lattices with $N = 38$, $N = 40$ and $N = 36$ sites (the results for $N = 36$ are in agreement with those of [55]). $(l_{11}, l_{12})$ and $(l_{21}, l_{22})$ are the components of the two edge vectors defining the finite 2D lattice.

| $N$ | $l_{11}$ | $l_{12}$ | $l_{21}$ | $l_{22}$ | $E_0$ | $\Delta$ | $m^2$ |
|---|---|---|---|---|---|---|---|
| 36 | 6 | 0 | 0 | 6 | −24.4393974 | 0.287538 | 0.20983715 |
| 38 | 1 | 7 | −5 | 3 | −25.7607925 | 0.272791 | 0.20751801 |
| 40 | 2 | 6 | −6 | 2 | −27.0948503 | 0.261623 | 0.20361937 |

Altogether 12 finite square lattices from $N = 18$ to $N = 40$ are used for the extrapolation of the GS energy and the order parameter to infinite $N$ (see

**Table 2.** Ground-state spin-spin correlations $\langle S_0^z S_R^z \rangle = \frac{1}{3}\langle \mathbf{S}_0 \mathbf{S}_R \rangle$ for all lattice vectors $\mathbf{R}$ of the HAFM on a square lattice with $N = 40$ sites. Note that due to the reduced symmetry of the finite lattice we have slightly different values for lattice vectors $\mathbf{R} = (3,1)$ and $(3,-1)$ as well as for $\mathbf{R} = (1,2)$ and $(1,-2)$.

| $\mathbf{R}$ | $(0,0)$ | $(0,1)$ | $(1,1)$ | $(0,2)$ | $(1,-2)$ | $(1,2)$ |
|---|---|---|---|---|---|---|
| $\langle S_0^z S_R^z \rangle$ | 0.250000 | −0.112895 | 0.069066 | 0.061711 | −0.059679 | −0.059055 |
| $\mathbf{R}$ | $(2,2)$ | $(0,3)$ | $(3,1)$ | $(3,-1)$ | $(3,-2)$ | $(4,-2)$ |
| $\langle S_0^z S_R^z \rangle$ | 0.053826 | −0.055663 | 0.054700 | 0.052344 | −0.052074 | 0.050275 |

Figs. 20a and 21a). We compare our results with some corresponding data obtained by other means:

- GS energy per bond: our result: $E_0/\text{bond} = -0.3350$; high-order SWT [56]: $E_0/\text{bond} = -s^2 - 0.157948s - 0.006237 + 0.0000108/s = -0.335233$; QMC [47]: $E_0/\text{bond} = -0.334719$; coupled cluster method (CCM) [57]: $E_0/\text{bond} = -0.3349$; series expansion [58]: $E_0/\text{bond} = -0.3347$; previous exact diagonalization up to $N = 32$ [33]: $E_0/\text{bond} = -0.33404$;
- order parameter (sublattice magnetization): our result: $m^+ = 0.3173 \sim 0.635\, m^+_{\text{class}}$; high-order SWT [56]: $m^+ = s - 0.1966019 + 0.0000866(25)/s^2 = 0.3037$; QMC [47]: $m^+ = 0.3070$; CCM [57]: $m^+ = 0.31$; series expansion [58]: $m^+ = 0.307$; previous exact diagonalization up to $N = 32$ [33]: $m^+ = 0.30676$

(for the extrapolation of the gap, see section 3.3). A more detailed collection of results for the sublattice magnetization and the GS energy obtained by different methods can be found in [33, 57].

The existence of Néel LRO for the square lattice does not automatically imply the conclusion, that all other bipartite lattices are also Néel long-range ordered. Stronger quantum fluctuations can appear in lattices with coordination number $z < 4$ and in lattices with non-equivalent NN bonds.

### The honeycomb lattice (T3)

For this lattice the geometric and the magnetic (Néel state) unit cell are identical and include two sites. All NN bonds are equivalent but the coordination number $z = 3$ is less than in the square lattice giving rise to stronger quantum fluctuations. Nevertheless there is a lot of evidence obtained by several methods [27, 42, 59–62] and also from the data presented below, that the GS is a semi-classical Néel state.

The low-energy spectrum is shown in Fig. 9. The QDJS are well separated from the other states and follow eq. (10). Due to the coincidence of geometric and magnetic unit cell they all have translational symmetry vector $\mathbf{Q} = (0,0)$. There are no low-lying singlets within the spin gap. The similarity between the spectra of the square and the honeycomb lattice is obvious.

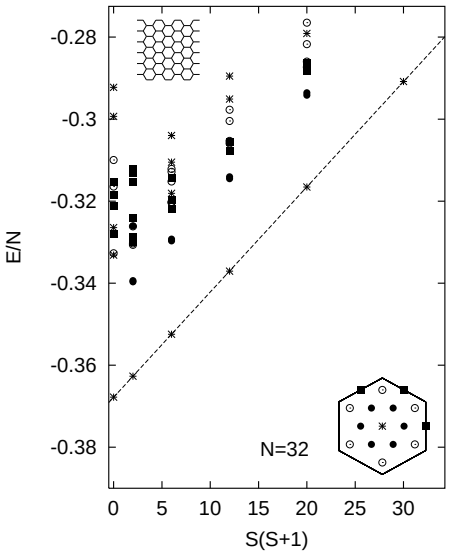


**Fig. 9.** Low-energy spectrum for the HAFM on the honeycomb lattice with $N = 32$ sites (the inset shows the $\mathbf{k}$ points in the Brillouin zone).

The largest lattice considered has $N = 38$ sites and is defined by the edge vectors $(3, 2); (-2, 5)$ and has GS energy $E_0/\text{bond} = -0.366768$, spin gap $\Delta = 0.213953$ and square of the order parameter $(m^+)^2 = 0.184396$.

For the finite-size extrapolation of the GS energy (Fig. 20a), the spin gap and the order parameter (Fig. 21a) we have used 14 finite lattices from $N = 6$ up to $N = 38$. The extrapolation according to formulae (12), (13), (14) leads to the following results:

- GS energy per bond: $E_0/\text{bond} = -0.3632$
  (for comparison: QMC [59]: $E_0/\text{bond} = -0.3630$; 2nd order SWT [60]: $E_0/\text{bond} = -s^2 - 0.209842s - 0.0110084 = -0.365929$; series expansion [61]: $E_0/\text{bond} = -0.3629$; CCM [27]: $E_0/\text{bond} = -0.3631$);
- spin gap: $\Delta = 0.0504$
  (for comparison: CCM [27]: $\Delta = 0.02$);
- order parameter: $m^+ = 0.2788 \sim 0.558\, m^+_{\text{class}}$
  (for comparison: QMC [59]: $m^+ = 0.235$; 2nd order SWT [60]: $m^+ = 0.2418$; series expansion [61]: $m^+ = 0.266$; CCM [27]: $m^+ = 0.28$).

Obviously due to the lower coordination number the magnetization is approximately 10% smaller than for the square lattice, but the existence of Néel LRO is not in question.

### The CaVO (T11) and the SHD (T10) lattices

Both these lattices have non-equivalent NN bonds and low coordination number $z = 3$ leading to strong quantum fluctuations. The lattice T11 has attracted much attention since 1995 when in susceptibility measurements on $CaV_4O_9$ [4] for the first time a rotationally invariant quantum paramagnetic GS with a finite spin gap of $\Delta \approx 110$K was discovered experimentally for a quasi-2D antiferromagnetic spin half system. The underlying lattice of $CaV_4O_9$ is a 1/5 site-depleted square lattice which can be transformed by an appropriate distortion to the Archimedean lattice T11 (see Fig. 10). We use therefore the name 'CaVO' to denote this lattice. The experimental findings stimulated a series of theoretical studies for the spin half HAFM on the CaVO lattice [48, 63–77]. The geometric unit cell of the CaVO lattice contains four sites. However, the translational symmetry of the lattice and of the classical Néel GS do not fit to each other and consequently the magnetic unit cell must be chosen as twice as large as the geometric one. This makes the symmetry of the QDJS similar to that of the square lattice (see Figs. 11a and 6a).

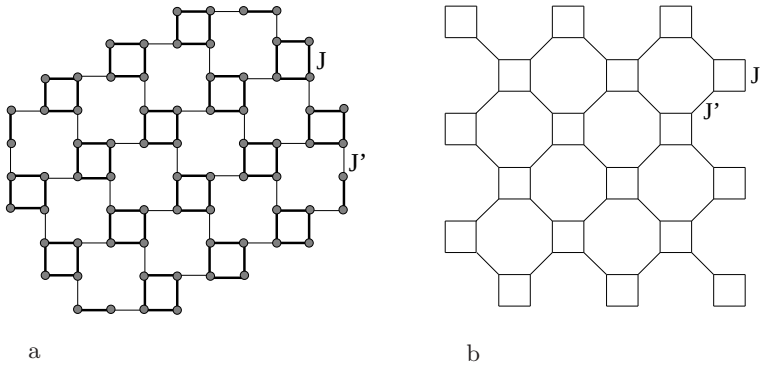


**Fig. 10.** Arrangement of the $V^{4+}$ atoms (points) in the V-O layers of $CaV_4O_9$ (left) and the corresponding Archimedean tiling T11 (right).

The Archimedean lattice T10 is built by regular squares, hexagons and dodecagons (SHD) and is therefore more complex than the CaVO lattice. As far as we know till now no antiferromagnetic material was synthesized having the lattice structure of tiling 10. The low coordination number, the quantum competition of non-equivalent NN bonds and the complex structure of the lattice have stimulated the search for a possible non-Néel ordered GS for this lattice [43, 78]. The geometric unit cell of the SHD lattice contains twelve sites. The translational symmetry of the lattice and of the classical Néel GS fit to each other leading to identical magnetic and geometric unit cell. Hence

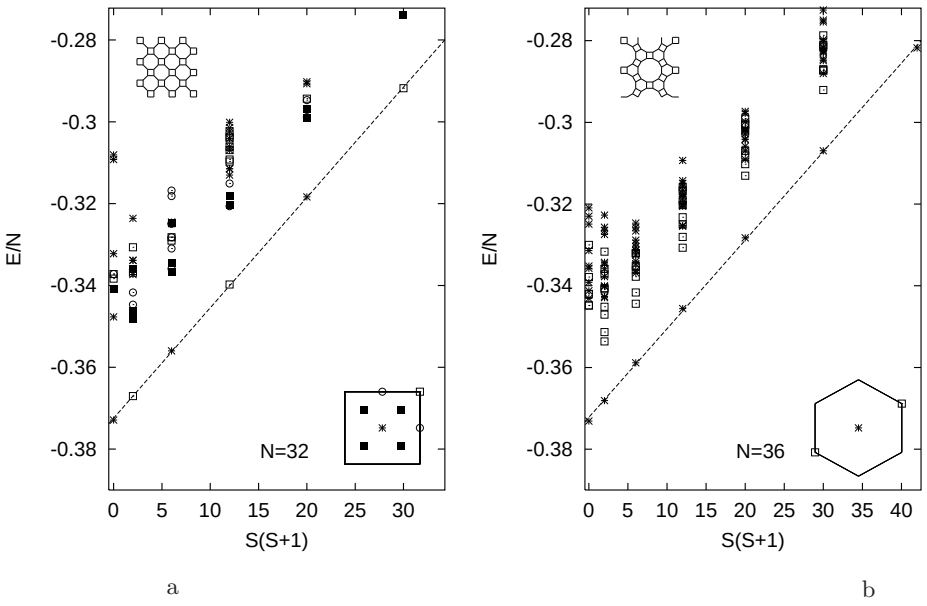


**Fig. 11.** Low-energy spectrum for HAFM on the CaVO (T11) and on the SHD (T10) lattice (the insets show the **k** points in the Brillouin zone).
a: CaVO with $N = 32$. b: SHD with $N = 36$.

the symmetry of the QDJS is similar to that of the honeycomb lattice (see Figs. 11b and 9). The similarities between the spectra of the square and the CaVO lattice as well as the SHD and the honeycomb lattice are obvious: The QDJS are well separated from the other states and follow eq. (10). There are no low-lying singlets within the spin gap.

Since the magnetic unit cell contains 8 sites, the largest CaVO lattice we consider has $N = 32$ sites and is defined by the edge vectors $(2, -2); (2, 2)$. It has GS energy per bond $E_0/\text{bond} = -0.372903$, spin gap $\Delta = 0.281788$ and square of the order parameter $(m^+)^2 = 0.178018$. The two non-equivalent NN correlations functions for $N = 32$ are $\langle \mathbf{S}_i \mathbf{S}_j \rangle_J = -0.311103$ for $J$ bonds belonging to squares and $\langle \mathbf{S}_i \mathbf{S}_j \rangle_{J'} = -0.403803$ for $J'$ dimer bonds (cf. Fig. 10).

The largest SHD lattice considered has $N = 36$ sites and is defined by the edge vectors $(2, 1); (-1, 1)$. It has GS energy per bond $E_0/\text{bond} = -0.373118$, spin gap $\Delta = 0.270929$ and square of the order parameter $(m^+)^2 = 0.163243$. The three non-equivalent NN correlations functions for $N = 36$ are $\langle \mathbf{S}_i \mathbf{S}_j \rangle_{SH} = -0.414324$ for NN bonds belonging to squares and hexagons, $\langle \mathbf{S}_i \mathbf{S}_j \rangle_{SD} = -0.395046$ for NN bonds belonging to squares and do-

decagons and $\langle \mathbf{S}_i \mathbf{S}_j \rangle_{HD} = -0.309984$ for NN bonds belonging to hexagons and dodecagons.

The finite-size extrapolation for the CaVO and even more for the SHD lattice suffers from the restriction to a small number of unit cells in the accessible finite lattices. Hence the extrapolation is particularly uncertain and should be taken with extra care. For the finite-size extrapolation of the GS energy (Fig. 20a), and the order parameter (Fig. 21a) according to formulae (12), (13), (14) we use finite lattices of $N = 16, 24, 32$ (CaVO) and $N = 12, 24, 36$ (SHD). The extrapolation leads to the following results for the CaVO lattice:

- GS energy per bond: $E_0/\text{bond} = -0.3689$
  (for comparison: linear SWT [64]: $E_0/\text{bond} = -0.3584$);
- spin gap: $\Delta = 0.1149$ (for comparison: QMC [48]: $\Delta \sim 0$);
- order parameter: $m^+ = 0.2303 \sim 0.461\, m^+_{\text{class}}$
  (for comparison: linear SWT [64]: $m^+ = 0.212$; QMC [48]: $m^+ = 0.178$)

and for the SHD lattice:

- GS energy per bond: $E_0/\text{bond} = -0.3713$
  (for comparison: variational (Huse-Elser) [78]: $E_0/\text{bond} = -0.3605$; variational (resonating valence bond (RVB)) [43]: $E_0/\text{bond} = -0.3688$);
- spin gap: $\Delta = 0.1435$;
- order parameter: $m^+ = 0.2126 \sim 0.425\, m^+_{\text{class}}$
  (for comparison: variational (RVB) [43]: $m^+ = 0.2546$).

Due to the competition between the bonds the order parameters for the CaVO and the SHD lattice are smaller than for the honeycomb lattice. Nevertheless we find convincing evidence that the GS is semi-classically Néel ordered. This conclusion is well supported by other methods [43, 48, 64, 66, 67, 72, 78]. However, the quantum competition between non-equivalent bonds leads to a tendency to form local singlets either on neighboring bonds or along polygons. In connection with the observed rotationally invariant quantum paramagnetic GS with a finite spin gap in $CaV_4O_9$ for the CaVO lattice a $J - J'$- HAFM with different strengths of NN bonds $J$ and $J'$ is considered, where $J$ is the NN bond belonging to a square and $J'$ is the NN bond not belonging to a dimer (Fig. 10). Within this model a quantum phase transition between the semi-classical Néel ordered phase and a quantum paramagnetic rotationally invariant singlet phase with gapped excitations is obtained. We will discuss this $J - J'$- HAFM and its quantum phase transition in more detail in section 5.

### 4.2 Semi-classical LRO on frustrated lattices

The classical GS for non-bipartite frustrated lattices may be collinear (weak frustration) or non-collinear (strong frustration) and depends on the special features of the lattice. The frustration may enhance the effect of quantum fluctuations so that the magnetic order may be stronger weakened than for the

bipartite lattices. Thus the frustrated HAFM on 2D lattices is an interesting candidate for a magnetic system with a quantum paramagnetic GS.

### The triangular lattice (T1)

The triangular lattice is strongly frustrated but has largest coordination number $z = 6$ (see Fig. 2). Already in the 70ties Anderson and Fazekas [8,9] considered the spin half HAFM on the triangular lattice. They argued that the GS for the 2D triangular lattice might be similar to that for the 1D HAFM and proposed a spin-liquid like rotationally invariant resonating valence bond GS instead of a semi-classical Néel state. Starting in the late eighties several authors found, however, more and more evidence for a Néel ordered GS (see e.g. [31,36,37,79–86]).

The classical GS is a three-sublattice Néel state with an angle of 120° between the spins of different sublattices (Fig. 12a). It breaks the translational symmetry of the lattice. The energy per bond is $E_0^{\rm class}/{\rm bond} = -s^2/2 = -0.125$ and the order parameter is $m^+_{\rm class} = \frac{1}{2}\sqrt{2/3} = 0.40825$.

The magnetic unit cell is three times as large as the geometric one and thus the QDJS belong to vectors $\mathbf{Q}_1 = (0,0)$, $\mathbf{Q}_2^+ = (+4\pi/3, 0)$ and $\mathbf{Q}_2^- = (-4\pi/3, 0)$. Low-lying states have been tabulated in [37], however for $N = 36$ only in the sector $\mathbf{Q}_1 = (0,0)$. Fig. 12b shows our results for the low-lying states on the $N = 36$ lattice. Apparently, the QDJS are well separated from the other states and follow eq. (10) for $S \lesssim 4$. The lowest singlet excitation energy is above the first triplet excitation. A special feature of the $E(S)$ behavior of the QDJS is a deviation from the linearity starting in the vicinity of $S = N/6$. This comes from the Ising part of the Hamiltonian and is connected with distinguished Ising states having two spins up and one spin down per triangle [87,88] and results in a plateau in the magnetization versus external magnetic field curve (for a more detailed discussion, see section 6). However, this peculiarity emerging around $S(S+1) = 42$ in Fig. 12b is relevant only if $\sqrt{N} \lesssim N/6$, i.e. for small $N$.

The largest lattice considered has $N = 36$ sites and is defined by the edge vectors $(6,0); (0,6)$. It has GS energy per bond $E_0/{\rm bond} = -0.186791$, spin gap $\Delta = 0.344211$ and square of the order parameter $(m^+)^2 = 0.124802$ (cf. [37]). A detailed discussion of the spectra can be found in [31,36,37].

For the finite-size extrapolation of the GS energy (Fig. 20b), the spin gap and the order parameter (Fig. 21b) we use only even finite lattices of size $N = 24, 30, 36$. The extrapolation according to formulae (12), (13), (14) leads to the following results:

- GS energy per bond: $E_0/{\rm bond} = -0.1842$
  (for comparison: RVB [8]: $E_0/{\rm bond} = -0.154$; SWT [81]: $E_0/{\rm bond} = -0.1823$; former exact diagonalization [37]: $E_0/{\rm bond} = -0.1815$, Green's function Monte Carlo [84]: $E_0/{\rm bond} = -0.1819$; CCM [86]: $E_0/{\rm bond} = -0.1835$);

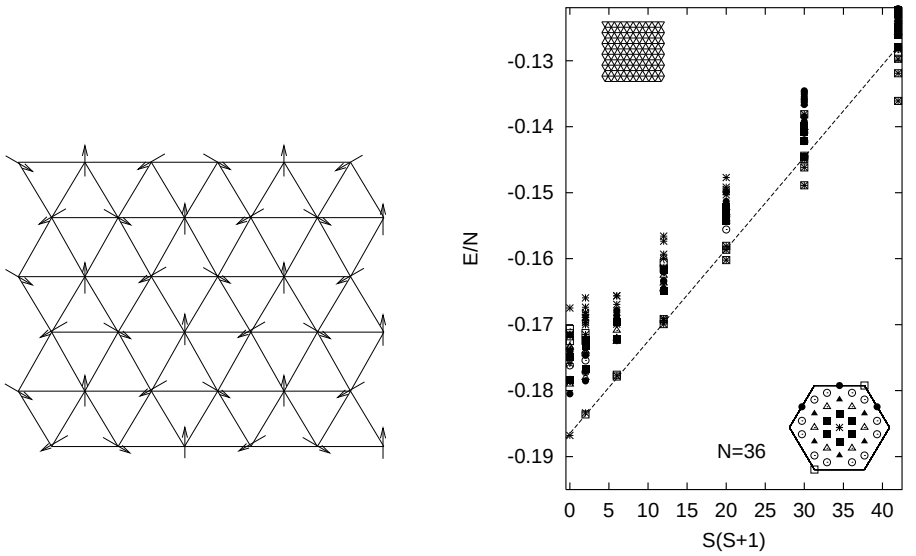


a b

**Fig. 12.** The HAFM on the triangular lattice (T1)
a: Classical GS b: Low-energy spectrum for $N = 36$ (the inset shows the $\mathbf{k}$ points in the Brillouin zone).

- spin gap: $\Delta = 0.1293$;
- order parameter: $m^+ = 0.1577 \sim 0.386\, m^+_{\rm class}$
  (for comparison: sublattice magnetization $m^{sl} = \langle S^z_i \rangle$ in linear SWT [81]: $m^{sl} = 0.2387 = 0.4774\, m^{sl}_{\rm class}$; Green's function Monte Carlo [84]: $m^{sl} = 0.205 = 0.41\, m^{sl}_{\rm class}$; CCM [86]: $m^{sl} = 0.2107 = 0.4214\, m^{sl}_{\rm class}$).

Obviously, the extrapolated gap is quite large, whereas the order parameter is smaller than that obtained by other means. This suggests stronger finite-size effects than for bipartite lattices. Nevertheless, the existence of semi-classical Néel LRO is not in question.

### The maple-leaf (T4) and the bounce (T7) lattices

The maple-leaf lattice [89] is obtained from the triangular lattice by a 1/7 depletion of sites. Its geometric unit cell contains six sites and the underlying Bravais lattice is a triangular one (cf. Fig. 13). It is also strongly frustrated but has lower coordination number ($z = 5$) than the triangular lattice. Furthermore, it has three non-equivalent NN bonds (solid, dashed and dotted lines in Fig. 5). Thus the quantum fluctuations might be more important and the HAFM on the maple-leaf lattice was considered as a candidate for a quantum paramagnet [90].

The bounce lattice is related to the maple-leaf lattice. It can be obtained from the maple-leaf lattice by bond depletion as described in section 2.2 (see Fig. 5). It has also a geometric unit cell with 6 sites, an underlying triangular Bravais lattice and contains two non-equivalent NN bonds. The coordination number $z = 4$ is lower than for the maple-leaf lattice but it is less frustrated, since the omitted bond was a frustrating one. As far as we know no antiferromagnetic material has, as yet, been synthesized with the lattice structure of tilings 4 or 7.

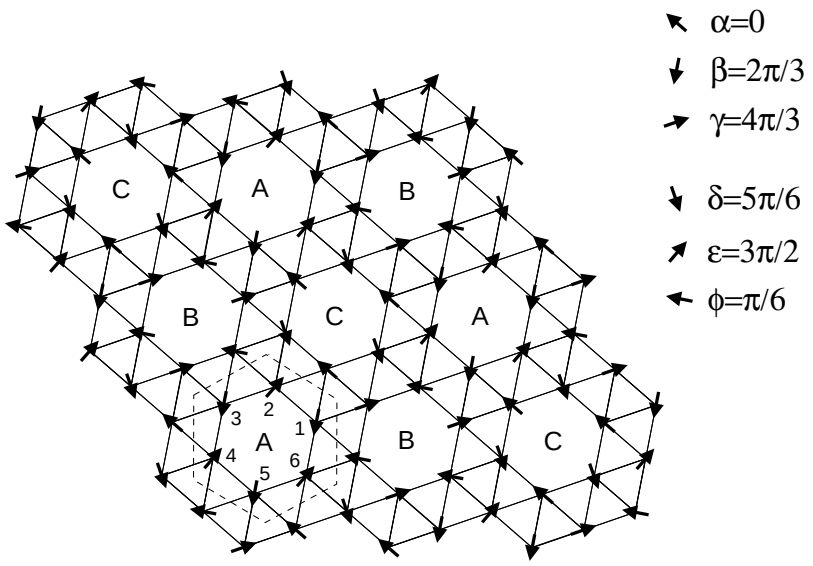


**Fig. 13.** The classical GS of the HAFM on the maple-leaf lattice (T4). The geometric unit cell is shown with dashed lines. The magnetic unit cell contains three geometric unit cells labeled by A,B,C.

The classical GS of the maple-leaf lattice is a six-sublattice Néel state shown in Fig. 13 with $E_0^{\rm class}/{\rm bond} = -s^2(\sqrt{3}+1)/5 = -0.13660$ and $m^+_{\rm class} = 0.39434$. The less frustrated bounce lattice has also a six-sublattice Néel GS with a 120° structure on each triangle and a collinear up-down structure on each hexagon leading to $E_0^{\rm class}/{\rm bond} = -2s^2/3 = -0.16667$ and $m^+_{\rm class} = 1/\sqrt{6} = 0.40825$. Both classical GSs break the translational symmetry of the lattice, the corresponding magnetic unit cell is three times as large as the geometric one and contains 18 sites. Therefore the applicability of finite-size calculations is particularly limited.

The low-lying spectra for both lattices with $N = 36$ sites are shown in Fig. 14. The lowest states in each sector of $S$ are QDJS belonging to appropriate symmetries $\mathbf{Q}_1 = (0, 0)$ and $\mathbf{Q}_2^+ = (+4\pi/3, 0)$, $\mathbf{Q}_2^- = (-4\pi/3, 0)$. They

follow eq. (10). The lowest singlet excitation energy is above the first triplet excitation.

The largest finite lattices considered have $N = 36$ sites and are defined by the edge vectors $(3, 0); (1, 2)$ for both tilings. Note that these finite lattices do not have the full symmetry of the corresponding infinite lattices. The $N = 36$ maple-leaf lattice has GS energy per bond $E_0/\text{bond} = -0.215589$, spin gap $\Delta = 0.400009$ and square of the order parameter $(m^+)^2 = 0.106101$. A picture of this lattice and a table of the correlation functions are given in [90]. The non-equivalent NN bonds lead to different NN correlations: $\langle \mathbf{S}_i \mathbf{S}_j \rangle_T = -0.1777$ (belonging to a dashed line in Fig. 5, middle), $\langle \mathbf{S}_i \mathbf{S}_j \rangle_H = -0.3656$ (belonging to a solid line in Fig. 5, middle) and $\langle \mathbf{S}_i \mathbf{S}_j \rangle_D = 0.0086$ (belonging to a dotted line in Fig. 5, middle).[8] It appears that the correlation functions of the quantum system fit quite well to the classical GS.

The $N = 36$ bounce lattice has GS energy per bond $E_0/\text{bond} = -0.286540$, spin gap $\Delta = 0.445138$ and square of the order parameter $(m^+)^2 = 0.119073$. The non-equivalent NN bonds lead to different NN correlations: $\langle \mathbf{S}_i \mathbf{S}_j \rangle_T = -0.1723$ (belonging to a dashed line in Fig. 5 right) and $\langle \mathbf{S}_i \mathbf{S}_j \rangle_H = -0.4008$ (belonging to a solid line in Fig. 5 right). The correlation function of the omitted bond (see Fig. 5) is $\langle \mathbf{S}_i \mathbf{S}_j \rangle_D = 0.1116$. It is obvious that the NN correlations $\langle \mathbf{S}_i \mathbf{S}_j \rangle_D$ and $\langle \mathbf{S}_i \mathbf{S}_j \rangle_H$ are enhanced by omitting the frustrating bond, whereas $\langle \mathbf{S}_i \mathbf{S}_j \rangle_T$ remains almost the same.

We use finite maple-leaf lattices and bounce lattices of size $N = 18$ and 36 for the finite-size extrapolation of the GS energy (Fig. 20b), the spin gap and the order parameter (Fig. 21b). By using formula (12), (13) and (14) we obtain for the maple-leaf lattice:

- GS energy per bond: $E_0/\text{bond} = -0.2137$
  (for comparison: SWT [90]: $E_0/\text{bond} = -0.20486$; variational [90]: $E_0/\text{bond} = -0.1988$);
- spin gap: $\Delta = 0.2548$;
- order parameter: $m^+ = 0.0860 \sim 0.218\, m^+_{\text{class}}$
  (for comparison: sublattice magnetization $m^{sl} = \langle S^z_i \rangle$ in SWT [90]: $m^{sl} = 0.154 = 0.308\, m^{sl}_{\text{class}}$).

An extrapolation of the gap based on a variational approach was presented in [90] and leads to $\Delta = 0.0180$.

The corresponding extrapolation for the bounce lattice yields:

- GS energy per bond: $E_0/\text{bond} = -0.2837$;
- spin gap: $\Delta = 0.2926$;
- order parameter: $m^+ = 0.1095 \sim 0.268\, m^+_{\text{class}}$.

[8] Note that these values and the corresponding values for the bounce lattice are averaged values, since the $N = 36$ lattices do not have all lattice symmetries of the infinite lattice. As a result one has to average over three different values for a certain correlation function.

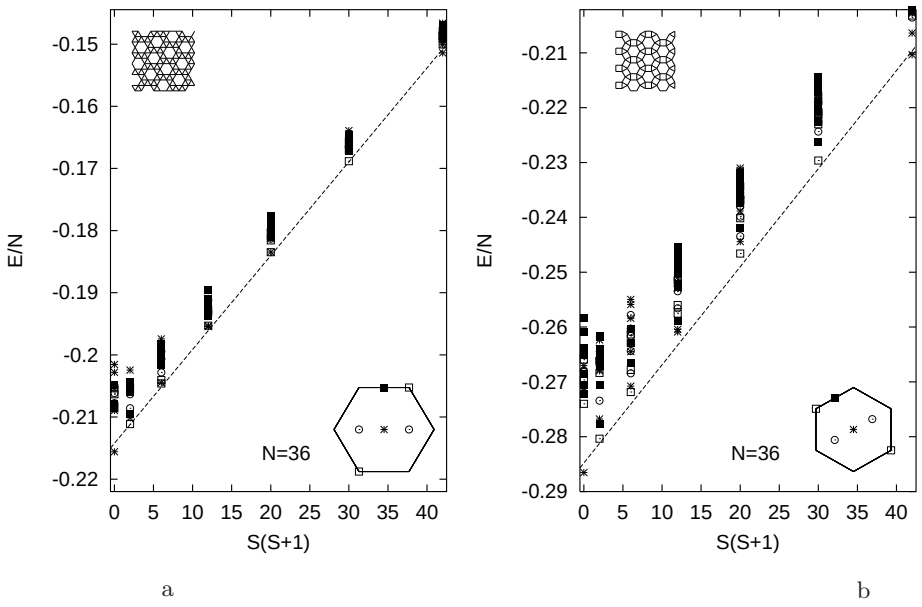


**Fig. 14.** Low-energy spectrum for HAFM on the maple-leaf (T4) and on the bounce (T7) lattice (the insets show the **k** points in the Brillouin zone). a: maple-leaf lattice with $N = 36$. b: bounce lattice with $N = 36$.

Obviously, the extrapolated order parameters are small but finite. The fact that the order parameter for the bounce lattice is larger than for the maple-leaf lattice seems to be related to the lower frustration. Taking into consideration results of the spin-wave theory and the variational approach presented for the maple-leaf lattice in [90] we conclude that the semi-classical six-sublattice Néel LRO survives for both lattices. However, this statement needs confirmation by further studies.

### The trellis lattice (T5)

The trellis lattice is to some extent exceptional since its structure corresponds to a system of coupled ladders or alternatively of coupled zigzag chains. Its geometric unit cell contains 2 sites (cf. Fig. 15a). It has the same coordination number $z = 5$ as the maple-leaf lattice but its frustration is slightly smaller (cf. Fig. 2). Furthermore, it has three non-equivalent NN bonds, labeled by $J_1$, $J_2$ and $J_3$ in Fig. 15a.

The HAFM on the trellis lattice is related to the magnetism of $SrCu_2O_3$, $CaV_2O_5$ and $MgV_2O_5$ [91, 92]. However, the $J_1$, $J_2$ and $J_3$ bonds are not of equal strength in these materials (for instance in $SrCu_2O_3$ the zigzag $J_1$ coupling is weak leading to a quasi-1D ladder structure). The classical GS is a Néel state for $J_2 < J_1/4$, and is an incommensurate spiral state along the

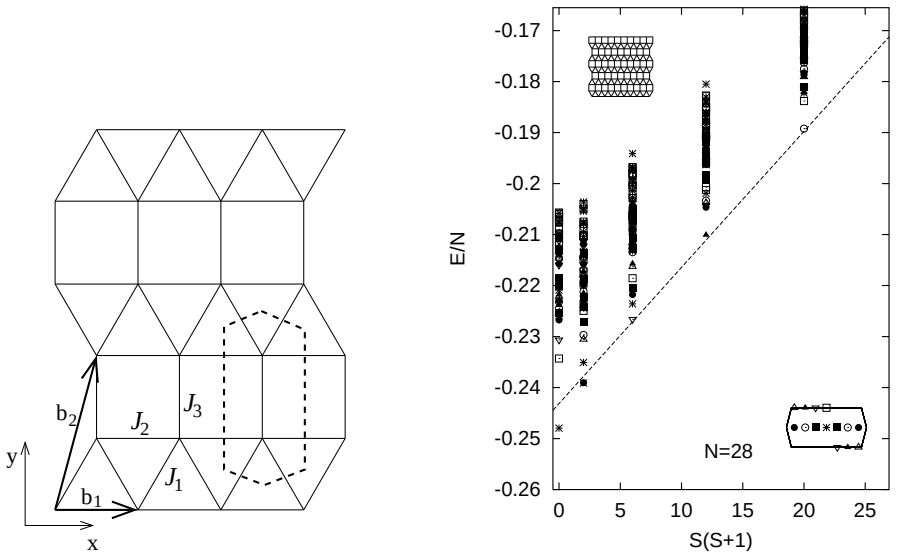


a b

**Fig. 15.** The trellis lattice (T5).
a: Illustration of the lattice with basis vectors $\mathbf{b}_1$ and $\mathbf{b}_2$, geometric unit cell (dashed) and the non-equivalent NN bonds $J_1$, $J_2$ and $J_3$. In the classical GS the spins form a spiral along the zigzag chains ($J_1$, $J_2$ bonds) whereas the spins along a $J_3$ bond are antiparallel.
b: Low-energy spectrum for $N = 28$ (the inset shows the $\mathbf{k}$ points in the Brillouin zone).

zigzag chains ($x$-direction) for $J_2 > J_1/4$, where the angles between neighboring bonds are $\alpha_2 = 2\arccos(J_1/4J_2)$ ($J_2$ bond), $\alpha_1 = \pi + \alpha_2/2$ ($J_1$ bond) and $\alpha_3 = \pi$ ($J_3$ bond). This leads to a classical GS with pitch angles $\alpha_1 = \pi + \arccos(1/4) = 1.41957\pi$; $\alpha_2 = 2\arccos(1/4) = 0.83914\pi$, GS energy per bond $E_0^{\rm class}/\text{bond} = -0.65s^2 = -0.1625$ and $m^+_{\rm class} = 0.39894$ for the perfect lattice ($J_1 = J_2 = J_3$).

The incommensurability of the classical GS creates additional difficulties applying exact diagonalization for finite lattices since the classical pitch angles $\alpha_1$ and $\alpha_2$ may be in conflict with periodic boundary conditions. In order to minimize this boundary effect we consider only finite lattices of $N = 20$, 28 and 36 sites having pitch angles $\alpha_2^{(N)}$ deviating by not more than 6% from the true values $\alpha_2$. The $N = 36$ lattice is defined by the edge vectors $(9, 0); (-1, 2)$ and has a pitch angle $\alpha_2^{(36)} = 1.059\alpha_2$. Its GS energy per bond is $E_0/\text{bond} = -0.247578$, spin gap $\Delta = 0.605227$ and square of the order parameter $(m^+)^2 = 0.109897$. The three non-equivalent NN correlations functions for $N = 36$ are

$\langle \mathbf{S}_i\mathbf{S}_j\rangle_{J_1} = -0.098835$, $\langle \mathbf{S}_i\mathbf{S}_j\rangle_{J_2} = -0.283938$ and $\langle \mathbf{S}_i\mathbf{S}_j\rangle_{J_3} = -0.472341$ (cf. Fig. 15a).

In Fig. 15b the QDJS are shown. Although the boundary conditions are not perfect it can be seen that the QDJS are separated from the other states and follow approximately eq. (10). The lowest singlet excitation is above the first triplet excitation. The translational symmetry of the QDJS is more complex than in the other lattices. It is connected with the $\mathbf{q}$ vector of the spiral state. We find $Q_y = 0, \pi$ and $Q_x = 6\pi(N/2 - S)/7 \bmod 2\pi$ for $N = 28$ and $Q_x = 8\pi(N/2 - S)/9 \bmod 2\pi$ for $N = 36$.

For the finite-size extrapolation of the GS energy (Fig. 20b), the spin gap and the order parameter (Fig. 21b) we use finite lattices of size $N = 20, 28, 36$. The extrapolation according to formulae (12), (13), (14) leads to the following results:

- GS energy per bond: $E_0/\text{bond} = -0.2471$;
- spin gap: $\Delta = 0.49$;
- order parameter: $m^+ = 0.0885 \sim 0.222\, m^+_{\text{class}}$.

Although our data do not allow a secure conclusion the results are in favor of a spiral long-range ordered phase. This conclusion is in agreement with the findings in [91] based on a Schwinger boson technique and linear spin-wave theory.

### The SrCuBO lattice (T6)

The SrCuBO lattice is weakly frustrated, has four sites in the geometric unit cell and two non-equivalent NN bonds $J_1$ and $J_2$ (see Fig. 16a, top). It can be transformed by an appropriate distortion to a square lattice with one diagonal bond in each second square (see Fig. 16a, bottom). This frustrated square lattice is known as Shastry-Sutherland model [93,94] introduced in the 80ties as a 2D spin half HAFM with an exactly known quantum GS. Indeed for large frustrating $J_2$ the GS is a so-called orthogonal dimer product state with dimer singlets on each $J_2$ bond. Although the Shastry-Sutherland model initially was understood as a 'toy model' it has attracted much renewed attention as it provides a representation of the magnetic properties of the recently discovered 2D spin gap system $SrCu_2(BO_3)_2$ [5,95]. The experimental findings stimulated a series of theoretical studies for the spin half HAFM on the SrCuBO lattice with varying bonds $J_1$, $J_2$, see Refs. [96–104] and the recent review [105]. We will discuss the GS phase diagram in the $J_1 - J_2$ plane below in section 5. In this section we consider $J_1 = J_2$, only. In this case the classical GS is the two-sublattice Néel state with energy per bond $E_0^{\text{class}}/\text{bond} = -0.6s^2 = -0.15$ and with order parameter $m^+_{\text{class}} = 0.5$. The geometric unit cell of the SrCuBO lattice contains four sites and the translational symmetry of the lattice and of the classical Néel GS fit to each other. The spectrum of the SrCuBO lattice (Fig. 16b) is therefore comparable with that of the honeycomb lattice (Fig.

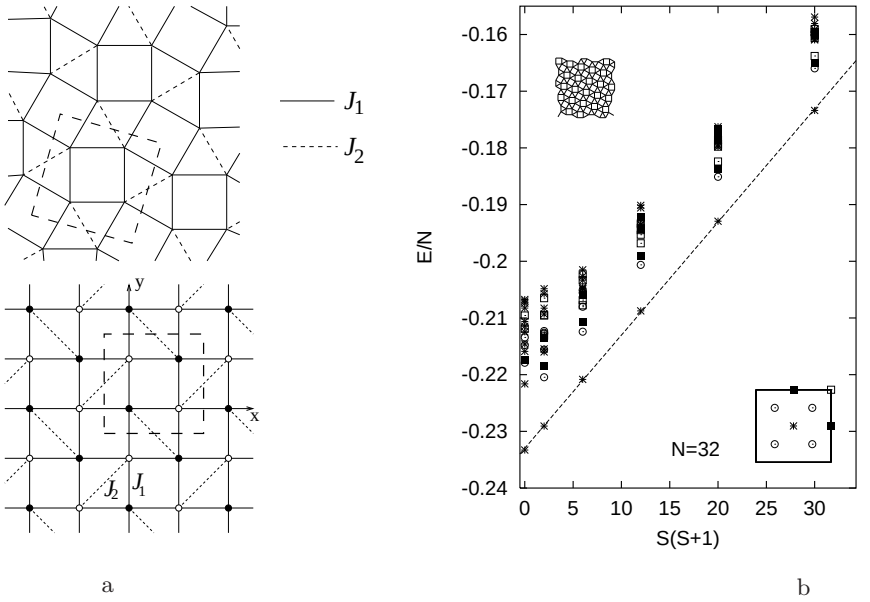


**Fig. 16.** The SrCuBO lattice (T6). a: Comparison of the SrCuBO lattice (above) and the Shastry-Sutherland model (below). The unit cell is illustrated by the dashed square.
b: Low-energy spectrum for $N = 32$ (the inset shows the $\mathbf{k}$ points in the Brillouin zone).

9). The QDJS are well separated from the other states and follow eq. (10). The lowest singlet excitation is above the first triplet.

The largest lattice considered with $N = 36$ sites is defined by the edge vectors $(3, 0); (0, 3)$ and has GS energy per bond $E_0/\text{bond} = -0.233410$, spin gap $\Delta = 0.319735$ and square of the order parameter $(m^+)^2 = 0.169048$, that is 80% of the order parameter of the corresponding square lattice. The two non-equivalent NN correlations functions for $N = 36$ are $\langle \mathbf{S}_i \mathbf{S}_j \rangle_{J_1} = -0.332886$ (almost the same as for the square lattice) and $\langle \mathbf{S}_i \mathbf{S}_j \rangle_{J_2} = 0.164493$.

For the finite-size extrapolation of the GS energy (Fig. 20b), the spin gap and the order parameter (Fig. 21b) we use finite lattices of size $N = 20$, 32 and 36. The extrapolation according to formulae (12), (13), (14) leads to the following results:

- GS energy per bond: $E_0/\text{bond} = -0.2310$
  (for comparison: series expansion [96]: $E_0/\text{bond} = -0.231$; Schwinger boson mean field [94]: $E_0/\text{bond} = -0.231$; CCM [106]: $E_0/\text{bond} = 0.2311$);
- spin gap: $\Delta = 0.0927$;

- order parameter: $m^+ = 0.2280 \sim 0.456\, m^+_{\rm class}$
  (for comparison: series expansion [96]: $m^+ = 0.200$; Schwinger boson mean field [94]: $m^+ = 0.203$; CCM [106]: $m^+ = 0.211$).

Due to frustration the order parameter is only about 70% of that of the square lattice but it is the largest one of all frustrated lattices. There is no doubt of semi-classical GS Néel order for this lattice. This conclusion is in agreement with several other studies like series expansion [96,97,99] and bosonic representations [94,104]. However, the Néel LRO is destroyed by further increasing the frustrating bond $J_2$ (see section 5).

### 4.3 Absence of semi-classical LRO on frustrated lattices - the kagomé (T8) and the star (T9) lattices

Among the non-bipartite frustrated lattices the kagomé[9] and the star lattice play an exceptional role. The kagomé lattice is strongest frustrated (as strong as the triangular lattice) and has low coordination number $z = 4$, cf. Fig. 17. It can be obtained by a 1/4 site depletion or alternatively by a 1/3 bond depletion (with an appropriate subsequent distortion) of the triangular lattice. Whereas the triangles in the kagomé lattice are corner sharing, they are separated by a dimer in the star lattice. Its degree of frustration is less than for the kagomé lattice but it has an even lower coordination number $z = 3$ and two non-equivalent NN bonds $J_D$ and $J_T$, cf. Fig. 18. As indicated in Fig. 3, the star lattice can be obtained by a 2/5 bond depletion of the maple-leaf (T4) or alternatively by a 1/4 bond depletion of the bounce lattice (T7) with an appropriate subsequent distortion. Both the kagomé and the star lattices are characterized by strong quantum fluctuations.

After realizing in the early nineties that the quantum GS of the HAFM on the triangular lattice is Néel ordered the HAFM on the kagomé lattice came into the focus of interest as a hot candidate for a 2D quantum spin system with an exotic non-Néel ordered GS [36,38,39,86,108–120]. Indeed, most of the recent investigations are in favor of a quantum paramagnetic GS, although its nature is far from being well understood. A possible physical realization of the kagomé HAFM is SrCrGa oxide, which is, however, a layered kagomé HAFM with spin 3/2 [121,122]. A novel spin-1/2 kagomé like HAFM has been found recently in volborthite $Cu_3V_2O_7(OH)_2 \cdot 2H_2O$ [123]. By contrast, the spin half HAFM on the star lattice has not been considered in the literature so far, nor is a physical realization currently known. However, we mention that a projection of the three-dimensional non-frustrated magnetic compound green dioptase $Cu_6Si_6O_{18} \cdot 6H_2O$ has the shape of the star lattice [124].

The geometric unit cell of the kagomé (star) lattice contains three (six) sites and the underlying Bravais lattice is a triangular one (cf. Figs. 17 and 18). The classical GS for the kagomé lattice was studied in [125–127]. In analogy to

[9] The name kagomé stems from the Japanese language and means a bamboo-basket woven pattern [107].

the triangular lattice the angle between neighboring spins is 120°. Its energy per bond is $E_0^{\text{class}}/\text{bond} = -s^2/2 = -0.125$. However, in contrast to the triangular lattice there is a non-trivial infinite degeneracy of the classical GS typical for a classical HAFM with corner-sharing triangles.

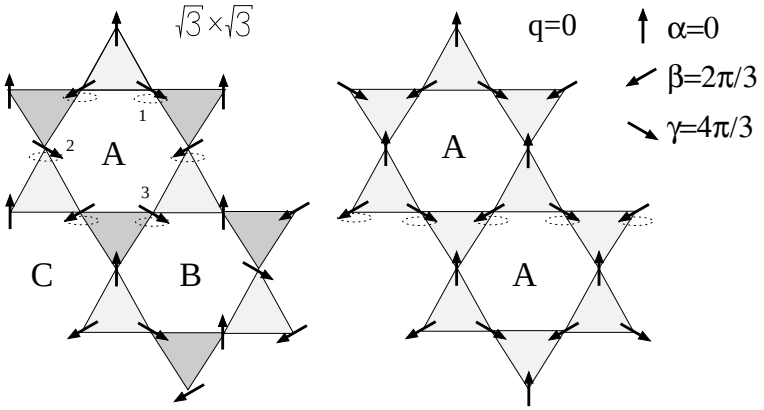


**Fig. 17.** Two variants of the GS of the classical HAFM on the kagomé lattice (T8): the $\sqrt{3}\times\sqrt{3}$ state (left) and the $q$=0 state (right). The dotted ellipses show further degrees of freedom of the highly degenerate classical GS. The Wigner-Seitz geometrical unit cell contains three sites (A1, A2, A3). The light and gray triangles symbolize different chiralities.

In the classical GS of the star lattice the two non-equivalent NN bonds carry different NN spin correlations: the angle between neighboring spins on dimer bonds $J_D$ is 180°, whereas the angle on triangular bonds $J_T$ is 120°. Its energy per bond is $E_0^{\text{class}}/\text{bond} = -2s^2/3 = -0.1667$. Although the star lattice is not built by corner-sharing triangles, the classical GS for this lattice also exhibits a non-trivial infinite degeneracy very similar to that of the kagomé lattice.

Two particular variants of the classical GS characterized by a certain wave vector are shown in Figs. 17 and 18. The states on the left side of Figs. 17 and 18 exhibit the same symmetry as the classical GS for the triangular lattice having a magnetic unit cell three times as large as the geometric unit cell (so-called $\sqrt{3}\times\sqrt{3}$ state). The states on the right side of Figs. 17 and 18 have the same translational symmetry as the lattice (so-called $q = 0$ state) and therefore the magnetic and the geometric unit cell are identical. Both states are highly degenerate as indicated by the dotted elliptic lines at the top of spins.

Let us consider the order parameter (9) for the classical GS. If we take the perfect ordered planar $\sqrt{3}\times\sqrt{3}$ and $q$=0 state, then we get for both lattices $m^+_{\text{class},\sqrt{3}\times\sqrt{3}} = m^+_{\text{class},q=0} = \frac{1}{2}\sqrt{2/3} = 0.40825$. However, one has to take

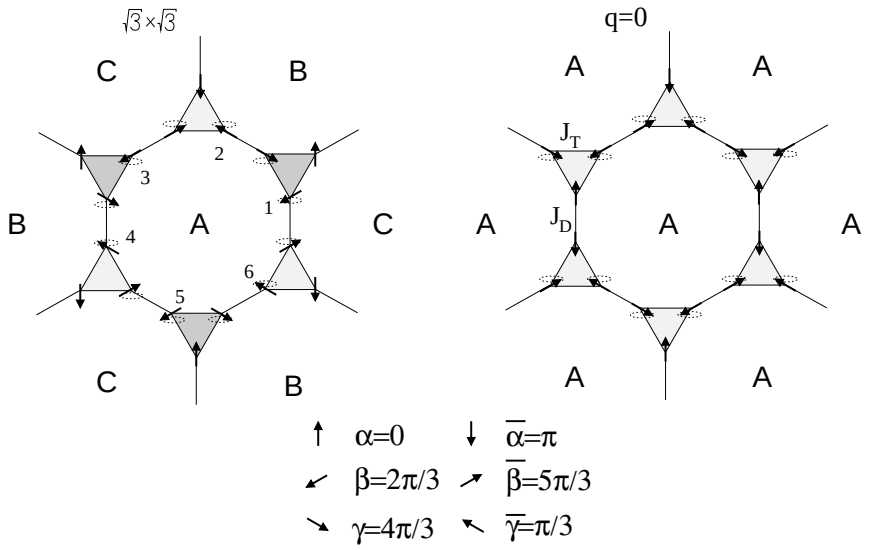


**Fig. 18.** Two variants of the GS of the classical HAFM on the star lattice (T9): the $\sqrt{3}\times\sqrt{3}$ state (left) and the $q$=0 state (right). The dotted ellipses show further degrees of freedom of the highly degenerate classical GS. The Wigner-Seitz geometrical unit cell consists of six sites located on a hexagon (sites A1,..., A6). The light and gray triangles symbolize different chiralities.

into account the high degeneracy of the GS. In order to average over these degenerate states we performed numerical calculations of the ground states for classical systems of up to $N = 432$ sites. The numerical results lead to the conclusion that for large $N$ we have $m^+_{\mathrm{class,averaged}} = 0.25$ for both lattices. This corresponds to a GS phase with decoupled spins for larger spin-spin separations.

In the quantum case the largest kagomé lattice considered has $N = 36$ sites and is defined by the edge vectors $(4, 2); (2, 4)$. It has GS energy per bond $E_0/\mathrm{bond} = -0.219188$, spin gap $\Delta = 0.164190$ and square of the order parameter $(m^+)^2 = 0.059128$. We mention that the result for $E_0/\mathrm{bond}$ was already given in [39, 111].

The largest star lattice considered has $N = 36$ sites and is defined by the edge vectors $(2, 0); (1, 3)$. It has GS energy per bond $E_0/\mathrm{bond} = -0.310348$, spin gap $\Delta = 0.480343$ and square of the order parameter $(m^+)^2 = 0.082299$. Note that the value of the spin gap is particularly large. The only $N = 36$ lattice having a larger spin gap is the trellis lattice for which, however, the large spin-gap is most likely a finite-size artifact due to the incommensurate structure of the states. The two non-equivalent NN correlation functions for

$N = 36$ are $\langle \mathbf{S}_i \mathbf{S}_j \rangle_{J_T} = -0.170339$ (that is weaker than for the kagomé and the triangular lattice) and $\langle \mathbf{S}_i \mathbf{S}_j \rangle_{J_D} = -0.590367$.[10] We mention that the NN correlation $\langle \mathbf{S}_i \mathbf{S}_j \rangle_{J_D}$ is the strongest correlation we found in all lattices, thus indicating a strong tendency to form local singlets on the $J_D$ bonds.

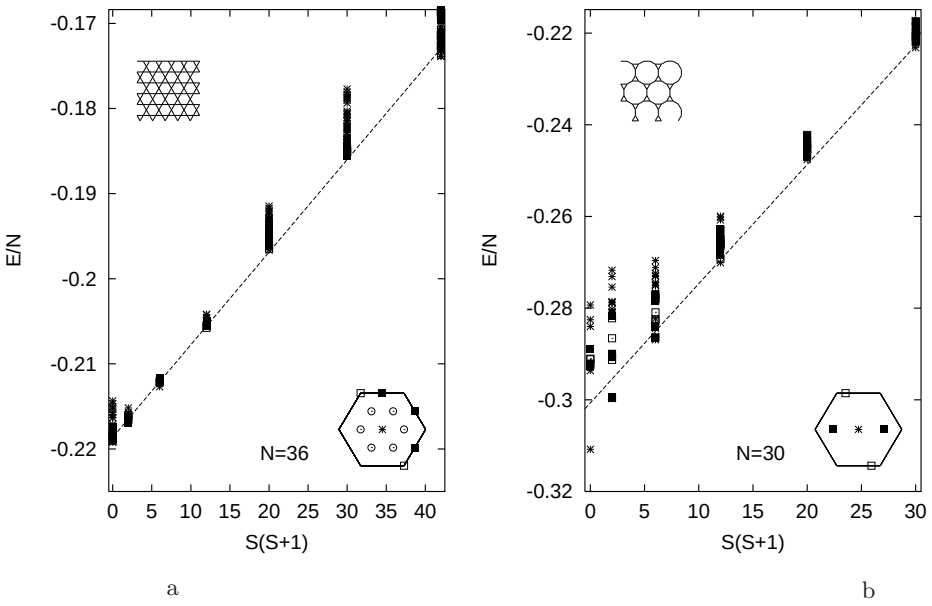


**Fig. 19.** Low-energy spectrum for HAFM on the kagomé (T8) and on the star (T9) lattice (the insets show the **k** points in the Brillouin zone).
a: kagomé with $N = 36$. b: star with $N = 30$.

The spectra of both lattices are shown Fig. 19. For both spectra it is obvious that the lowest states $E_{\min}(S)$ are not well described by eq. (10). In particular, the lowest states belonging to $S = 0$ and $S = 1$ deviate significantly from a straight line. We do not see well separated QDJS as well as spin-wave excitations. Furthermore, the symmetries of the lowest states in each sector of $S$ cannot be attributed to the classical $\sqrt{3}\times\sqrt{3}$ or $q$=0 ground states in general. The kagomé lattice is an exceptional case in that a large number of non-magnetic singlets fill the singlet-triplet gap. For instance for $N = 27$ there are 153 [39] and for $N = 36$ on finds 210 [11] non-magnetic excitations within the spin gap and in the thermodynamic limit possibly a gapless singlet continuum. This unusual number of low-lying singlets is attributed to the non-trivial huge degeneracy of the classical GS. By contrast, the star lattice does

[10] Note that these values are averaged values, since the $N = 36$ star lattice does not have all lattice symmetries of the infinite lattice. As a result one has to average over two different values.

not show low-lying singlets. This can be attributed to the special property of the quantum GS to form local singlets on the $J_D$ bonds which somehow makes the singlet GS of the star lattice exceptional. As a consequence, the quantum GS of the star lattice has lowest energy per bond among all frustrated lattices and is well separated from the excitations. Especially the first singlet excitation has comparably high energy.

We mention that a detailed discussion of the spectrum for the kagomé lattice was given in [38, 39].

For the finite-size extrapolation of the GS energy (Fig. 20b), the gap and the order parameter (Fig. 21b) we use finite lattices of size $N = 12$, 18, 24, 30 and 36 (kagomé) and of $N = 18$, 24, 30 and 36 (star). The extrapolation leads to the following results for the kagomé lattice:

- GS energy per bond: $E_0/\text{bond} = -0.2172$
  (for comparison: SWT [109]: $E_0/\text{bond} = -0.2353$; former exact diagonalization ($N = 9, \ldots, 21$) [108]: $E_0/\text{bond} = -0.217$; CCM [86]: $E_0/\text{bond} = -0.2126$; Green's function decoupling [115, 120]: $E_0/\text{bond} = -0.215$);
- spin gap: $\Delta = 0.0397$;
- order parameter: $m^+ = 0.000 \sim 0.0\ m^+_{\text{class}}$.

In fact, the extrapolation gives the unphysical value $m^+ = -0.0146 < 0$ (cf. Fig. 21b). We interpret this as vanishing order parameter.

For the star lattice we obtain:

- GS energy per bond: $E_0/\text{bond} = -0.3093$;
- spin gap: $\Delta = 0.3809$;
- order parameter: $m^+ = 0.0385 \sim 0.094 \ldots 0.150\ m^+_{\text{class}}$ (the first value corresponds to $m^+_{\text{class}} = 0.40825$ of the perfect ordered planar $\sqrt{3}\times\sqrt{3}$ and $q$=0 classical GS, see Fig. 18, whereas the second value corresponds to $m^+_{\text{class,averaged}} = 0.25$ obtained by averaging over all degenerate classical ground states).

The extrapolated spin gap for the kagomé lattice is small but finite and corresponds to the values reported in the literature (see e.g. [12]), but we should remark that the existence of a spin gap at all is not a fully secure statement.

For both lattices the exact diagonalization data yield indications for a quantum paramagnetic GS. For the kagomé lattice this statement is known from detailed studies by C. Lhuillier, H.-U. Everts and coworkers as well as other groups published over the last 10 years. However, the star lattice represents a new example for a quantum HAFM on a uniform 2D lattice without semi-classical GS ordering. We emphasize that the quantum paramagnetic GS for the star lattice is different in nature to the quantum GS for the kagomé lattice. The quantum GS for the star lattice is characterized by an extremely strong NN correlation on the dimer bonds (more than 60% larger than the NN correlation of the honeycomb lattice having the same coordination number $z = 3$) and a weak NN correlation on the triangular bonds (only about 30% of the NN dimer correlation and significantly weaker than the triangular

NN correlation of the kagomé and the triangular lattices). The singlet-triplet spin gap is particularly large (about ten times larger than that for the kagomé lattice). Although the classical GS exhibits a huge non-trivial degeneracy, remarkably one does not find low-lying singlets within this large spin gap, rather the first singlet excitation is well above the lowest triplet state. The low-lying spectrum as a whole resembles the spectrum of weakly coupled dimers [18]. All these features support the conclusion that the quantum GS of the HAFM on the star lattice is dominated by local singlet pairing and represents a so-called valence-bond crystal state (see also section 4.4).

### 4.4 Summary and comparison

Based on extensive exact diagonalization studies and on available results in the literature we discuss the GS ordering of the spin half HAFM on the 11 uniform Archimedean tilings in two dimensions. Of course we are not able to clarify all aspects of the GS properties of these quantum many-body systems. Nevertheless the comparative discussion of the 11 lattices leads to conclusions on the influence of lattice structure on GS magnetic ordering in two dimensions and this way on the existence or absence of semi-classical LRO in these systems.

The HAFM has been already studied intensively in the literature for some of these lattices (square (T2), triangular (T1), honeycomb (T3), kagomé (T8), SrCuBO (T6), CaVO (T11)) and the physical picture seems to be more or less clear for those lattices. For some other lattices (SHD (T10), maple-leaf (T4) and trellis (T5)) only a few results are available in the literature so far and the conclusions on the GS ordering are less reliable. The HAFM on the star lattice (T9) as well as on the bounce lattice (T7) has not been studied till now.

Let us summarize the results of the preceding sections: The GS of the spin half HAFM on the bipartite (i.e. non-frustrated) lattices is semi-classically Néel ordered. The reduction of the order parameter by quantum fluctuations depends on the coordination number and on the competition of non-equivalent NN bonds (cf. table 3). The low-energy spectra exhibit some typical features for magnetic systems with semi-classical order, namely well separated quasi-degenerate joint states (QDJS) with symmetries belonging to the classical GS ordering. Another indication for semi-classical ordering is the disappearance of the spin gap in the thermodynamic limit. We find, at least for the lattices with not too large unit cells, indications for a vanishing spin gap. However, the finite-size extrapolation of the spin gap is less reliable than for the magnetization (see section 3.3) and therefore we do not consider the spin gap as a main criterion for the existence of semi-classical LRO. The comparison of the finite-size behavior of the GS energy shown in Fig. 20 shows that the extrapolation coefficient $A_3$ (cf. eq. (12)) for the bipartite lattices is largest in agreement with long-ranged spin-spin correlations. We mention that a suppression of semi-classical LRO in bipartite lattices can appear in systems with NN bonds

of different strength this way increasing the competition of non-equivalent NN bonds (see section 5).

**Table 3.** Comparison of the ground-state energy per bond $E_0$/bond and the order parameter $m^+$ (eq. (9)) of the spin half HAFM obtained by finite-size extrapolation (see text). In order to see the effect of quantum fluctuations, we present $m^+$ scaled by its corresponding classical value $m^+_{\rm class}$. Furthermore, we show the coordination number $z$ and indicate, whether all NN bonds are equivalent or not by EQ and NEQ, respectively. For the star lattice (last row) the first value corresponds to $m^+_{\rm class}$ of the perfect ordered planar $\sqrt{3}\times\sqrt{3}$ and $q$=0 classical GS, see Fig. 18, whereas the second value corresponds to $m^+_{\rm class}$ averaged over all degenerate classical ground states.

| tiling | $z$ | NN bonds | $E_0$/bond | $m^+/m^+_{\rm class}$ |
|---|---|---|---|---|
| *bipartite* | | | | |
| square (T2) | 4 | EQ | −0.3350 | 0.635 |
| honeycomb (T3) | 3 | EQ | −0.3632 | 0.558 |
| CaVO (T11) | 3 | NEQ | −0.3689 | 0.461 |
| SHD (T10) | 3 | NEQ | −0.3713 | 0.425 |
| *frustrated* | | | | |
| SrCuBO (T6) | 5 | NEQ | −0.2310 | 0.456 |
| triangular (T1) | 6 | EQ | −0.1842 | 0.386 |
| bounce (T7) | 4 | NEQ | −0.2837 | 0.286 |
| trellis (T5) | 5 | NEQ | −0.2471 | 0.222 |
| maple-leaf (T4) | 5 | NEQ | −0.2171 | 0.218 |
| kagomé (T8) | 4 | EQ | −0.2172 | 0.000 |
| star (T9) | 3 | NEQ | −0.3093 | 0.094 . . . 0.150 |

The situation for the frustrated lattices is more complex. Some of the criteria for semi-classical LRO might be weaker pronounced. For the HAFM on the kagomé and on the star lattice we find evidence for a quantum paramagnetic GS whereas for the other frustrated lattices there are indications for semi-classical LRO. Although the order parameter $m^+$ is additionally weakened by the interplay of quantum fluctuations and frustration the extrapolated values of $m^+$ remain finite (between 22% and 45% of the classical values) for the tilings T1,T4,T5,T6,T7. It vanishes however for the kagomé lattice and is at least very small for the star lattice (see table 3). Except for the kagomé and the star lattices the low-energy spectra exhibit some typical features for magnetic systems with semi-classical order, namely well separated QDJS with symmetries belonging to the classical GS ordering. The comparison of the finite-size behavior of the GS energy (Fig. 20) shows the smallest extrapolation coefficient $A_3$ for the kagomé and the star lattice being in agreement with short-range spin-spin correlations. Although the extrapolation coefficient

$A_3$ is very small for the trellis lattice, too, we interpret this as a particular finite-size effect due to the incommensurate structure of the classical GS.

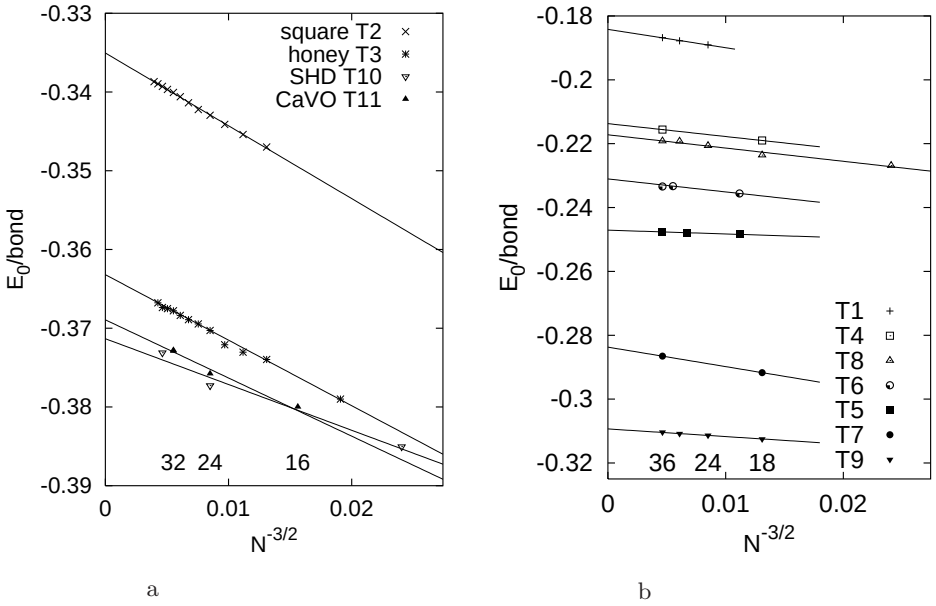


**Fig. 20.** Finite-size extrapolations of GS energy per bond $E_0$/bond, a - bipartite lattices, b - frustrated lattices.

We conclude that the interplay of lattice structure and quantum fluctuations may lead to a non-classical quantum paramagnetic singlet GS for frustrated lattices with low coordination number and strong frustration, i.e. for the kagomé and the star lattice (see Fig. 22). Although extensive studies have been performed for the kagomé lattice [36, 38, 39, 86, 108–120], the spin half HAFM on the star lattice is considered in this article for the first time. By contrast with all the other lattices, the kagomé and the star lattice show a huge non-trivial degeneracy of the classical GS due to strong frustration.

Although there is no semi-classical GS order for both lattices, the nature of both quantum ground states is basically different in the quantum case. We argue that the origin for this difference lies in the existence of non-equivalent NN bonds in the star lattice whereas all NN bonds in the kagomé lattice are equivalent. That leads also to significant differences in the low-lying spectrum of both lattices. The kagomé lattice has probably a finite spin gap, but within this spin gap a large number (increasing exponentially with system size) of low-lying singlets appear [38, 39, 113] which seem to be a remnant of the non-trivial classical GS degeneracy. However, the HAFM on the star lattice has a particularly large spin gap but also a well pronounced singlet-singlet gap (even

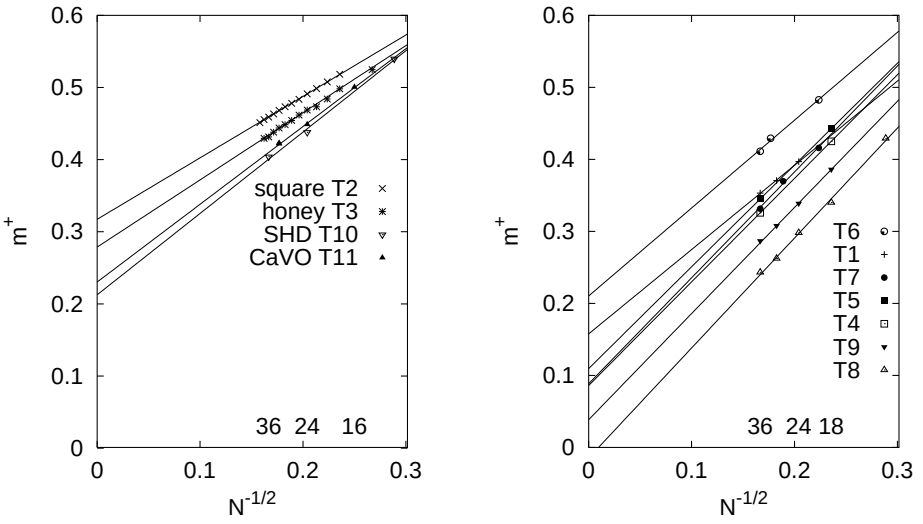


**Fig. 21.** Finite-size extrapolations of $m^+$, a - bipartite lattices, b - frustrated lattices.

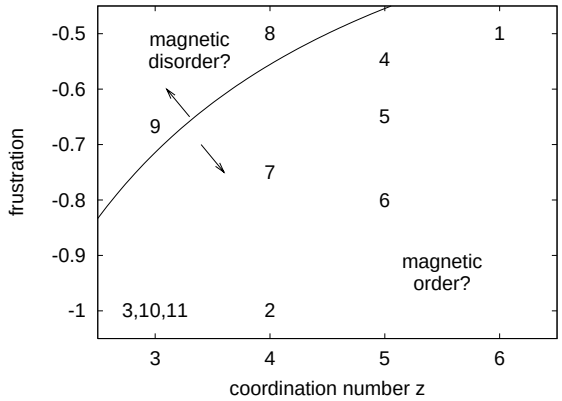


**Fig. 22.** Border line between semi-classical magnetic order and quantum magnetic disorder in a parameter space spanned by frustration (classical GS energy per bond divided by $s^2$, see section 2.1) and coordination number $z$. The numbers indicate the location of the Archimedean tilings in this parameter space.

larger than the spin gap) which is in accord with a GS dominated by local singlet pairing on non-equivalent NN $J_D$ bonds assisted by frustration. As a consequence, the huge classical GS degeneracy has no remnant in the spectrum of the quantum model. We mention that the checkerboard (planar pyrochlore) lattice is another example, where the non-trivial classical GS degeneracy does not lead to a continuum of low-lying singlets and the ground-state is most likely a valence bond crystal (see e.g. [128, 129]). Furthermore, examples are known that many low-lying non-magnetic excitations within the spin gap may appear although the classical GS is not non-trivially degenerate [41, 130].

For all the other bipartite and frustrated lattices the quantum fluctuations seem to be not strong enough to destroy the classical order. However, we should again emphasize that our conclusions about semi-classical LRO possesses some uncertainty, in particular for the trellis, maple-leaf and bounce lattices.

The above presented study provides some criteria for the appearance of novel quantum ground states in 2D spin systems. Although only for a few of the lattices under consideration direct realizations in real materials have been found till now, in several cases slightly modified models, e.g. models with NN couplings of non-equal strength or with inclusion of next-nearest neighbor couplings, are appropriate for the description of real magnetic substances.

At the end of this paragraph we will classify the magnetic ordering on the 11 Archimedean tilings using the four basic types of low-energy physics in 2D isotropic quantum antiferromagnets proposed and described recently by Lhuillier, Sindzingre, Fouet and Misguich [11–15]. The first type of GS phases is the semi-classical LRO (collinear or noncollinear). Most of the lattices belong this class, namely all bipartite lattices (T2,T3,T10,T11) but also the frustrated tilings (T1,T4,T5,T6,T7). The GS of the HAFM on these lattices breaks the $SU(2)$ symmetry. The low-lying excitations are gapless Goldstone modes (magnons). As discussed above, the order parameter is reduced by quantum fluctuations. The three other types of GS phases, namely the so-called valence bond crystal, type I spin liquid and type II spin liquid are purely quantum.

The so-called valence bond crystal is a phase characterized by the formation of local singlets with high binding energy built by an even number of spins (most likely by two or four spins) connected by NN bonds (singlet 'valence bonds'). The correlation between the singlets is weak leading to a fast exponential decay of the spin pair correlation to zero. The GS is a rotationally invariant singlet of the total spin without $SU(2)$ symmetry breaking. However, breaking of translational symmetry of the lattice is possible but not necessary. The valence bond crystal possesses long-range singlet-singlet (dimer-dimer or plaquette-plaquette) correlations. All excitations above the GS are gapped leading to an exponential (i.e. thermally activated) low-temperature behavior of the specific heat $c$ and of the susceptibility $\chi$. A candidate for such a GS phase is the HAFM on the star lattice. For this lattice the possible dimer-dimer LRO would fit to the lattice geometry. Another candidate is the $J_1 - J_2$

model on the square lattice, widely discussed in the literature (see [85, 131] and references therein), where the valence bond crystal phase would break the translational symmetry of the lattice. The type I spin liquid has some similarity to the valence bond crystal. It has also a rotationally invariant singlet GS without $SU(2)$ symmetry breaking, it has a fast exponential decay of the spin pair correlation to zero and gapped excitations leading to thermally activated low-temperature behavior of $c$ and $\chi$. However, the GS does not possess singlet-singlet long-ranged correlations but is likely to be characterized by short ranged resonating valence bonds. There is no good candidate for this phase among the Archimedean tilings. But this phase might be realized in the $J_1 - J_2$ model on the honeycomb lattice [42]. The type II spin liquid has also a rotationally invariant singlet GS, a fast exponential decay of the spin pair correlation to zero and no long-ranged singlet-singlet correlations. The spin gap $\Delta$ to the first triplet excitation is finite giving rise to a thermally activated low-temperature behavior of the susceptibility $\chi$. However, there is a gapless continuum of singlets which could be described by a family of short-ranged valence bond states [116] the number of which is exponentially growing with size $N$. This gapless continuum implies that the system has a zero-temperature residual entropy and that the low-temperature specific heat is not thermally activated. The best candidate for this type of spin liquid is the spin half HAFM on the kagomé lattice.

## 5 Quantum phase transitions in 2D HAFM - the CaVO $J - J'$ model and the Shastry-Sutherland model

Phase transitions have been a subject of great interest to physicists over many decades. Besides thermal phase transitions, the so-called quantum phase transitions (or zero-temperature transitions) have started to attract a lot of attention (see chapter by S. Sachdev in this book). For zero-temperature order-disorder transitions we basically need the interplay between the interparticle interactions and quantum fluctuations. Canonical models to discuss quantum phase transitions are quantum spin models. As discussed above the HAFM on most of the 2D lattices possesses semi-classical LRO in the GS, but the interplay of quantum fluctuations and strong competition between bonds may suppress this order. The competition may appear either as frustration or by non-equivalent NN bonds or a combination of both. Indeed, the strength of this competition may serve as the control parameter of a zero-temperature order-disorder transition. It can be tuned by changing the relative magnitude of non-equivalent NN bonds or by introducing next-nearest neighbor bonds. The Archimedean tilings therefore represent a wide playground for the investigation of zero-temperature transitions.

A generic model of a frustrated HAFM widely discussed in the literature (see, e.g., Refs. [55, 85, 131–138]) is the spin-half $J_1 - J_2$ model on the square lattice, where the frustrating $J_2$ bonds plus quantum fluctuations are believed

to lead to a second-order transition from a Néel-ordered state to a quantum paramagnetic state at about $J_2 \approx 0.38 J_1$. The properties of the latter state are still far from being understood. One favored quantum phase for $J_2 \sim 0.5 J_1$ is a valence bond crystal. However, there are examples where frustration leads to a first-order transition in quantum spin systems in contrast to a second-order transition in the corresponding classical model (see, e.g., Refs. [27, 74, 99, 139–141]).

The competition between non-equivalent NN bonds melts the semi-classical Néel order by formation of local singlets. By contrast to frustration, which yields competition in quantum as well as in classical systems, the local singlet formation is a pure quantum effect. Both mechanisms may of course be mixed as, for instance, in $CaV_4O_9$ or in $SrCu_2(BO_3)_2$ (see, e.g., Refs. [64, 68, 99]).

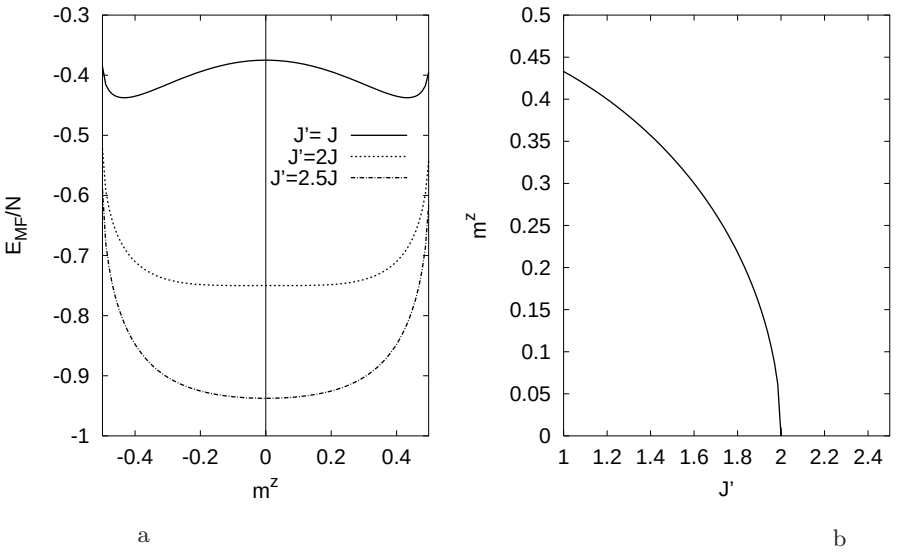


**Fig. 23.** Mean field results for the $J - J'-$HAFM on the CaVO lattice.
a: Energy versus order parameter b: Order parameter versus $J'$

Let us first discuss a mean-field like approach to describe the continuous quantum phase transition driven by local singlet formation. To that end we study the HAFM on the CaVO lattice having two non-equivalent NN bonds $J$ and $J'$, see Fig. 10. The uncorrelated mean-field state for Néel LRO is the two-sublattice Néel state $|\phi_{MF_1}\rangle = |\uparrow\rangle|\downarrow\rangle|\uparrow\rangle|\downarrow\rangle|\uparrow\rangle|\downarrow\rangle\ldots$ and for the dimerized singlet state it is the rotationally invariant product state of local singlets of the two spins belonging to a $J'$ bond $|\phi_{MF_2}\rangle = \prod_{\{i,j\}_{J'}} \{|\uparrow_i\rangle|\downarrow_j\rangle - |\downarrow_i\rangle|\uparrow_j\rangle\}/\sqrt{2}$ , where $i$ is a site in the sublattice $A$ and

$j$ a site in sublattice $B$. In order to describe the transition between both states, we consider an uncorrelated product state interpolating between $|\phi_{MF_1}\rangle$ and $|\phi_{MF_2}\rangle$ of the form [27,142]

$$|\Psi_{MF}(t)\rangle = \prod_{\{i,j\}_{J'}} \frac{1}{\sqrt{1+t^2}} \left\{ |\uparrow_i\rangle|\downarrow_j\rangle - t|\downarrow_i\rangle|\uparrow_j\rangle \right\}. \tag{15}$$

We have $|\Psi_{MF}(t=0)\rangle = |\phi_{MF_1}\rangle$ and $|\Psi_{MF}(t=1)\rangle = |\phi_{MF_2}\rangle$. The minimal value of the energy is given by

$$\frac{E_{MF}}{N} = \frac{\langle\Psi_{MF}|H|\Psi_{MF}\rangle}{N} = \begin{cases} -\frac{3J'}{8} - \frac{1}{16J}(2J-J')^2 & J' \leq 2J \\ -\frac{3J'}{8} & J' > 2J. \end{cases} \tag{16}$$

Furthermore, it is found that the sublattice magnetization $m^z$ has the following form

$$m^z = \langle\Psi_{MF}|S^z_{i\in A}|\Psi_{MF}\rangle = \begin{cases} \frac{1}{4J}\sqrt{(2J-J')(2J+J')} & J' \leq 2J \\ 0 & J' > 2J. \end{cases} \tag{17}$$

Note that $m^z$ vanishes at a critical point $J'_c = 2J$, and that the critical index is the mean-field index $1/2$ (see Fig. 23b). Using the relation between the variational parameter $t$ and the sublattice magnetization $m^z$ we find the relation $E_{MF}/N = -\frac{1}{8}J' - \frac{1}{4}J'\sqrt{1 - 4\,(m^z)^2} - J\,(m^z)^2$ showing the typical behavior of a second-order transition, see Fig. 23a. We can expand $E_{MF}$ up to the fourth order in $m^z$ near the critical point and find a Landau-type expression, given by $E_{MF}/N = -\frac{3}{8}J' + \frac{1}{2}(J'-2J)\,(m^z)^2 + \frac{1}{2}J'\,(m^z)^4$.

Although this mean-field like description gives some qualitative insight into the physics of the quantum phase transition for the CaVO lattice more elaborated investigations [48,64,66,70] show that the quantum phase transition to a rotationally invariant gapped dimerized GS phase takes place at $J'/J \approx 1.7$ and to the plaquette singlet GS phase at $J'/J \approx 0.9$. The critical exponents of quantum phase transitions driven by the competition of non-equivalent NN bonds in 2D quantum HAFMs are not the mean field exponents but those of the three-dimensional classical Heisenberg model [70,143].

Another interesting example for quantum phase transitions in spin systems appears in the Shastry-Sutherland model, i.e. the $J_1 - J_2$ HAFM on the SrCuBO lattice (T6). We will use in this section the Shastry-Sutherland representation (frustrated square lattice, see Fig. 16a, lower part). The classical GS of this model has two phases: The collinear Néel phase for $J_2 \leq J_1$ and a spiral phase for $J_2 > J_1$ (cf. Fig. 1 in Ref. [94]). The transition between the two classical phases is of second order.

For $J_2 \leq J_1$ the physics of the quantum model is similar to that of the classical model, i.e., we have semi-classical Néel order (see section 4.2). However, the quantum model exhibits new features for stronger frustration $J_2 > J_1$. Firstly, one finds that the collinear Néel phase in the quantum model can survive into the region where classically it is already unstable [94,99,102,104].

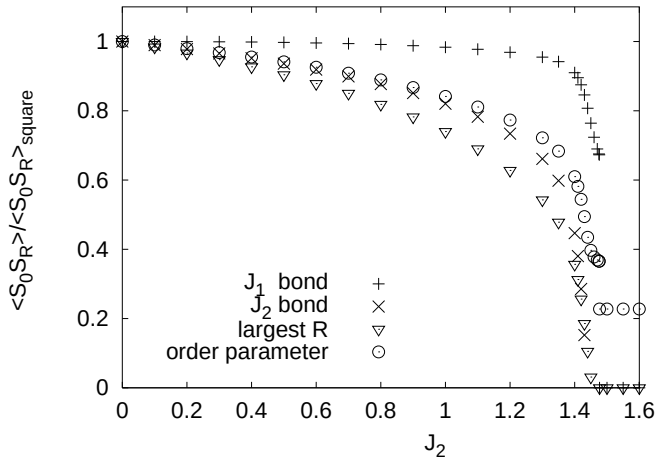


**Fig. 24.** Spin-spin correlation and square of sublattice magnetization (order parameter) scaled by their values for the square lattice ($J_2 = 0$) for the Shastry-Sutherland model ($N = 32$).

This effect is known as *order from disorder* [144, 145] and is widely observed in quantum spin systems (see, e.g. [27, 55, 110]).

Secondly, one knows already from Shastry and Sutherland [93] that for large enough $J_2$ the quantum GS is a rotationally invariant product state of local pair singlets $|\phi\rangle = \prod_{\{i,j\}_{J_2}} [|\uparrow_i\rangle|\downarrow\rangle_j - |\downarrow_i\rangle|\uparrow\rangle_j]/\sqrt{2}$ (so-called orthogonal dimer state), where $i$ and $j$ correspond to those sites which cover the $J_2$ bonds. This orthogonal dimer phase sets in at around $J_2^c \approx (1.45 \ldots 1.48) J_1$ [95–97, 99, 102, 104]. The nature of the transition to the dimer phase is still a matter of discussion, although there are arguments that the transition is probably of first order [94, 99]. In the region $1.2 J_1 \lesssim J_2 \lesssim 1.45 J_1$ the main challenging question is whether the system has an intermediate phase. Candidates are quantum spiral phases or more favorable a plaquette RVB like phase. Despite numerous investigations, a definite picture concerning the existence and nature of an intermediate phase has not yet emerged.

We illustrate such behavior discussed above by finite-lattice results ($N = 32$) for the spin-spin correlation along the NN $J_1$ bond, along the diagonal $J_2$ bond and for the largest separation $R = 4$ available in the finite $N = 32$ Shastry-Sutherland lattice as well as for the square of sublattice magnetization $\bar{m}^2$ (cf. eq. (6)) shown in Fig. 24. We have scaled the correlation functions and the sublattice magnetization by their corresponding values for the square lattice ($J_2 = 0$) for better comparison. The small changes in the correlation functions and the sublattice magnetization are in agreement with the survival of the collinear Néel ordering up to about $J_2 \sim 1.2 J_1$. Beyond $J_2 \sim 1.2 J_1$ the correlation functions change drastically up to $J_2 = 1.4785 J_1$, where for

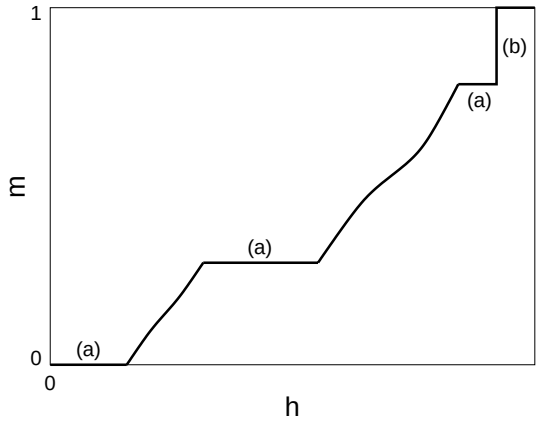


**Fig. 25.** Schematic magnetization curve illustrating some plateaux (a) and a jump below saturation (b).

$N = 32$ the rotationally invariant orthogonal dimer state becomes the GS. At this point the correlation functions and the sublattice magnetization jump to their values of the orthogonal dimer state. The behavior in the region $1.2J_1 \lesssim J_2 < 1.4785J_1$ preceding the transition to the orthogonal dimer state seems to be in accordance with the existence of an intermediate phase.

## 6 Magnetization process

In this final section we discuss the effect of a uniform external magnetic field on the models discussed so far. Once a small but finite magnetization is created by the external field, spins can no longer align completely antiparallel in the classical ground state even for a bipartite lattice. Since this is similar to the effect of geometric frustration, one can regard the magnetic field as introducing or enhancing frustration. One may therefore expect that a strong external field can induce further interesting quantum effects. In particular, we will discuss the quantum phenomena which are sketched in Fig. 25:

(a) Plateaux have a fixed magnetization $m$ in a region of the applied magnetic field $h$. Note that a plateau with magnetization $m = 0$ corresponds to a spin gap at zero magnetic field $h = 0$.
On a plateau, the magnetization $m$ typically assumes a (simple) rational fraction of its saturation value.
(b) Also some examples of jumps associated with a special degeneracy in the spectrum will be discussed in section 6.4.

Specifically we consider the Heisenberg antiferromagnet (1) in a uniform external magnetic field $h$

$$H = \sum_{<i,j>} J_{ij} \mathbf{S}_i \mathbf{S}_j - h \sum_i S_i^z \,. \tag{18}$$

In the following we will focus on the zero-temperature magnetization process of the Heisenberg antiferromagnet (18) on the 11 Archimedean and some related lattices. Some further aspects of two-dimensional $s = 1/2$ antiferromagnets in an external field have been summarized e.g. in [12,146].

In the present context it will sometimes be useful to allow for general length $s$ of the local spin. One can also introduce an $XXZ$ anisotropy as a prefactor $\Delta_I$ multiplying the $z$-$z$ interaction term in (1). Note that a magnetic field $h \neq 0$ already breaks the symmetry from $SU(2)$ down to $U(1)$ such that in contrast to the case $h = 0$, there is no reason for the Heisenberg point $\Delta_I = 1$ to be special. We will nevertheless concentrate mainly on $s = 1/2$ and $\Delta_I = 1$.

An important observable is the magnetization

$$m = \frac{1}{s\,N} \sum_i S_i^z \tag{19}$$

which we normalize to saturation value $m = 1$ (recall that $N$ is the total number of spins in the system). The magnetization (19) is a conserved quantity for the Hamiltonian (18): $[H, m] = 0$. One can therefore replace the operator (19) by its expectation value and by slight abuse of notation we will use the same symbol for both. The conservation of $m$ is also technically useful for computing the magnetization curve since one can relate energies with a field $E(h)$ to the energies $E(S^z, h = 0)$ for fixed total $S^z$ at $h = 0$

$$E(h) = E(S^z, h = 0) - h\,S^z \,. \tag{20}$$

This implies that the GS energies in the sectors $S^z$ and $S^z + 1$ cross at the magnetic field

$$h = E(S^z + 1, h = 0) - E(S^z, h = 0) \tag{21}$$

i.e. at this value of $h$ the magnetization increases by $1/s\,N$. The ground states with a given total spin $S$ typically carry the maximal possible $S^z$ and hence $S = S^z$ holds for them. In such a situation, $E(S^z, h = 0) = E(S)$ of the preceding sections and (21) implies that the $h(m)$ curve is obtained by (discrete) differentiation of the $E(S)$ curve at $h = 0$ with respect to $S \sim m$. In particular, if there is a regime with a quadratic dependence of $E$ on $S$ like in (10), the magnetization curve $m(h)$ becomes linear in this regime.

If $E(S)$ has a downward cusp, one obtains two different fields $h_1$ and $h_2$ when approaching the associated value of $m$ from below and above, respectively, and one finds a plateau in $m(h)$. In one dimension, the appearance of plateaux is governed by the following quantization condition on the magnetization $m$ [147] (see also [146] for a more detailed discussion)

$$sV\,(1 - m) \in \mathbb{Z} \,. \tag{22}$$

Here $V$ is the number of spins in a translational unit cell of the **ground state** (i.e. the lowest state for a given $m$) which can be larger than (namely an integer multiple of) the unit cell of the Hamiltonian if translational symmetry is spontaneously broken.

In two dimensions, there is no proof yet that the condition (22) is a necessary one. Nevertheless, the condition (22) should apply to those cases where plateau states are ordered (e.g. valence bond crystals) and it is therefore at least a useful guide also in two dimensions.

Fig. 26 shows results for magnetization curves of all 11 Archimedean lattices. With one exception, all these curves have been computed for finite lattices with $N = 36$ sites. Since for $s = 1/2$ only the discrete values $S^z = 0$, 1, ..., $N/2$ are allowed for a given $N$, one finds step-like curves on a finite lattice. The task is then to determine which parts of these curves will become smooth in the thermodynamic limit $N \to \infty$ or where anomalies like plateaux or jumps remain in this limit.

Clearly, the behavior in a magnetic field is even richer than the $h = 0$ properties and we will therefore not aim at a complete analysis. Before we proceed with a discussion of some selected aspects, we would like to add some remarks on two tilings that we will not discuss further. Firstly, on the trellis lattice (T5) the ground states in a magnetic field carry incommensurate momenta. They correspond in the $x$-direction to the twist angle $\alpha_2$ discussed in section 4.2 (although for $m < 1$ the GS momenta in a quantum system are in general different from the classical twist angle). Since irrational momenta are not realized for any finite lattice, one obtains additional finite-size effects. However, we have checked that these effects are sufficiently small for the $N = 36$ lattice which we have used to render the result in Fig. 26 qualitatively representative.

Secondly, the ground state on the CaVO lattice (T11) has a unit cell with 8 spins (see section 4.1). Since this does not fit on a lattice with $N = 36$ sites, one observes large finite-size artifacts in this case. In fact, the CaVO lattice is the only one among the 11 Archimedean lattices where no good magnetization curve can be obtained for $N = 36$. For completeness, we nevertheless show this result as the dotted curve in Fig. 26, but we also show a curve for $N = 32$ (full line) which should be considered as representative.

In the following three sections we discuss the tilings T2 (square), T1 (triangular) and T8 (kagomé) in more detail.

### 6.1 Square lattice

Let us start with a brief discussion of the magnetization process of the square lattice which is well understood and probably representative for the non-frustrated Archimedean tilings. Fig. 27 shows the magnetization curve of the $s = 1/2$ square-lattice Heisenberg antiferromagnet obtained by different approaches. Firstly, the thin full line shows the result obtained by exact diagonalization for a finite lattice with $N = 40$ sites [148] (see also [88,149,150] for

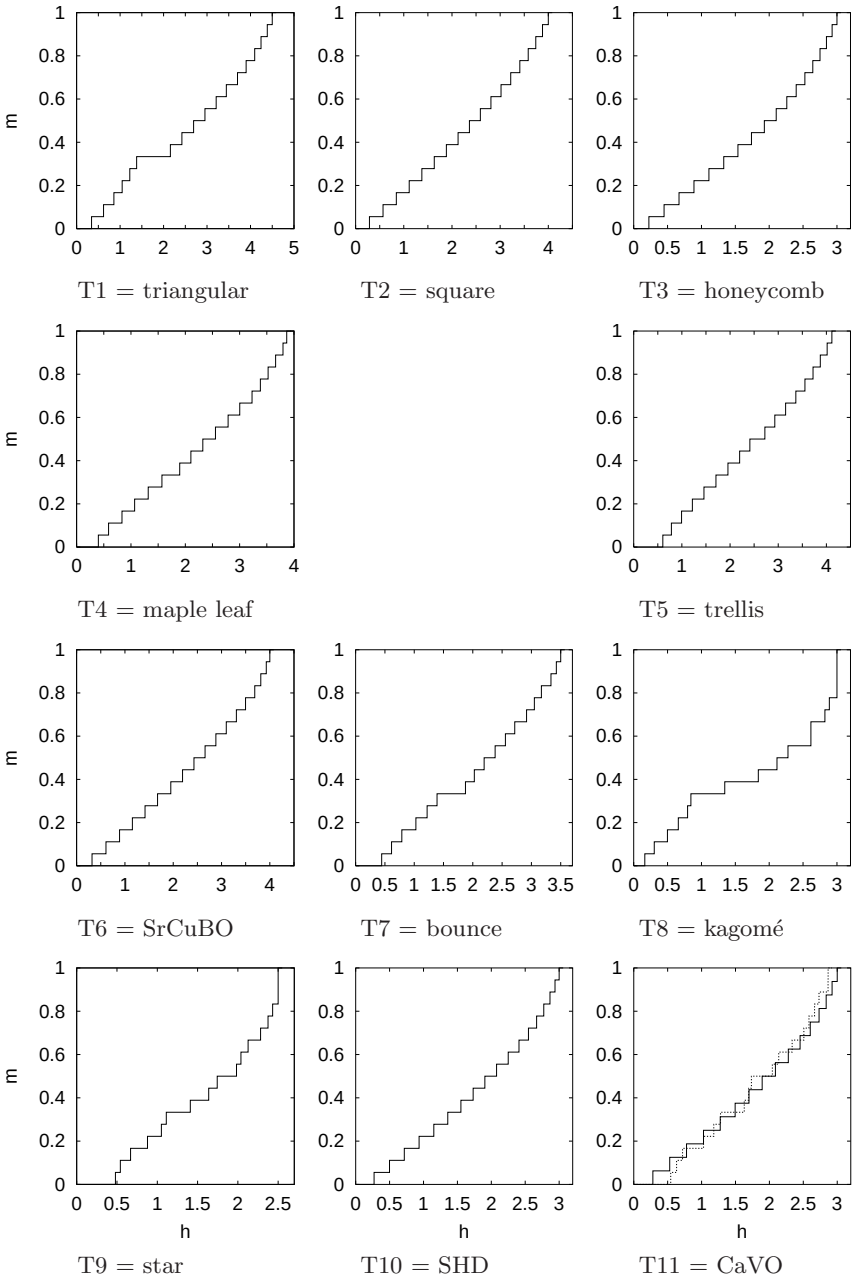


**Fig. 26.** Magnetization curves of the $s = 1/2$ Heisenberg antiferromagnet with $J = 1$ on all 11 Archimedean tilings. Results are for $N = 36$ sites except for the tiling T11 (CaVO) where the full curve shows a result for $N = 32$ which should be more representative than $N = 36$ (shown as the dashed curve). For further details compare the text.

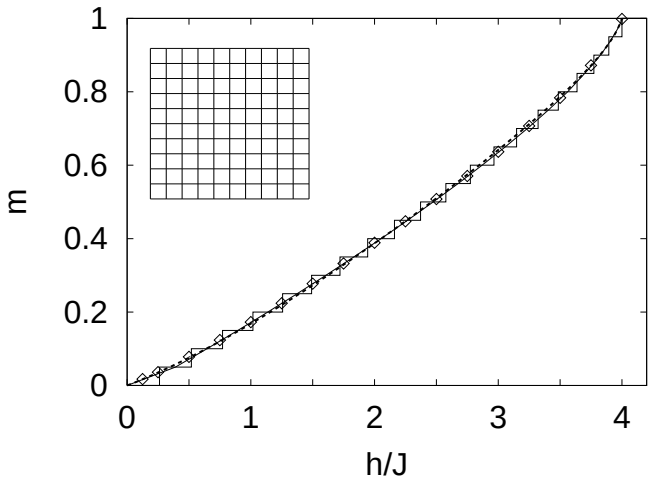


**Fig. 27.** Magnetization curve of the $s = 1/2$ Heisenberg antiferromagnet on the square lattice. The thin solid line is for $N = 40$ sites, the full bold line is an extrapolation to the thermodynamic limit. A second-order spin-wave result [151] (bold dashed line) and QMC results (diamonds) are also shown.

earlier exact diagonalization studies). The full bold line denotes an extrapolation of the exact diagonalization data to the thermodynamic limit which is obtained by connecting the midpoints of the finite-size steps at the largest available system size. One observes a smooth magnetization curve with no peculiar features (in particular no plateaux) for $|m| < 1$. Note that close to saturation the extrapolated curve includes data at large system sizes, which are not shown explicitly in Fig. 27 (the curve is based exclusively on finite lattices with at least $8 \times 8$ sites for $m \geq 0.84375$). The high-field part of the magnetization curve is therefore particularly well controlled by exact diagonalization.

The magnetization curve of a classical Heisenberg antiferromagnet would be just a straight line for all fields up to saturation. Hence, the curvature of the magnetization curve Fig. 27 is due to quantum effects. These quantum effects can also be studied by spin-wave theory; a second-order spin-wave result [151] is shown by the bold dashed line in Fig. 27.

Finally, the magnetization process of the square lattice can also be studied by quantum Monte Carlo (QMC) since this lattice is not frustrated, We have generated some values of $m(h)$ on a $64 \times 64$ lattice (typically at $T = J/50$ which we have lowered to $T = J/200$ upon approaching saturation) using the ALPS stochastic-series-expansion QMC application [152, 153]. These results are shown by the diamonds in Fig. 27 (statistical errors are much smaller than

the size of the symbols) and agree with available stochastic-series-expansion QMC results [154].

The quantitative differences of the results of all three approaches are small, i.e., each approach yields a good description of the $s = 1/2$ HAFM on the square lattice. As the spin-wave approach [151] is based on a Néel state, we may therefore conclude that Néel order prevails in the transverse components for $|m| < 1$ (see also [150] for a discussion from the point of view of exact diagonalization).

The same picture is probably also valid for the other bipartite non-frustrated tilings, namely T3 (honeycomb), T10 (SHD) and T11 (CaVO). All these lattices are believed to be Néel ordered at $h = 0$ (see section 4.4). Upon application of a magnetic field, the Néel vector first turns perpendicular to the field and then the sublattice magnetizations are smoothly tilted towards the field direction until full polarization is reached. At least the numerical results for the magnetization curves shown in Fig. 26 for the lattices T3 (honeycomb – see also [88] for further details and numerical data), T10 (SHD) and T11 (CaVO) are consistent with a smooth magnetization curve.

From an experimental point of view, one needs a sufficiently small exchange constant $J$ to render the saturation field acccessible in a laboratory. Successful synthesis and measurement of the magnetization process of suitable $s = 1/2$ square lattice antiferromagnets have been reported in [54].

### 6.2 Triangular lattice

The $s = 1/2$ $XXZ$ model on the triangular lattice is among the first models whose magnetization process was studied by exact diagonalization [155]. These early studies already found a plateau with $m = 1/3$, at least for Ising-like anisotropies $\Delta_I > 1$. Due to the restriction to at most 21 sites, it was first not completely clear whether the plateau persists in the isotropic regime $\Delta_I \approx 1$. The magnetization process of the Heisenberg antiferromagnet ($\Delta_I = 1$) was analyzed further using spin-wave theory [156]. This study provided evidence that the $m = 1/3$ plateau exists also at $\Delta_I = 1$ and estimates for its boundaries were obtained.

Fig. 28 shows the magnetization curves obtained by exact diagonalization for the $s = 1/2$ Heisenberg antiferromagnet on finite lattices with $N = 36$ and 39 sites (thin lines). There are small quantitative differences of the $N = 36$ curve with exact diagonalization results presented previously [37, 88, 146] whose origin is discussed in [148]. Both curves in Fig. 28 exhibit a clear plateau at $m = 1/3$ in an otherwise smooth magnetization curve. The spin-wave results for the magnetic fields at the lower $h_1 = 3\,(s - 0.084)\,J = 1.248\,J$ and the upper boundaries $h_2 = 3\,(s + 0.215)\,J = 2.145\,J$ of the $m = 1/3$ plateau [156] are smaller by about $0.13J$ (lower boundary) and $0.01J$ (upper boundary) than the exact diagonalization results presented here for $N = 39$ and $s = 1/2$.

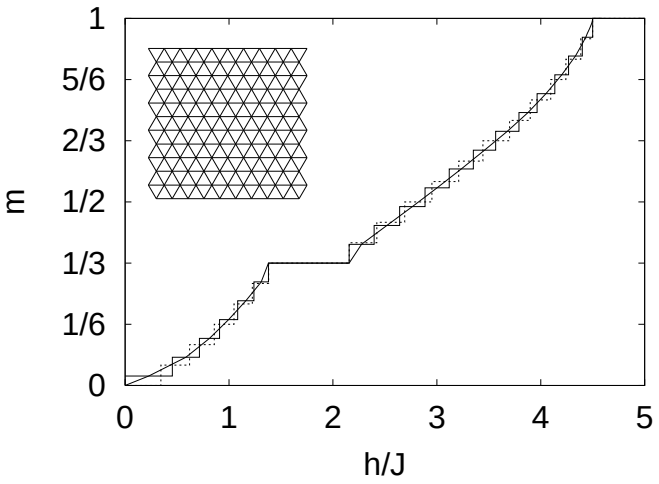


**Fig. 28.** Magnetization curve of the $s = 1/2$ Heisenberg antiferromagnet on the triangular lattice. The thin dashed and solid lines are for $N = 36$ and 39 sites, respectively. The bold line is an extrapolation to the thermodynamic limit.

The full bold line in Fig. 28 denotes an extrapolation of the exact diagonalization data to the thermodynamic limit which is obtained by connecting the midpoints of the finite-size steps at the largest available system size (except for the boundaries of the $m = 1/3$ plateau where corners were used). Close to saturation this includes again bigger system sizes than those explicitly shown in Fig. 28.

The state of the $m = 1/3$ plateau can be easily understood in the Ising limit $\Delta_I \gg 1$ [87, 88]. Quantum fluctuations are completely suppressed in the limit $\Delta_I \to \infty$ and the $m = 1/3$ state is a classical state where all spins on two of the three sublattices of the triangular lattice point up and all spins on the third sublattice point down. This state corresponds to an ordered collinear spin configuration. It is threefold degenerate and breaks the translational symmetry. One can then use perturbation theory in $1/\Delta_I$ to study the $m = 1/3$ plateau of the $XXZ$ model [88]. However, the current best estimate of the point $\Delta_{I,c}$ where the $m = 1/3$ plateau disappears is obtained from a numerical computation of the overlap of the Ising states and the $m = 1/3$ wave function of the full $XXZ$ model with $s = 1/2$: $\Delta_{I,c} = 0.76 \pm 0.03$ [148]. This means that the $m = 1/3$ plateau states of the Ising antiferromagnet and the Heisenberg antiferromagnet on the triangular lattice are qualitatively the same.

In the absence of a magnetic field, order persists in the Heisenberg antiferromagnet on the triangular lattice despite the geometric frustration (see section 4.2). We have now seen that the magnetic field enhances the frustra-

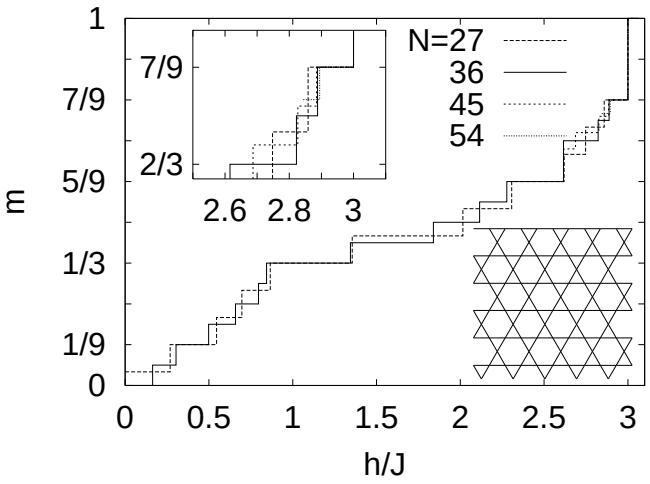


**Fig. 29.** Magnetization curves of the $s = 1/2$ Heisenberg antiferromagnet on the kagomé lattice with $N = 27$, 36 (complete), 45 and 54 (partial). The inset shows a magnified version of the region around $m = 7/9$.

tion sufficiently in the Heisenberg antiferromagnet on the triangular lattice to open a spin gap and thus a plateau at $m = 1/3$.

Among the other magnetization curves shown in Fig. 26, the one of the bounce lattice (T7) looks most similar to the one of the triangular lattice. Indeed, also the tiling T7 consists of triangles and one may expect that also here an up-up-down spin structure on each triangle gives rise to an $m = 1/3$ plateau. However, the covering of the complete lattice with up-up-down triangles is not unique for the bounce lattice, indicating at least some differences in the magnetization process of the triangular and bounce lattices.

### 6.3 Kagomé lattice

Among the Archimedean lattices, the kagomé (T8) and star (T9) lattices are characterized by the combination of strong frustration and low coordination number. As discussed in sections 4.3 and 4.4, we believe that they give rise to a quantum paramagnetic ground state at $h = 0$. The $N = 36$ magnetization curves in Fig. 26 indicate that these two lattices are presumably also those with the most complicated and rich magnetization processes among all 11 Archimedean lattices. Here we summarize the current understanding of the magnetization process of the $s = 1/2$ kagomé lattice and leave a detailed investigation of the star lattice to the future.

Fig. 29 shows complete magnetization curves for the kagomé lattice with $N = 27$ and 36 sites as well as the high-field part of $N = 45$ and 54 curves

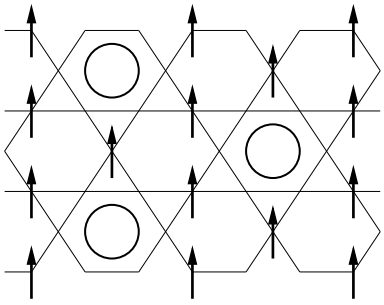

**Fig. 30.** Part of the kagomé lattice with a $\sqrt{3} \times \sqrt{3}$ superstructure indicated by the circles in certain hexagons. Arrows indicate spins which are aligned with the magnetic field.

[148, 157, 158]. Firstly, there should be a plateau at $m = 0$ associated to the small spin gap above the quantum paramagnetic ground state. However, this is difficult to recognize in Fig. 29.

A plateau at $m = 1/3$ may be better recognized in Fig. 29. In fact, the presence of this plateau at $m = 1/3$ in the $s = 1/2$ Heisenberg antiferromagnet on the kagomé lattice has been established previously by considering also system sizes different from those shown in Fig. 29 [157, 159]. The state of this plateau is, however, quite non-trivial. For the classical Heisenberg antiferromagnet at $m = 1/3$, thermal fluctuations select collinear states, but due to the huge degeneracy of these states, there appears to be no real order on the classical level at $m = 1/3$ [160] (see also [161]). For $s = 1/2$, it is useful to consider the $XXZ$ model. In the Ising limit $\Delta_I \to \infty$ one can then first establish [162] a relation to a quantum dimer model on the honeycomb lattice which was argued [163, 164] to give rise to a valence bond crystal ground state with a $\sqrt{3} \times \sqrt{3}$ order. Fig. 30 shows a qualitative picture of this state. In the present context the circles indicate resonances between the two different Néel states on the surrounding hexagon. The next step is to compute the overlap of the $m = 1/3$ wave function of the $XXZ$ model with that of the quantum dimer model as a function of $\Delta_I$ and one finds no evidence for a phase transition for $\Delta_I \geq 1$ [162]. This implies that also the $m = 1/3$ state of the $s = 1/2$ Heisenberg antiferromagnet on the kagomé lattice is an ordered state with features similar to the valence bond crystal. There are many low-lying non-magnetic excitations above the lowest $m = 1/3$ state which can be considered as a remnant of the classical degeneracy. However, the valence-bond-crystal-type order implies just three degenerate $m = 1/3$ ground states related by translational symmetry (see Fig. 30 for illustration) and a gap to *all* excitations above this three-fold degenerate ground state. Note that for the $s = 1/2$ Heisenberg antiferromagnet on the kagomé lattice this non-magnetic gap in the $m = 1/3$ sector turns out to be quite small (estimates are of the order of $J/25$ [162]).

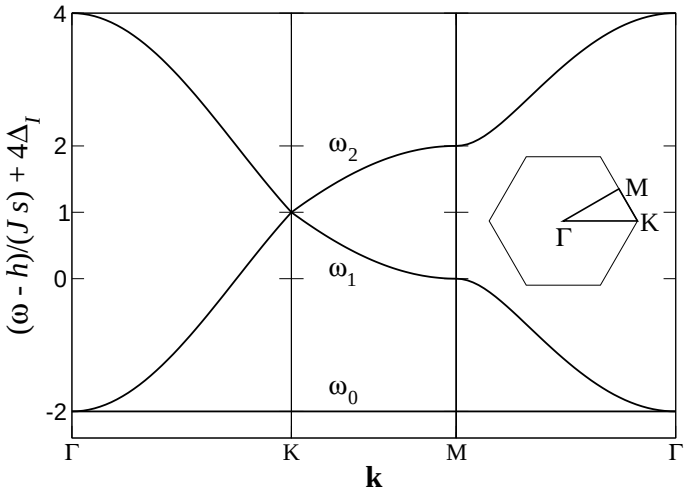


**Fig. 31.** The three branches $\omega_i(\mathbf{k})$ of one-magnon excitations above the ferromagnetic background for the kagomé lattice along the path in the Brillouin zone shown in the inset. Note that $\omega_0(\mathbf{k})$ is completely independent of $\mathbf{k}$.

There may be a further plateau at $m = 5/9$ in Fig. 29 although it is difficult to draw unambiguous conclusions from the available numerical data in this region of magnetization values.

Finally, one can see a pronounced jump of height $\delta m = 2/9$ just below saturation and a plateau at $m = 7/9$ in the magnetization curve of the $s = 1/2$ kagomé lattice. Both features will be discussed in more detail in the next section.

### 6.4 Independent magnons and macroscopic magnetization jumps

For the $s = 1/2$ Heisenberg model on a given two-dimensional lattice it is a very rare event that one can write down the ground state exactly. One such exceptional case is the dimerized ground state arising in the two-dimensional Shastry-Sutherland model [93] (see section 5). It is therefore remarkable that in the high-field region of some popular frustrated lattices such as the kagomé lattice one can construct a macroscopic number of exact ground states. We will discuss some aspects of the construction in more detail in this section, focusing in particular on the kagomé lattice. Note that similar constructions can be given for other lattices [158, 165] and finite clusters [166] (for other points of view we also refer to [158, 165]). We also wish to remark that the construction of exact eigenstates to be described below works for models where no non-trivial conservation laws are known. However, it is restricted to the transition to saturation, since, as will become clear in the following, it relies on the knowledge of a reference state (namely the ferromagnetically polarized

state $|\uparrow \ldots \uparrow\rangle$ which is a trivial eigenstate of the Hamiltonian) and an analytic determination of the one-magnon excitations above it.

Now let us be more specific and, as the first step, consider very high magnetic fields such that the ground state is the ferromagnetically polarized state. In highly frustrated spin models, the lowest branch $\omega_0(\mathbf{k})$ of the one-magnon excitations above the ferromagnetically polarized state often has some flat directions (i.e. does not depend on some of the components $k_i$) or is completely flat (i.e. independent of $\mathbf{k}$). In the latter case, one finds a special type of jump just below the saturation field as well as indications for a plateau below the jump [158, 165].

The explicit computation of the one-magnon spectrum above the ferromagnetically polarized state depends on the model. For example, the kagomé lattice has a unit cell containing three sites and the spectrum is obtained by diagonalization of a $3 \times 3$ matrix. For the spin-$s$ $XXZ$ model one then finds the three magnon branches $\omega_i(\mathbf{k})$ ($i = 0, 1, 2$) which are shown in Fig. 31. Remarkably, the lowest branch $\omega_0(\mathbf{k}) = h - (2 + 4\Delta_I)\, J\, s$ is completely flat, i.e. independent of $\mathbf{k}$. This property is a fingerprint of the strong frustration caused by the triangles in the kagomé lattice. In fact, the lowest magnon branch relative to the ferromagnetically polarized state is also completely flat for some other popular highly frustrated lattices including the pyrochlore lattice and its two-dimensional projection, namely the checkerboard lattice [158].

The one-magnon excitations can be localized in the real-space directions corresponding to a flat direction in $\mathbf{k}$-space by using an inverse Fourier transformation. If the dispersion is completely flat, one can construct a magnon excitation that is localized in a finite volume. For the kagomé lattice, these local magnon excitations are located on the hexagons marked by circles in Fig. 30. Apart from normalization, this state is given by

$$|1\rangle \sim \sum_x (-1)^x S_x^- \, |\uparrow \ldots \uparrow\rangle \tag{23}$$

where the sum runs over the 6 corners of the hexagon. Localization can be verified since each spin next to the hexagon is coupled to two spins in the hexagon such that contributions of flipped spins propagating onto the exterior site add with different signs and thus cancel. Therefore, a localized magnon is an exact eigenstate of the $XXZ$ Hamiltonian on the kagomé lattice.

Now one can create further localized magnon excitations. As long as the local magnons are sufficiently well separated in space, they do not interact and consequently the many-magnon state is still an exact eigenstate. The non-trivial step is to verify that these non-interacting localized magnon excitations are not only eigenstates but in fact ground states in their respective magnetization subspaces. This result is probably true for general $s$, general coupling geometries with $J_{i,j} \geq 0$ and $XXZ$ anisotropy $\Delta_I \geq 0$. In [158] the ground state property was verified numerically for some cases and it has been shown rigorously for certain subsets of the parameters, namely for $s = 1/2$,

$\Delta_I \geq 0$ and all coupling constants $J_{i,j}$ equal [166] or for general $s$ and $J_{i,j} \geq 0$, but isotropic interaction $\Delta_I = 1$ [167].

If the localization region is finite, a macroscopic fraction of the spins in the system can be flipped using local magnon excitations. Since the energies of the individual excitations add without interaction terms, one obtains a finite interval of the magnetization $m$ where the ground state energy $E(m)$ becomes a linear function. Due to the relation (21), this linear behavior leads to a finite jump in the magnetization curve $m(h)$ at the saturation field $h_{\rm sat}$.

Inspection of Fig. 30 shows that at most $N/9$ local magnons fit on a finite kagomé lattice. Therefore, a jump of height $\delta m = 1/(9\,s)$ is predicted for the kagomé lattice. For the $s = 1/2$ Heisenberg antiferromagnet on the kagomé lattice one indeed observes numerically a jump of height $\delta m = 2/9$ which is independent of the system size if boundary conditions are chosen appropriately (see Fig. 29). Note that the height of the jump is in general proportional to $1/s$ and vanishes in the classical limit $s \to \infty$. Therefore, the macroscopic jump caused by independent local magnons is a true macroscopic quantum effect.

The maximal number of local excitations is obtained for their closest possible packing. The circles in Fig. 30 indicate this state for the kagomé lattice. This clearly is an ordered (crystalline) state. According to general arguments [98, 168], one expects a gap above such a crystalline state and consequently a plateau in the magnetization curve at the foot of the jump. This conclusion is supported by the numerical magnetization curve of the $s = 1/2$ Heisenberg antiferromagnet on the kagomé lattice, Fig. 29, which exhibits a clear plateau at $m = 7/9$ with a width around $0.07J$ [169].

The excitation energy of a local magnon is exactly zero at the saturation field $h_{\rm sat}$. Hence, all independent magnon states are exactly degenerate at $h = h_{\rm sat}$. The number of these states grows exponentially with $N$. This can be seen by considering the subset of states where magnons sit only on the positions of the crystalline state. Since the number of such positions is proportional to $N$ and each position can be empty or occupied by a magnon, one finds an exponentially growing lower bound on the number of independent magnon states (this lower bound is $2^{N/9}$ for the kagomé lattice). In other words, the local magnon excitations give rise to a finite zero-temperature entropy at $h = h_{\rm sat}$ for a quantum spin system !

The star lattice (T9) is the other Archimedean tiling which supports local magnon excitations. In this case, the magnons are localized around dodecagons as shown by the circles in the inset of Fig. 32. The adjacent triangles again ensure localization via destructive interference of hopping processes out of a dodecagon. One can read off from the inset of Fig. 32 that a finite star lattice can in general accomodate at most $N/18$ local magnons. This implies a jump of height $\delta m = 1/(18\,s)$ below saturation with a plateau at $m = 1 - 1/(18\,s)$ corresponding to the crystalline pattern of local magnon excitations sketched in the inset of Fig. 32. The main panel of Fig. 32 shows that a jump of the expected height $\delta m = 1/9$ is indeed present in the magnetization curves of

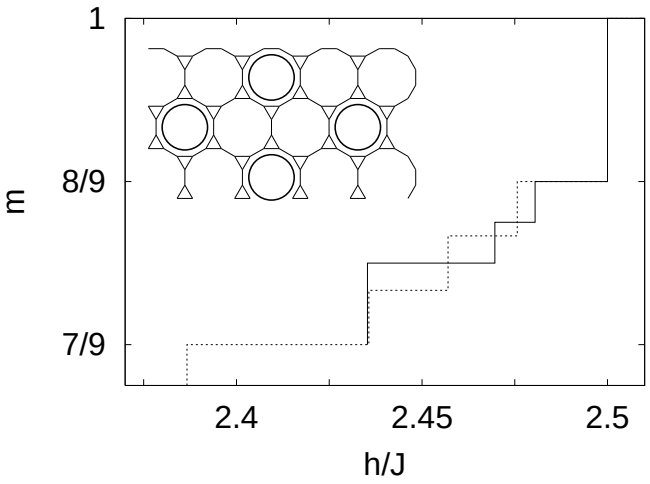


**Fig. 32.** High-field part of the magnetization curves of the $s = 1/2$ Heisenberg antiferromagnet on the star lattice (T9) with $N = 54$ (dashed line) and $N = 72$ sites (solid line). The inset indicates the closest packing of local magnon excitations.

the $s = 1/2$ model on lattices with $N = 54$ and 72. Note that the $N = 36$ lattice whose magnetization curve is shown in Fig. 26 is not generic, but an exception from the point of view of local magnons. Due to its small linear extent, it has more and shorter cycles wrapping around the boundary than present in the infinite system, namely of length eight while the dodecadons yield cycles with length twelve. This $N = 36$ lattice then supports not only two but three local magnons and therefore the jump is higher than in the generic situation. Note further that a plateau is expected below this jump, i.e. at $m = 8/9$ for $s = 1/2$. However, the $N = 54$ and 72 curves in Fig. 32 do not allow an unambiguous confirmation of the presence of such a plateau.

The checkerboard and a square-kagomé lattice are further two-dimensional lattices supporting local magnon excitations [158, 169]. On the checkerboard lattice, a magnon is localized around a square. This leads to a jump of size $\delta m = 1/(8\,s)$, as one can verify numerically for $s = 1/2$ [165].

We would like to mention in passing that there are instabilities towards lattice deformations. However, it can be argued that the most favorable instability is one which preserves the local magnon excitations as exact eigenstates and the associated degeneracy [169].

A related but different situation arises in two dimensions if the minima of the one-magnon excitations form a one-dimensional manifold. One example is the two-dimensional Shastry-Sutherland lattice [170] whose magnetization process will be discussed in the next section, another one is the frustrated square lattice mentioned in section 5 at $J_2 = J_1/2$ [171, 172]. In this case,

magnon excitations can be constructed [146, 158] that are localized in some directions, but not all. The frustrated square lattice can accommodate $L/2$ local magnon excitations [146,158] if the linear extent of the lattice is $L$, leading to a finite-size jump $\delta m = L/(2\,N\,s)$. A finite-size jump of height $\delta m = L/N$ is indeed observed in exact diagonalization studies of the $s = 1/2$ frustrated square lattice at $J_2 = J_1/2$ [146, 172]. However, due to the incomplete localization, the height of the jump vanishes in the thermodynamic limit, i.e. the transition to saturation remains continuous in such a case. Although the magnetization curve should be exceptionally steep just below saturation, the precise asymptotic form has been discussed controversially [150,158,172]. A recent diagrammatic analysis of the condensation problem into the one-magnon dispersion yields a square-root dependence with a logarithmic correction for the frustrated square lattice at $J_2 = J_1/2$ [173].

### 6.5 Shastry-Sutherland model versus $SrCu_2(BO_3)_2$

For the purpose of high-field magnetization experiments one does not only need materials which realize a given lattice structure, but in addition $J$ must be small in order to be able to achieve full or at least a macroscopic polarization of the sample in (pulsed) magnetization experiments. $SrCu_2(BO_3)_2$ is an $s = 1/2$ material whose lattice structure corresponds to the tiling T6 and where the exchange constants are sufficiently small to close the spin gap by an external magnetic field and study the material at finite magnetizations in a laboratory. The magnetization process of $SrCu_2(BO_3)_2$ has attracted considerable attention because plateaux are observed in the magnetization curve[11] at $m = 1/8$, $1/4$ and $1/3$ [5, 174–176] (see Fig. 33).

By contrast, the tiling T6 at $J = J_1 = J_2$ has a smooth magnetization curve (see Fig. 26), hence we need to consider the Shastry-Sutherland model with $J_1 \neq J_2$. The theoretical analysis of the magnetization process of the two-dimensional Shastry-Sutherland model [93] has been summarized in [105] – here we discuss only some selected aspects.

For $J_2 \to 0$, the Shastry-Sutherland model reduces to the square lattice antiferromagnet which is Néel ordered in the transverse components for all magnetic fields (see section 6.1). As discussed in section 5, this Néel phase extends beyond $J_2 = J_1$ for $m = 0$. For $m \to 1$, Néel order in the transverse components is stable for $J_2 \leq J_1$ [170]. We have performed a finite-size analysis of the widths of the $m = 1/8$, $1/4$, $1/3$ and $1/2$ steps and found no indications for plateaux in the thermodynamic limit for $J_2 = J_1$. These considerations indicate the absence of quantum phase transitions between $J_2 = 0$ and $J_2 = J_1$ for any value of the field $h$ such that Néel order persists for the tiling T6 with $J_2 = J_1$ at all magnetic fields.

[11] Magnetization experiments are controlled by a material-dependent and anisotropic $g$-factor. The $s = 1/2$ spins in $SrCu_2(BO_3)_2$ are localized on $Cu^{2+}$-ions, hence $g \approx 2$ – see e.g. [174] for more details.

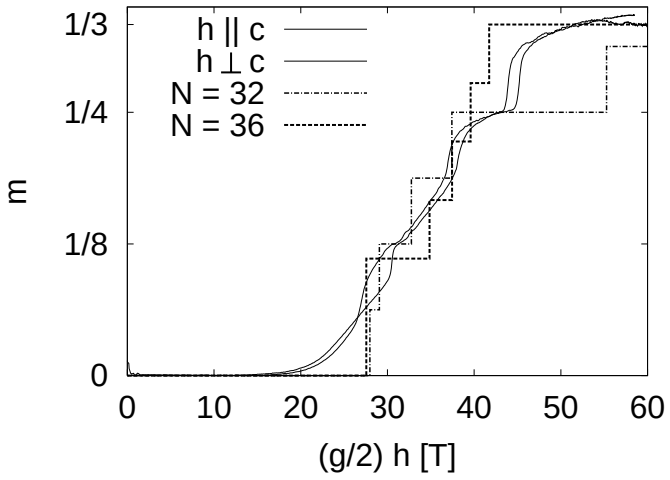


**Fig. 33.** Magnetization curves of a $SrCu_2(BO_3)_2$ single crystal scaled by $g = 2.28$ for $h \parallel c$ and $g = 2.05$ for $h \perp c$ [174]. Also shown are magnetization curves of the $s = 1/2$ Heisenberg antiferromagnet on $N = 32$ and 36 Shastry-Sutherland lattices for $J_2 = 57\mathrm{T}$, $J_1 = 0.6\, J_2$.

This is one indication that $SrCu_2(BO_3)_2$ should be described by $J_2 > J_1$ since several plateaux are observed in its magnetization curve Fig. 33, namely at $m = 0$, $1/8$, $1/4$ and $1/3$ [5, 174–176]. In this regime, one can perform perturbation expansions around the limit of decoupled dimers $J_1 = 0$ and indeed perturbation theory plays a central role in the theoretical approaches [98, 170, 177–179]. Plateaux at $m = 0$, $1/2$, $1/3$ and $1/4$ then arise in zeroth, first, second and fourth order perturbation theory in $J_1$, as has been clearly pointed out in [179].

For a direct comparison with the Shastry-Sutherland model, we adopt the estimates $J_1 \approx 0.6\, J_2$ and $J_2 \approx 70 - 75\mathrm{K}$ obtained by analyzing inelastic neutron scattering data [180–182] or the specific heat in a magnetic field [176]. The magnetization curves for the Shastry-Sutherland model shown in Fig. 33 were computed by choosing first $J_1 = 0.6\, J_2$ and then setting the overall scale to $J_2 = 57\mathrm{T}$ ($\approx 77\mathrm{K}$ with $g = 2$). The $m = 1/8$ and $1/4$ plateaux (present only for $N = 32$ in Fig. 33), the $m = 1/3$ plateau (present only for $N = 36$ in Fig. 33) and the $m = 0$ plateau agree roughly with the experimental results [174]. We have also performed computations for the value $J_1 = 0.68\, J_2$ proposed in [174] and have found less good agreement.

Only the region with $m \leq 1/3$ has so far been accessed with magnetization experiments on $SrCu_2(BO_3)_2$. Hence, the magnetization curves for the $N = 32$ and $N = 36$ Shastry-Sutherland lattices are also restricted to $m \leq 1/3$ in Fig. 33. Fig. 34 shows the corresponding complete magnetization curves for

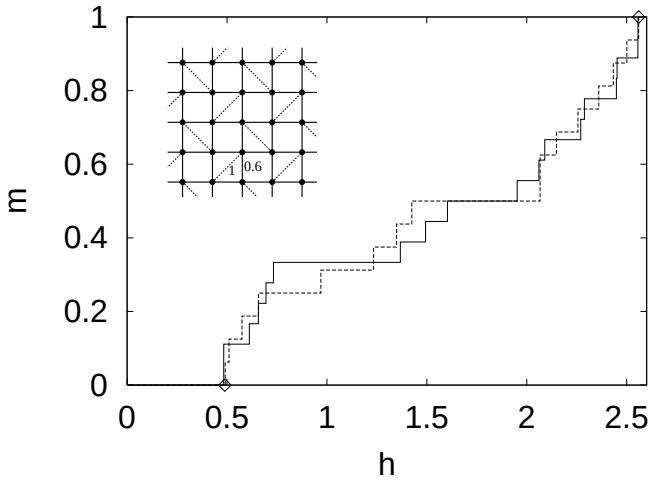


**Fig. 34.** Magnetization curve of the $s = 1/2$ Heisenberg antiferromagnet on the Shastry-Sutherland lattice for $J_2 = 1$, $J_1 = 0.6$. The dashed and solid lines are for $N = 32$ and $N = 36$ sites, respectively. The diamonds denote the exact value of the saturation field at $m = 1$ [170] and a series expansion result for the gap to $S = 1$ excitations at $m = 0$ [180], respectively.

$J_2 = 0.6\,J_1$. Note that we have chosen an $N = 32$ lattice which is compatible with the structure of the $m = 1/8$ plateau in $SrCu_2(BO_3)_2$ as determined by NMR [175]. For both finite lattices, the saturation field agrees well with the analytical result [170] shown by one of the diamonds in Fig. 34. Also the boundary of the $m = 0$ plateau is in good agreement with the spin gap (i.e. the gap to $S = 1$ excitations) computed by expansion around the dimer limit $J_1 = 0$ [180] (compare the second diamond in Fig. 34).

As on other lattices, it is more difficult to draw unambiguous conclusions from finite-size data for intermediate values of $m$. One complication which the Shastry-Sutherland model shares with the trellis lattice are incommensurate ground states arising from the spiral phase for $J_1 < J_2$ in the classical model (see section 5). A more general aspect is that given magnetizations are realized only for a limited number of sizes $N$. For example, lattices with $N = 32$ and 36 share only $m = 1/2$ in addition to $m = 0$ and 1. Even for $m = 1/2$ finite-size effects are still important in Fig. 34 although the presence of a plateau at $m = 1/2$ is well established in the Shastry-Sutherland model (see above and [105]). $m = 1/8$ is realized only for $N = 16$ apart from $N = 32$. From these two lattice sizes one may estimate a plateau width $\lesssim J_2/10$ for the Shastry-Sutherland model at $J_1 = 0.6\,J_2$, but the evidence in favor of a plateau at $m = 1/8$ is not very strong yet although its structure has already been analyzed in detail [175, 183].

### 6.6 Summary of plateaux & related topics

Let us summarize the findings of this section. Firstly, in section 6.1 we have discussed the square lattice which we believe to be representative for the non-frustrated bipartite tilings T2 (square), T6 (honeycomb), T10 (SHD) and T11 (CaVO). In these cases, Néel order probably persists in the transverse components for all magnetic fields up to saturation, leading to a smooth magnetization curve. The frustrated tilings T4 (maple leaf), T5 (trellis) and T6 (SrCuBO) may behave similarly. At least their $N = 36$ magnetization curves shown in Fig. 26 appear smooth and provide no evidence for any plateaux or jumps.

Also the triangular (T1) and bounce lattices (T7) are magnetically ordered at $h = 0$. However, in these two cases a plateau appears at $m = 1/3$ in the magnetization curves (see section 6.2). In both cases, the appearance of a plateau at $m = 1/3$ may be attributed to the fact that these lattices are built from triangles. Nevertheless, the structure of the $m = 1/3$ state on the bounce lattice may be different from the one of the triangular lattice which corresponds to a long-range ordered collinear up-up-down spin configuration.

The tilings T8 (kagomé) and T9 (star) have the most interesting magnetization curves. According to section 4.3, at $h = 0$ the kagomé lattice is expected to have a small spin gap whereas the star lattice has a large one. This gives rise to a narrow and pronounced plateau at $m = 0$, respectively. Comparison of results for the $s = 1/2$ Heisenberg antiferromagnet on the kagomé lattice with different sizes $N$ (see section 6.3) shows that the magnetization curve has a plateau at $m = 1/3$. Evidence has been provided recently [162] that the state of this $m = 1/3$ plateau on the kagomé lattice has a structure of the valence-bond-crystal type. The $N = 36$ magnetization curve of the star lattice shown in Fig. 26 indicates an $m = 1/3$ plateau, too. Since the lattice T9 also consists of triangles, it is plausible that this $m = 1/3$ plateau persists in the limit $N \to \infty$. Further plateaux are suspected on both lattices, including one at $m = 5/9$ on the kagomé lattice (see section 6.3) and a similar one at $m = 7/9$ on the star lattice (compare Fig. 32) even if the currently available numerical data do not allow definite conclusions.

Close to saturation, exact eigenstates can be constructed for the strongly frustrated tilings T8 (kagomé) and T9 (star) – see section 6.4. For general $s$ they give rise to a jump below saturation of height $\delta m = 1/(9\,s)$ (T8) and $\delta m = 1/(18\,s)$ (T9). Furthermore, a plateau is expected directly below this jump and such a plateau is indeed observed in the $s = 1/2$ Heisenberg antiferromagnet at $m = 7/9$ for the kagomé lattice (T8) and possibly at $m = 8/9$ for the star lattice (T9).

Although there are still open issues concerning the magnetization process on the 11 Archimedean lattices, it is already clear that even richer behavior is found if one allows different exchange constants on non-equivalent bonds or adds further couplings. Examples include the following:

- The two-dimensional Shastry-Sutherland model has been discussed in section 6.5. Here plateaux with $m = 0$, $1/4$, $1/3$ and $1/2$ have been found and a further one is expected at $m = 1/8$. In contrast, its ancestor, the tiling T6 has a smooth magnetization curve with no particular features (see Fig. 26).
- A similar situation arises in the CaVO lattice (T11) if one allows for two different exchange constants $J$ and $J'$ as shown in Fig. 10. It is clear at least in the limit $J' \to 0$ that plateaux can then arise for $m = 0$ and $1/2$ [77]. Further plateaux with $m = 1/4$, $3/4$ and $1/8$ arise in some parameter regions if one adds a second-neighbor interaction $J_2$ [77, 98].
- Not only the zero-field properties of the frustrated square lattice have attracted considerable attention (see section 5), but also its magnetization process has been studied intensively [146, 149, 150, 171–173, 184–187]. In this model, a collinear up-up-up-down state arises at half the saturation field [184, 185]. For $s = 1/2$, this state is found to be stabilized in the region $0.5 \lesssim J_2/J_1 \lesssim 0.66$ where it gives rise to a plateau with $m = 1/2$ [146, 172, 184, 185]. A further plateau at $m = 1/3$ is predicted by a Chern-Simons theory [187] and might also be observable in exact diagonalization studies although the latter do not allow definite conclusions about the presence or absence of an $m = 1/3$ plateau yet [146].
- Another variant of the square lattice is the checkerboard lattice, a planar projection of the pyrochlore lattice. The $s = 1/2$ checkerboard lattice has a pronounced spin gap at $h = 0$ [128, 129, 188], i.e. a plateau at $m = 0$. In the limit of decoupled four-spin units [129] another plateau arises at $m = 1/2$. Numerical data for $N = 32$, 40 [165] and 36 sites support the presence of an $m = 1/2$ plateau also in the checkerboard model where all coupling constants are equal. The construction of section 6.4 predicts another plateau at $m = 3/4$ in the $s = 1/2$ checkerboard model although here the numerical evidence [165] is less clear.
- One can also add multi-spin interactions. On the triangular lattice, inclusion of four-spin cyclic exchange terms in the $s = 1/2$ model gives rise to an additional plateau at $m = 1/2$ [12, 130, 189, 190]. This $m = 1/2$ plateau is already present in the classical model where one also finds an $m = 1/3$ plateau for a suitable choice of parameters [191]. The latter differs from the $m = 1/3$ plateau of section 6.2 which arises only in the quantum Heisenberg antiferromagnet on the triangular lattice and is absent in the classical limit.

All the aforementioned plateaux for $m \neq 0$ give rise to ordered ground states (at least in those cases where the state of the plateau is sufficiently well understood). The unit cell of the ground state then has a volume $V$ such that the magnetization $m$ satisfies the quantization condition (22). Hence, also in two dimensions this quantization condition seems to hold generically.

The transitions to saturation in 9 of the 11 Archimedean lattices appear to be continuous quantum phase transition (see Fig. 26). Generically, the dis-

persion of the one-magnon excitations above the ferromagnetically polarized state should be quadratic close to their minima. An analysis of the associated condensation problem then predicts the following universal asymptotic behavior of the magnetization curve close to the saturation field $h_{\rm sat}$ [192–194]

$$1 - m \sim \left(\frac{h_{\rm sat} - h}{J}\right) \ln\left(\frac{b\,J}{h_{\rm sat} - h}\right) \tag{24}$$

where $b$ is a non-universal constant. The logarithmic correction in (24) is characteristic for two dimensions and arises because of a logarithmic singularity in the density of states [192]. The functional form (24) has been verified by a first-order spin-wave approximation for the square lattice [151] and numerically for the $s = 1/2$ Heisenberg antiferromagnet on the square, honeycomb and triangular lattices [88, 146]. We note that a behavior of the form (24) is expected to be valid at generic continuous transitions at plateau boundaries in two dimensions [194] (at least in those cases where the fundamental excitations are magnons).

Deviations from (24) are expected if the one-magnon dispersion is not quadratic close to the minimum which in general requires fine-tuning of parameters. Nevertheless, completely flat bands arise in two Archimedean lattices, namley the kagomé and star lattices (T8 and T9). In these cases, we find a macroscopic jump in the magnetization curve just below saturation as we have discussed in section 6.4

**Acknowledgments**

The authors are indebted to R. Ferchmin and P. Tomczak for bringing our attention to the 11 Archimedean tilings. We thank A. Harrison to inform us on Ref. [24]. We would like to thank H.-U. Everts and R. Schumann for critical reading the manuscript and P. Tomczak and H.-U. Everts for useful discussions. Thanks go to H. Kageyama for sending us the magnetization data of [174] which we reproduced in Fig. 33. The more complicated computations presented in this article have been performed on the compute-servers `wildfire`, `marvel` and `cfgauss` at the computing centers of Magdeburg University and the TU Braunschweig, respectively. We are particularly grateful to J. Schüle of the Rechenzentrum at the TU Braunschweig for technical support. This work was partly supported by the DFG (project Ri615/10-1).

## References

1. T. Barnes: Int. J. Mod. Phys. C **2**, 659 (1991)
2. E. Manousakis: Rev. Mod. Phys. **63**, 1 (1991)
3. E. Dagotto: Rev. Mod. Phys. **66**, 763 (1994)
4. S. Taniguchi, T. Nishikawa, Y. Yasui, Y. Kobayashi, M. Sato, T. Nishioka, M. Kontani, K. Sano: J. Phys. Soc. Jpn. **64**, 2758 (1995)

5. H. Kageyama, K. Yoshimura, R. Stern, N.V. Mushnikov, K. Onizuka, M. Kato, K. Kosuge, C.P. Slichter, T. Goto, Y. Ueda: Phys. Rev. Lett. **82**, 3168 (1999)
6. H. Tanaka, T. Ono, H. Aruga Katori, H. Mitamura, F. Ishikawa, T. Goto: Progr. Theor. Phys. Suppl. **145**, 101 (2002)
7. N.D. Mermin, H. Wagner: Phys. Rev. Lett. **17**, 1133 (1966)
8. P.W. Anderson: Mater. Res. Bull. **8**, 153 (1973)
9. P. Fazekas, P.W. Anderson: Philos. Mag. **30**, 423 (1974)
10. S. Sachdev, *Quantum Phase Transitions* (Cambridge University Press, Cambridge 1999)
11. C. Lhuillier, P. Sindzingre, J.-B. Fouet: Can. J. Phys. **7**9, 1525 (2001)
12. C. Lhuillier, G. Misguich: Frustrated quantum magnets
    In: *High magnetic fields*, ed by C. Berthier, L.P. Lévy, G. Martinez, Lecture Notes in Physics 595 (Springer, Berlin, 2001) pp 161-190
13. P. Sindzingre, C. Lhuillier, J.-B. Fouet: Quantum phases in two-dimensional frustrated spin-1/2-antiferromgnets
    In: *Series on Advances in Quantum Many-Body Theory*, vol. 6 ed by R.F. Bishop, T. Brandes, K.A. Gernoth, N.R. Walet, Y. Xian (World Scientific, Singapore 2002) pp 90-98
14. C. Lhuillier, P. Sindzingre: Spin-1/2 antiferromagnets in 2 dimensions
    In: *Quantum Properties of Low-Dimensional Antiferromagnets*, ed by Y. Ajiro, J.-P. Boucher (Kyushu University Press 2002) pp 111-117 (also: `cond-mat/0212351`)
15. G. Misguich, C. Lhuillier: Two-dimensional quantum antiferromagnets
    In: *Frustrated Spin Systems*, ed by H.T. Diep (World Scientific 2005) pp 229-306 (also: `cond-mat/0310405`)
16. B. Canals, C. Lacroix: Phys. Rev. Lett. **80**, 2933 (1998)
17. Spinpack homepage: `http://www-e.uni-magdeburg.de/jschulen/spin/`
18. J. Schulenburg: Einfluß der Gitterstruktur auf den Grundzustand von $s = 1/2$-Quantenspinsystemen, PhD thesis, University of Magdeburg (2002)
    [`http://www-e.uni-magdeburg.de/jschulen/diss/diss.pdf`]
19. S. Chakravartry, B.I. Halperin, D.R. Nelson: Phys. Rev. B **39**, 2344 (1989)
20. A.V. Chubukov, S. Sachdev, T. Senthil: Nuclear Phys. B **426**, 601 (1994)
21. J. Richter, S. Krüger, D. Farnell, R. Bishop: Quantum phase transitions in spin systems
    In: *Series on Advances in Quantum Many-Body Theory*, vol. 5 ed by R.F. Bishop, K.A. Gernoth, N.R. Walet (World Scientific, Singapore 2001) pp 239-246
22. F. Mila: Quantum Frustrated Magnets: From Theory to Experiment
    In: *Series on Advances in Quantum Many-Body Theory*, vol. 6 ed by R.F. Bishop, T. Brandes, K.A. Gernoth, N.R. Walet, Y. Xian (World Scientific, Singapore 2002) pp 80-89
23. B. Grünbaum, G.C. Shephard: *Tilings and Patterns*, W.H. Freeman and Company, New York (1987)
24. P.N. Suding, R.M. Ziff: Phys. Rev. E **60**, 275 (1999)
25. S. Kobe, K. Handrich: Phys. Stat. Sol. b **73**, K65 (1976); J. Richter, S. Kobe: J. Phys. C **15**, 2193 (1982); S. Kobe, T. Klotz: Phys. Rev. E **52**, 5660 (1995)
26. R.R.P. Singh, M.P. Gelfand, D.A. Huse: Phys. Rev. Lett. **61**, 2484 (1988)
27. S.E. Krüger, J. Richter, J. Schulenburg, D.J.J. Farnell, R.F. Bishop: Phys. Rev. B **61**, 14607 (2000); S.E. Krüger, J. Richter: Phys. Rev. B **64**, 024433 (2001)

28. W. Marshall: Proc. Roy. Soc. A **232**, 48 (1955)
29. E. Lieb, D. Mattis: J. Math. Phys. **3**, 749 (1962)
30. J. Richter, N.B. Ivanov, K. Retzlaff, A. Voigt: J. Magn. Magn. Mat. **140-144**, 1611 (1995)
31. B. Bernu, C. Lhuillier, L. Pierre: Phys. Rev. Lett. **69**, 2590 (1992)
32. D.D. Betts, J. Schulenburg, G.E. Stewart, J. Richter, J.S. Flynn: J. Phys. A: Math. Gen. **31**, 7685 (1998)
33. D.D. Betts, H.Q. Lin, J.S. Flynn: Can. J. Phys. **77**, 353 (1999)
34. P.W. Anderson: Phys. Rev. **86**, 694 (1952)
35. H. Neuberger, T. Ziman: Phys. Rev. B **39**, 2608 (1989)
36. B. Bernu, P. Lecheminant, C. Lhuillier, L. Pierre: Physica Scripta T **49**, 192 (1993)
37. B. Bernu, P. Lecheminant, C. Lhuillier, L. Pierre: Phys. Rev. B **50**, 10048 (1994)
38. P. Lecheminant, B. Bernu, C. Lhuillier, L. Pierre, P. Sindzingre: Phys. Rev. B **56**, 2521 (1997)
39. Ch. Waldtmann, H.-U. Everts, B. Bernu, C. Lhuillier, P. Sindzingre, P. Lecheminant, L. Pierre: Eur. Phys. J. B **2**, 501 (1998)
40. J. Richter, N.B. Ivanov, K. Retzlaff: acta physica slovaca **44**, 365 (1994)
41. A. Voigt, J. Richter, P. Tomczak: Physica A **299**, 461 (2001)
42. J.B. Fouet, P. Sindzingre, C. Lhuillier: Eur. Phys. J. B **20**, 241 (2001)
43. P. Tomczak, J. Schulenburg, J. Richter, A.R. Ferchmin: J. Phys.: Condens. Matter **13**, 3851 (2001)
44. P. Hasenfratz, H. Leutwyler: Nuclear Phys. B **343**, 241 (1990)
45. P. Hasenfratz, F. Niedermayer: Z. Phys. B **92**, 91 (1993)
46. J. Oitmaa, C.J. Hamer, Zheng Weihong: Phys. Rev. B **50**, 3877 (1994)
47. A.W. Sandvik: Phys. Rev. B **56**, 11678 (1997)
48. M. Troyer, H. Kontani, K. Ueda: Phys. Rev. Lett. **76**, 3822 (1996)
49. E.J. Neves, J.F. Perez: Phys. Lett. **114A**, 331 (1986)
50. I. Affleck, T. Kennedy, E.H. Lieb, H. Tasaki: Commun. Math. Phys. **115**, 477 (1988)
51. K. Kubo, T. Kishi: Phys. Rev. Lett. **61**, 2585 (1988)
52. H.-A. Wischmann, E. Müller-Hartmann: J. Phys. I (Paris) **1**, 647 (1991)
53. M. Greven, R.J. Birgeneau, Y. Endoh, M.A. Kastner, B. Keimer, M. Matsuda, G. Shirane, T.R. Thurston: Phys. Rev. Lett. **72**, 1096 (1994)
54. F.M. Woodward, A.S. Albrecht, C.M. Wynn, C.P. Landee, M.M. Turnbull: Phys. Rev. B **65**, 144412 (2002)
55. H.J. Schulz, T.A.L. Ziman: Europhys. Lett. **18**, 355 (1992); H.J. Schulz, T.A.L. Ziman, D. Poilblanc: J. Phys. I France **6**, 675 (1996)
56. Zheng Weihong, C.J. Hamer: Phys. Rev. B **47**, 7961 (1993)
57. R.F. Bishop, D.J.J. Farnell, S.E. Krüger, J.B. Parkinson, J. Richter: J. Phys. Condens. Matter **12**, 6887 (2000)
58. Zheng Weihong, J. Oitmaa, C.J. Hamer: Phys. Rev. B **43**, 8321 (1991)
59. J.D. Reger, J.A. Riera, A.P. Young: J. Phys.: Condens. Matter **1**, 1855 (1989)
60. Zheng Weihong, J. Oitmaa, C.J. Hamer: Phys. Rev. B **44**, 11869 (1991)
61. J. Oitmaa, C.J. Hamer, Zheng Weihong: Phys. Rev. B **45**, 9834 (1992)
62. A. Mattsson, P. Fröjdh, T. Einarsson: Phys. Rev. B **49**, 3997 (1994)
63. N. Katoh, M. Imada: J. Phys. Soc. Jpn. **64**, 4105 (1995)
64. K. Ueda, H. Kontani, M. Sigrist, P.A. Lee: Phys. Rev. Lett. **76**, 1932 (1996)

65. O.A. Starykh, M.E. Zhitomirsky, D.I. Khomskii, R.R.P. Singh, K. Ueda: Phys. Rev. Lett. **77**, 2558 (1996)
66. M.P. Gelfand, Zheng Weihong, R.R.P. Singh, J. Oitmaa, C.J. Hamer: Phys. Rev. Lett. **77**, 2794 (1996)
67. M. Albrecht, F. Mila: Phys. Rev. B **53**, R2945 (1996)
68. M. Albrecht, F. Mila, D. Poilblanc: Phys. Rev. B **54**, 15856 (1996)
69. Zheng Weihong, M.P. Gelfand, R.R.P. Singh, J. Oitmaa, C.J. Hamer: Phys. Rev. B **55**, 11377 (1997)
70. M. Troyer, M. Imada, K. Ueda: J. Phys. Soc. Jpn. **66**, 2957 (1997)
71. I. Bose, A. Ghosh: Phys. Rev. B **56**, 3149 (1997)
72. L.O. Manuel, M.I. Micheletti, A.E. Trumper, H.A. Ceccatto: Phys. Rev. B **58**, 8490 (1998)
73. Zheng Weihong, J. Oitmaa, C.J. Hamer: Phys. Rev. B **58**, 14147 (1998)
74. J. Richter, N.B. Ivanov, J. Schulenburg: J. Phys.: Condens. Matter **10**, 3635 (1998)
75. M.A. Korotin, I.S. Elfimov, V.I. Anisimov, M. Troyer, D.I. Khomskii: Phys. Rev. Lett. **83**, 1387 (1999)
76. C.S. Hellberg, W.E. Pickett, L.L. Boyer, H.T. Stokes, M.J. Mehl: J. Phys. Soc. Jpn. **68**, 3489 (1999)
77. Y. Fukumoto, A. Oguchi: J. Phys. Soc. Jpn. **68**, 3655 (1999)
78. P. Tomczak, J. Richter: Phys. Rev. B **59**, 107 (1999)
79. D.A. Huse, V. Elser: Phys. Rev. Lett. **60**, 2531 (1988)
80. Th. Jolicoeur, J.C. Le Guillou: Phys. Rev. B **40**, 2727R (1989)
81. S.J. Miyake: J. Phys. Soc. Jpn. **61**, 983 (1992)
82. R. Deutscher, H.U. Everts: Z. Phys. B **93**, 77 (1993)
83. A.E. Trumper: Phys. Rev. B **60**, 2987 (1999)
84. L. Capriotti, A.E. Trumper, S. Sorella: Phys. Rev. Lett. **82**, 3899 (1999)
85. L. Capriotti: Int. J. of Mod. Phys. B **15**, 1799 (2001)
86. D.J.J. Farnell, R.F. Bishop, K.A. Gernoth: Phys. Rev. B **63**, 220402(R) (2001)
87. S. Miyashita: J. Phys. Soc. Jpn. **55**, 3605 (1986)
88. A. Honecker: J. Phys.: Condens. Matter **11**, 4697 (1999)
89. D.D. Betts: Proc. N.S. Inst. Sci. **40**, 95 (1995)
90. D. Schmalfuß, P. Tomczak, J. Schulenburg, J. Richter: Phys. Rev. B **65**, 224405 (2002)
91. B. Normand, K. Penc, M. Albrecht, F. Mila: Phys. Rev. B **56**, R5736 (1997)
92. S. Miyahara, M. Troyer, D.C. Johnston, K. Ueda: J. Phys. Soc. Jpn. **67**, 3918 (1998)
93. B.S. Shastry, B. Sutherland: Physica B **108**, 1069 (1981)
94. M. Albrecht, F. Mila: Europhys. Lett. **34**, 145 (1996)
95. S. Miyahara, K. Ueda: Phys. Rev. Lett. **82**, 3701 (1999)
96. Zheng Weihong, C.J. Hamer, J. Oitmaa: Phys. Rev. B **60**, 6608 (1999)
97. E. Müller-Hartmann, R.R.P. Singh, C. Knetter, G.S. Uhrig: Phys. Rev. Lett. **84**, 1808 (2000)
98. T. Momoi, K. Totsuka: Phys. Rev. B **61**, 3231 (2000)
99. A. Koga, N. Kawakami: Phys. Rev. Lett. **84**, 4461 (2000)
100. G. Misguich, Th. Jolicoeur, S.M. Girvin: Phys. Rev. Lett. **87**, 097203 (2001)
101. C.H. Chung, J.B. Marston, S. Sachdev: Phys. Rev. B **64**, 134407 (2001)
102. Weihong Zheng, J. Oitmaa, C.J. Hamer: Phys. Rev. B **65**, 014408 (2001)
103. D. Carpentier, L. Balents: Phys. Rev. B **65**, 024427 (2002)

104. A. Läuchli, S. Wessel, M. Sigrist: Phys. Rev. B **66**, 014401 (2002)
105. S. Miyahara, K. Ueda: J. Phys.: Condens. Matter **15**, R327 (2003)
106. J. Richter, D.J.J. Farnell: unpublished
107. M. Mekata: Phys. Today **56**, 12 (2003)
108. C. Zeng, V. Elser: Phys. Rev. B **42**, 8436 (1990)
109. A.B. Harris, C. Kallin, A.J. Berlinsky: Phys. Rev. B **45**, 2899 (1992)
110. A. Chubukov: Phys. Rev. Lett. **69**, 832 (1992)
111. P.W. Leung, V. Elser: Phys. Rev. B **47**, 5459 (1993)
112. K. Yang, L.K. Warman, S.M. Girvin: Phys. Rev. Lett. **70**, 2641 (1993)
113. F. Mila: Phys. Rev. Lett. **81**, 2356 (1998)
114. Ch. Waldtmann, H. Kreutzmann, U. Schollwöck, K. Maisinger, H.-U. Everts: Phys. Rev. B **62**, 9472 (2000)
115. Weiqiang Yu, Shiping Feng: Eur. Phys. J. B **13**, 265 (2000)
116. M. Mambrini, F. Mila: Eur. Phys. J. B **17**, 651 (2000)
117. R. Shankar, D. Shubashree: Phys. Rev. B **61**, 12126 (2000)
118. P. Sindzingre, G. Misguich, C. Lhuillier, B. Bernu, L. Pierre, Ch. Waldtmann, H.-U. Everts: Phys. Rev. Lett. **84**, 2953 (2000)
119. A.V. Syromyatnikov, S.V. Maleyev: Phys. Rev. B **66**, 132408 (2002)
120. B.H. Bernhard, B. Canals, C. Lacroix: Phys. Rev. B **66**, 104424 (2002)
121. A.P. Ramirez: Annu. Rev. Mater. Sci. **24**, 453 (1994)
122. A.P. Ramirez, B. Hessen, M. Winkelmann: Phys. Rev. Lett. **84**, 2957 (2000)
123. Z. Hiroi, M. Hanawa, N. Kobayashi, M. Nohara, H. Takagi, Y. Kato, M. Takigawa: J. Phys. Soc. Jpn. **70**, 3377 (2001)
124. C. Gros, P. Lemmens, K.-Y. Choi, G. Güntherodt, M. Baenitz, H.H. Otto: Europhys. Lett. **60**, 276 (2002)
125. J.T. Chalker, P.C.W. Holdsworth, E.F. Shender: Phys. Rev. Lett. **68**, 855 (1992)
126. D.A. Huse, A.D. Rutenberg: Phys. Rev. B **45**, 7536 (1992)
127. J.N. Reimers, A.J. Berlinsky: Phys. Rev. B **48**, 9539 (1993)
128. J.-B. Fouet, M. Mambrini, P. Sindzingre, C. Lhuillier: Phys. Rev. B **67**, 054411 (2003)
129. W. Brenig, A. Honecker: Phys. Rev. B **65**, 140407(R) (2002)
130. W. LiMing, G. Misguich, P. Sindzingre, C. Lhuillier: Phys. Rev. B **62**, 6372 (2000)
131. V.N. Kotov, J. Oitmaa, O. Sushkov, Z. Weihong: Phil. Mag. B **80**, 1483 (2000)
132. P. Chandra, B. Doucot: Phys. Rev. B **38**, 9335 (1988)
133. J. Richter: Phys. Rev. B **47**, 5794 (1993)
134. A.V. Dotsenko, O.P. Sushkov: Phys. Rev. B **50**, 13821 (1994)
135. J. Oitmaa, Zheng Weihong: Phys. Rev. B **54**, 3022 (1996)
136. R.F. Bishop, D.J.J. Farnell, J.B. Parkinson: Phys. Rev. B **58**, 6394 (1998)
137. L. Capriotti, S. Sorella: Phys. Rev. Lett. **84**, 3173 (2000)
138. O.P. Sushkov, J. Oitmaa, Zheng Weihong: Phys. Rev. B **63**, 104420 (2001)
139. Y. Xian: Phys. Rev. B **52**, 12485 (1995)
140. A. Koga, K. Okunishi, N. Kawakami: Phys. Rev. B **62**, 5558 (2000)
141. J. Schulenburg, J. Richter: Phys. Rev. B **66**, 134419 (2002)
142. C. Gros, W. Wenzel, J. Richter: Europhys. Lett. **32**, 747 (1995)
143. P. Tomczak, J. Richter: J. Phys. A: Math. Gen. **34**, L461 (2001)
144. J. Villain, R. Bidaux, J.P. Carton, R. Conte: J. Phys. **41**, 1263 (1980)
145. E.F. Shender: Zh. Eksp. Teor. Fiz. **83**, 326 (1982) (Sov. Phys. JETP **56**, 178 (1982))

146. A. Honecker: The magnetization process of antiferromagnetic quantum spin systems and macroscopic quantum effects, habilitation thesis (2003) [http://perso.u-cergy.fr/~ahonecker/papers/bs/habil.pdf]
147. M. Oshikawa, M. Yamanaka, I. Affleck: Phys. Rev. Lett. **78**, 1984 (1997)
148. A. Honecker, J. Schulenburg, J. Richter: J. Phys.: Condens. Matter **16**, S749 (2004)
149. Yu.E. Lozovik, O.I. Notych: Solid State Communications **85**, 873 (1993)
150. M.S. Yang, K.-H. Mütter: Z. Phys. B **104**, 117 (1997)
151. M.E. Zhitomirsky, T. Nikuni: Phys. Rev. B **57**, 5013 (1998)
152. F. Alet, S. Wessel, M. Troyer: Phys. Rev. E **71**, 036706 (2005)
153. ALPS homepage: http://alps.comp-phys.org/
154. A.W. Sandvik: Phys. Rev. B **59**, R14157 (1999)
155. H. Nishimori, S. Miyashita: J. Phys. Soc. Jpn. **55**, 4448 (1986)
156. A.V. Chubukov, D.I. Golosov: J. Phys.: Condens. Matter **3**, 69 (1991)
157. K. Hida: J. Phys. Soc. Jpn. **70**, 3673 (2001)
158. J. Schulenburg, A. Honecker, J. Schnack, J. Richter, H.-J. Schmidt: Phys. Rev. Lett. **88**, 167207 (2002)
159. D.C. Cabra, M.D. Grynberg, P.C.W. Holdsworth, P. Pujol: Phys. Rev. B **65**, 094418 (2002)
160. M.E. Zhitomirsky: Phys. Rev. Lett. **88**, 057204 (2002)
161. E.F. Shender, P.C.W. Holdsworth: Order by disorder and topology in frustrated magnetic systems
In: *Fluctuations and Order* ed by M. Millonas (Springer-Verlag, New York 1996) pp 259–279
162. D.C. Cabra, M.D. Grynberg, P.C.W. Holdsworth, A. Honecker, P. Pujol, J. Richter, D. Schmalfuß, J. Schulenburg: Phys. Rev. B **71**, 144420 (2005)
163. R. Moessner, S.L. Sondhi: Phys. Rev. B **63**, 224401 (2001)
164. R. Moessner, S.L. Sondhi, P. Chandra: Phys. Rev. B **64**, 144416 (2001)
165. J. Richter, J. Schulenburg, A. Honecker, J. Schnack, H.-J. Schmidt: J. Phys.: Condens. Matter **16**, S779 (2004)
166. J. Schnack, H.-J. Schmidt, J. Richter, J. Schulenburg: Eur. Phys. J. B **24**, 475 (2001)
167. H.-J. Schmidt: J. Phys. A: Math. Gen. **35**, 6545 (2002)
168. M. Oshikawa: Phys. Rev. Lett. **84**, 1535 (2000)
169. J. Richter, O. Derzhko, J. Schulenburg: Phys. Rev. Lett. **93**, 107206 (2004)
170. T. Momoi, K. Totsuka: Phys. Rev. B **62**, 15067 (2000)
171. S. Gluzman: Phys. Rev. B **50**, 6264 (1994)
172. A. Honecker: Can. J. Phys. **79**, 1557 (2001)
173. G. Jackeli, M.E. Zhitomirsky: Phys. Rev. Lett. **93**, 017201 (2004)
174. K. Onizuka, H. Kageyama, Y. Narumi, K. Kindo, Y. Ueda, T. Goto: J. Phys. Soc. Jpn. **69**, 1016 (2000)
175. K. Kodama, M. Takigawa, M. Horvatić, C. Berthier, H. Kageyama, Y. Ueda, S. Miyahara, F. Becca, F. Mila: Science **298**, 395 (2002)
176. G.A. Jorge, R. Stern, M. Jaime, N. Harrison, J. Bonča, S. El Shawish, C.D. Batista, H. Dabkowska, B.D. Gaulin: Phys. Rev. B **71**, 092403 (2005)
177. S. Miyahara, K. Ueda: Phys. Rev. B **61**, 3417 (2000)
178. Y. Fukumoto, A. Oguchi: J. Phys. Soc. Jpn. **69**, 1286 (2000)
179. Y. Fukumoto: J. Phys. Soc. Jpn. **70**, 1397 (2001)
180. C. Knetter, A. Bühler, E. Müller-Hartmann, G.S. Uhrig: Phys. Rev. Lett. **85**, 3958 (2000)

181. H. Kageyama, M. Nishi, N. Aso, K. Onizuka, T. Yosihama, K. Nukui, K. Kodama, K. Kakurai, Y. Ueda: Phys. Rev. Lett. **84**, 5876 (2000)
182. C. Knetter, G.S. Uhrig: Phys. Rev. Lett. **92**, 027204 (2004)
183. S. Miyahara, F. Becca, F. Mila: Phys. Rev. B **68**, 024401 (2003)
184. M.E. Zhitomirsky, A. Honecker, O.A. Petrenko: Phys. Rev. Lett. **85**, 3269 (2000)
185. A. Honecker, O.A. Petrenko, M.E. Zhitomirsky: Physica B **312-313**, 609 (2002)
186. A. Fledderjohann, K.-H. Mütter: Eur. Phys. J. B **24**, 211 (2001)
187. M.-C. Chang, M.-F. Yang: Phys. Rev. B **66**, 184416 (2002)
188. S.E. Palmer, J.T. Chalker: Phys. Rev. B **64**, 094412 (2001)
189. G. Misguich, B. Bernu, C. Lhuillier, C. Waldtmann: Phys. Rev. Lett. **81**, 1098 (1998)
190. T. Momoi, H. Sakamoto, K. Kubo: Phys. Rev. B **59**, 9491 (1999)
191. K. Kubo, T. Momoi: Z. Phys. B **103**, 485 (1997)
192. V.N. Popov: Theor. Math. Phys. **11**, 565 (1972)
193. S. Gluzman: Z. Phys. B **90**, 313 (1993)
194. S. Sachdev, T. Senthil, R. Shankar: Phys. Rev. B **50**, 258 (1994)